ASSESING SOIL STRENGTH FROM GEOPHYSICAL SURVEYS

A Thesis

by

REHAN KHAN

Submitted to the Office of Graduate and Professional Studies of
Texas A&M University
in partial fulfilment of the requirements for the degree of

MASTER OF SCIENCE

Chair of Committee, Giovanna Biscontin
Co-Chair of Committee, Charles Aubeny
Committee Member, Luis San Andres
Head of Department, Robin Autenrieth

May 2014

Major Subject: Civil Engineering

ABSTRACT

A study is presented to develop framework for correlating sand strength (friction angle) to geophysical measurements, primarily shear wave and body wave velocities. Triaxial tests accompanied by wave velocity measurements was performed to generate a matrix relating bulk modulus and shear modulus to soil strength over a range of soil types, stress levels, stress history and soil density.

Two types of sands- Mystic White (angular) and Ottawa (rounded) were tested at four different confining pressures (5kPa, 15kPa, 30kPa and 60kPa) and for each sand type at a given stress level, two types of samples, dense and loose, were prepared, resulting in 16 tests overall. The sands were selected so as to match the requirements of maximum and minimum void ratios and angularity. Separate samples were prepared for each test and duplicate testing was conducted for at least one stress level of each material type.

The GEOTAC TruePath Automated Stress Path system was employed to carry out anisotropically consolidated tests. This system also includes pore pressure and cell pressure flow pumps allowing automatic feedback control of the cell pressure and back pressure through the software. Flow pumps were needed primarily to measure volume changes.

The caps in the triaxial apparatus were equipped with piezoelectric transducers, manufactured by GCTS Testing Systems and fit the GEOTAC setup. One set of caps had bender elements (protruding from the caps) and p-crystals installed while the other set had both p and s-crystals (mounted under the surface of the cap) installed. The system is completed by a Tectronix arbitrary function generator AFG320, a Tectronix oscilloscope TD3014B and TDS3GV and a Piezosystems PiezoLinear amplifier.

A qualitative correlation between sediment strength normalized with respect to confinement and stiffness is obtained and the conclusion drawn that further tests are required for a quantitative correlation.

ACKNOWLEDGEMENTS

I would like to thank my committee chair, Dr. Biscontin and co-chair Dr. Aubeny, for their guidance and support throughout the course of this research. Thanks also go to my colleague in the lab Madhuri Murali and the lab coordinator Mike Linger for the timely help that was much needed for the completion of the project.

Finally, thanks to my parents and friends for their constant encouragement and love.

TABLE OF CONTENTS

Page

LIST OF FIGURES

LIST OF TABLES

CHAPTER I

INTRODUCTION

These days offshore exploration is gaining importance primarily due to a gradual depletion of hydrocarbon reserves onshore or near the coastlines. This calls for offshore site investigation, which is very expensive. Offshore structures include oil platforms, artificial islands and submarine pipelines and the seabed has to be able to withstand the weight of these structures and the applied loads. Usually soil conditions offshore are more difficult to ascertain and the offshore structures typically have to bear significant lateral loads, cyclic loading and geohazards. The environmental and financial costs are higher in case of failure in offshore conditions. So the strength analysis of offshore soils is an exacting process and very crucial to the successful completion of any offshore project.

The goal of this study is to perform laboratory tests to develop a preliminary analytical framework such that uncertainties in estimating soil strength from the results of geophysical tests can be quantified and reduced. We seek to obtain geotechnical information for a range of materials anticipated to be encountered in the upper 5 m of the seafloor without requiring direct contact with the seafloor. The usefulness of the study undertaken relies on the ease and quickness with which geophysical surveys can be performed offshore. If there existed correlations between sediment strength and the geophysical data on sands then the high cost and time required to obtain strength through running experiments can be avoided. The study undertaken is based on this very idea and aims to correlate the sand friction angle to the shear modulus. The interpretation of classical geotechnical data can be limited to the vicinity of the borehole, but geophysical survey techniques provide a complete spatial approach to the estimation of soil properties. They cover a zone of much greater extent and give access to the average values of dynamic moduli on a large scale, though at a lower resolution (Emerson & Foray, 2006).

Traditionally for sands, strength is obtained through in-situ tests. These tests, however, have the drawbacks of accessibility and costs which calls for alternative methods to get the strength and this

study presents an alternative that is based on correlating the strength parameter to a more easily obtainable geophysical measurement. In offshore soils, especially in deep waters it is not feasible to conduct in situ tests that require direct contact with the seabed. A number of in situ test devices are available for offshore use. These include the piezocone, the pressuremeter, the dilatometer, nuclear density and electrical resistivity probes, seismic cone and the screw plate. But the results from these tests should be complemented by laboratory testing. Lunne et al. (1985) suggested that the selection of final design parameters should not be based on results of in situ tests alone and that a thorough laboratory investigation is of utmost importance. Even if in future in situ testing is used more extensively, this will not eliminate the need to take good samples and test them in the laboratory.

In the cone penetration test, the measured sleeve friction is not so accurate and liable to variability from one cone to another. Among other factors, the pore pressure induced during cone penetration affects the sleeve friction measurement (Campanella et al. 1982). Also the measured pore pressure depends on the location of porous filter. The correlations between the constrained modulus, M and the cone resistance do not take into account stress and strain history, stress level, relative density of sand and mineralogical composition which is related to crushability of sand grains. In the pressuremeter test, the self boring can provide reliable measurement of horizontal stress only if the self boring operation is carried out with utmost care or else the starting pressure of the expansion test is invariably equal to in situ pore pressure. Also due to disturbance caused by the insertion process, the push in pressuremeter can't be used to get in situ stresses in sand. The push in and self boring pressuremeter tests tend to give different effective friction and dilation angles. In the dilatometer test it is unclear whether the friction angle obtained is representative of drained or undrained conditions.

Chapter 2 -'Literature review' presents historical review of strength assessment in soils with a focus on offshore field methods. Work done by researchers previously on sands is highlighted. Then there is a review of geophysical methods used in the laboratory. Chapter 3 –'Triaxial testing' starts with a description of the geomaterial used for running the tests including gradation curves and relative

densities. The method used for preparing the specimen is discussed at length and its advantage over other methods in the literature is pointed out. A brief overview of testing methods and procedures follows next with the steps followed in data reduction. Results of triaxial tests are presented in the form of deviatoric stress- axial strain plots and volumetric strain- axial strain plots. It was initially proposed that a total of 16 tests would be run- eight on rounded sand and 8 on angular sand. Each type of sand was tested at four different confining pressures (5, 15, 30 and 60 kPa) and for each sand at a given confining pressure, two samples were prepared which were representative of dense and loose soils. However, 5 kpa tests on angular sand was not possible due to the fact that the sample failed to stand at such a low value of confining pressure. So a total of fourteen tests were run instead. Shear strength and friction angles at failure and at 'near critical state' formed the table of results and are included in the final data set. The dependence of shear strength and friction angle on confining pressure and on density is plotted and compared with Schmertmann's correlation. Some typical trends in the stress- strain plot and the volumetric behavior of sands are underlined. For example, dense sands undergo failure (characterized by peak in the stress- strain plot) at about 1-4 % strain. For loose sands there is no peak and the stress keeps on increasing until the sample reaches critical state. Chapter 4 –'Bender Element Testing' introduces the concept of how shear modulus of soils can be measured in the laboratory and the equipment used for this purpose. The ultrasonic test system and the test principles are discussed in detail. All the methods for determining the travel time of waves in soil are delineated and the method that was actually adopted for this project is elaborated upon in a detailed manner. Recommendations are made regarding the choice of frequency of the waveform to be used so as to obtain clear signals on the oscilloscope and also to avoid near field effects. Travel time measurements are taken at two instances during the course of the test- the first one right before the start of shearing, i.e., when the vertical stress is such that the ratio of vertical to horizontal stress is K_0:1, and the second measurement is taken at the end of shear, typically at 20% strain. Finally the results are tabulated and the table includes the shear wave velocity, body wave velocity, shear modulus and bulk modulus of the soil for each sand type at each confining pressure and for each relative density. Once again, the effect of

confinement and relative density of the sample on shear modulus is noted just like for the case of triaxial testing. Additionally, the after-shear modulus values are compared to the before-shear modulus values and the trend noted for both dense and loose sand. Theoretical explanation is given for any trend observed. Chapter 5 –'Conclusions' is a brief summary and restatement of the findings and also recommended future work. The ultimate goal is to come up with correlations between the two sets of data collected from the tests and correlate the friction angle with shear modulus and see how such correlations are affected by confining pressure, relative density of sample, stress and strain history of the soil, and sand type (angularity of grains).

CHAPTER II

LITERATURE REVIEW

The shear strength of soils is usually interpreted by Mohr-Coulomb theory, which combines Mohr circles with frictional resistance. When Mohr circles of different tests of the same sand at different confining pressures are drawn together, the slope of the tangent (known as failure envelope) to the circles is used to get the friction angle. The equation is known as Mohr-Coulomb failure criterion:

$$\sigma_1' = \sigma_3' \left(\frac{1+\sin\phi}{1-\sin\phi} \right) + 2c' \left(\frac{\cos\phi}{1-\sin\phi} \right)$$

For sands, c= 0, so the friction angles can be calculated as:

$$\phi_p = \sin^{-1} \left(\frac{\sigma_1' - \sigma_3'}{\sigma_1' + \sigma_3'} \right)_p$$

$$\phi_{cv} = \sin^{-1} \left(\frac{\sigma_1' - \sigma_3'}{\sigma_1' + \sigma_3'} \right)_{cv}$$

2.1. Particle size contribution to sand strength

There are three components contributing to the strength of sand: sliding friction due to microscopic interlocking arising from surface roughness; interlocking friction caused by physical resistance to relative particle translation and this is why energy is required to cause dilation of sand; and rolling friction which is the reason we need energy to rearrange and reorient materials. Figure 2.1 shows the relative contribution of all the three factors to the strength as a function of the void ratio. Dense sand when sheared results in grains getting entangled at an early stage which mobilize more friction and hence a higher shear strength.

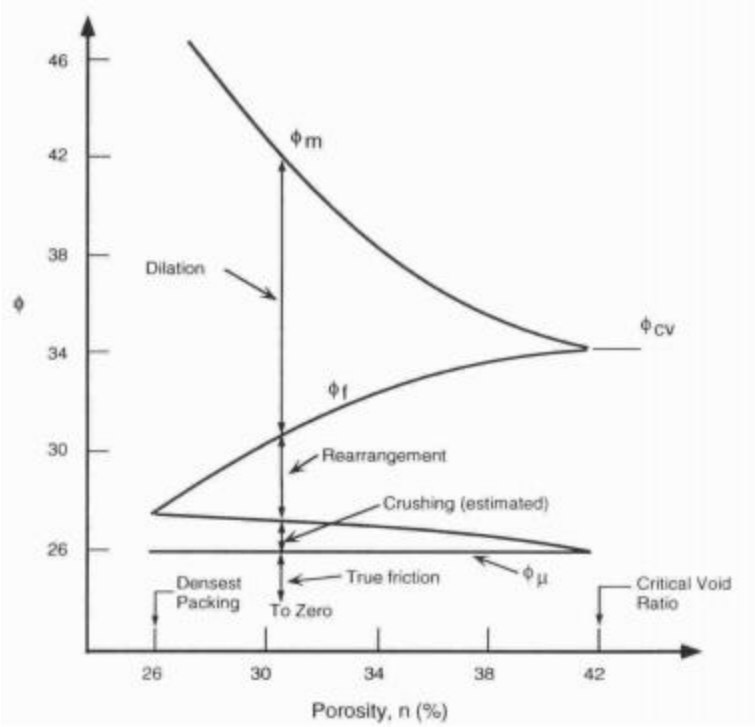

Figure 2.1: Relative contribution to shear strength of sands (Mitchell, 1993)

The friction angle can be correlated to the grain size distribution as can be seen from the work of Kara et al. (2013). It was concluded that the internal friction angle increased with the increase of the Uniformity Coefficient for sands consisting of feldspar and calcite. Kara et al. (2013) conducted direct shear tests on 17 samples of Tergha sand. Seven different particle size ranges were identified to constitute the sand. Seven samples were prepared, each sample consisting of particles from one particular size range. In addition, ten samples were prepared each sample containing different percentages from the seven different particle size ranges. The following correlations were arrived at

$$\Phi_i^{peak} = 34 + 10d_i$$

$$\Phi_i^{CS} = 29 + 3d_i$$

where:

d_i $[mm]$: $smallest\ diameter\ of\ particle\ size\ range$ $[di + 1, di]$

Φ_i^{peak}: peak friction angle

Φ_i^{CS}: critical state friction angle

The above equation gives the friction angle for each particle size range. If we wish to obtain the global friction angle of sands that contains more than one particle size range then the results show that the peak friction angle corresponds to the sum of contribution of the various size ranges, the contribution of each class being equal to its peak friction angle balanced by its percentage in the grain size distribution of the sample.

$$\Phi^{peak} = \sum_i \Phi_i^{peak} * p_i$$

2.2. Friction angle and dilatancy

Φ^{peak}, in addition to other factors, also depends on stress path. So plane strain tests and triaxial tests yield friction angles that defer by more than 5^0 for dense sands. However, Bolton and Rowe (1986) have presented data that suggest a unique angle for loose sands. Results obtained by Schanz & Vermeer (1995) from triaxial tests on dense and loose Hostun sand when compared to the results obtained by Hammad (1991) from plane strain tests on the same sand has also revealed that a significant difference existed for the dense sand peak friction angle, whereas there is very little difference for the loose sand friction angle. This finding is also confirmed by data on other sands. Hence it can be concluded that a unique critical state friction angle exists independent of strain conditions.

Dilatancy can be defined as the volume change associated with the application of shear stresses. The angle of dilation is the ratio of plastic volumetric strain rate to the plastic shear strain rate. Expansion or increase in volume is considered positive dilation while contraction is considered as negative dilation. The rate of dilation was studied by Schanz and Vermeer (1995). It is accepted that the triaxial rate of dilation coincides with the plane strain rate and thus there exists a unique definition for the angle of dilatancy.

The angle of dilatancy for plane strain situations is defined as:

$$\sin\psi^{ps} = -\frac{\dot{\varepsilon}_1 + \dot{\varepsilon}_3}{\dot{\varepsilon}_1 - \dot{\varepsilon}_3}$$

For triaxial tests, the angle of dilatancy is defined as:

$$\sin\psi = -\frac{\dot{\varepsilon}_v/\dot{\varepsilon}_1}{2 - \dot{\varepsilon}_v/\dot{\varepsilon}_1}$$

The above equation is valid for both test conditions because ϵ_2 vanishes for plane strain, giving $\epsilon_v = \epsilon_1 + \epsilon_3$. Bolton (1986) presented numerous data to show that both tests yielded the same peak ratio of ϵ_v/ϵ_1. Rowe's stress dilatancy theory attempts at predicting the dilatancy angle in triaxial testing as a function of critical state friction angle. Rowe proposed an expression that states that the ratio of work done by the major principal compression stress on the sample to the work done by the sample on the minor principal stresses in a triaxial test is constant. The constant K is related to the soil friction angle.

$$K = \frac{1 + \sin(\Phi)}{1 - \sin(\Phi)}$$

Rowe used a minimum potential energy ratio principle to develop this relation. DeJong (1976) arrived at the same relation by applying only the friction laws to the same 'toothed separation plane' model as was treated by Rowe, without resorting to energy principles. Friction rules state that when friction exists in the contact surface between two rigid bodies, their relative displacement depends on the deviation angle, λ, between the normal to contact surface and the direction of force transmitted through that surface. λ can never be greater than Φ_u and bodies can slide only if $\lambda = \Phi_u$. Three terms- stress ratio, $R = \sigma_1'/\sigma_3'$; strain increment ratio, $D = (\epsilon_2' + \epsilon_3')/ -\epsilon_1'$; and $E^* = R/D = \sigma_1' \epsilon_1'/(\sigma_2' \epsilon_2' + \sigma_3' \epsilon_3')$ are introduced. After rigorous mathematical deductions it can be shown that $E* = tan^2(\frac{\Pi}{4} + \frac{\Phi}{2}) = K$. Physical interpretation of E* suggests that the numerator of E* is the work done by the major principal stress, σ_1 on the sample and the denominator is the work done by the sample on the minor principal stresses σ_2 and σ_3. As can be seen the ratio of these two works is a constant. On combining the equation $E^* = K$ with the definition for dilatancy angle, ψ it is found that

$$\sin \phi'_m = \frac{\sin \phi'_{cv} + \sin \psi}{1 + \sin \phi'_{cv} \sin \psi}$$

where φ'_m is the Mohr Coulomb friction angle.

The above equation relates the critical state friction angle with the Mohr Coulomb friction angle and dilatancy angle. However, for triaxial conditions of stress and strain this theory is supplemented by Bolton (1986) to obtain a relationship between the peak friction angle and dilatancy angle. Bolton correlated the peak friction angle with the critical state friction angle for both triaxial and plane strain tests.

$$\phi_p^{ps} - \phi_{cv}^{ps} \approx 5I_R$$

$$\phi_p^{tr} - \phi_{cv}^{tr} \approx 3I_R$$

I_R is the relative dilatancy index which depends on the relative density of the sample and the mean effective stress at the peak shear strength. Also a direct consequence of Bolton's findings is the following equation:

$$\phi_p^{tr} \approx \tfrac{1}{5}(3\phi_p^{ps} + 2\phi_{cv})$$

We can thus see that the differences between friction angles disappear as looser states are considered. Bolton also found that the rate of dilation was strain independent.

$$-\dot{\varepsilon}_v/\dot{\varepsilon}_1 = 0{\cdot}3I_R$$

This supports the notion of a unique dilatancy angle because this angle was related to the rate of dilation. Combining the above equation with the definition for dilatancy angle we get:

$$\sin \psi = \frac{0{\cdot}3I_R}{2 + 0{\cdot}3I_R} = \frac{I_R}{6{\cdot}7 + I_R}$$

The peak friction angle reduces with increasing stress level resulting in a curved peak strength envelope in the Mohr-Coulomb plot. The peak friction angle, ϕ_p approaches the critical state friction angle, ϕ_{cs} at

very high stress levels. It is noteworthy that ϕ_p and ϕ_{cs}, dilation, and reduction of ϕ_p with stress level are all linked.

The 'Sawtooth model' establishes the relationship between angles of friction and dilation. If one block slides over another on a flat plane with coefficient of friction $\mu = \tan(\phi_{cs})$, then the ratio of normal to shear stress is $\frac{\tau}{\sigma} = \tan(\phi_{cs})$. If we consider sliding on a plane with teeth at an angle ψ to the horizontal with the same friction then it can be shown that $\frac{\tau}{\sigma} = \tan(\phi_{cs} + \psi)$ so that $\phi = \phi_{cs} + \psi$. There are many more theories in literature to explain the relationship between friction and dilation angles. Taylor (1948) hypothesized that the energy dissipation rate due to friction is proportional to the normal stress and the shear strain rate, $\tan(\phi_{cs})$ being the constant of proportionality. $W = \tan(\phi_{cs}) * \sigma * \gamma$. The energy dissipation rate must be equal to the input work which includes the work done by shear stress as well as normal stress. Therefore, $\dot{W} = \sigma'_n \dot{\varepsilon}_v + \tau\dot{\gamma} = (\tan\phi'_{cv})\sigma'_n\dot{\gamma}$

Noting that $\tan(\phi_{cs}) = \frac{\tau}{\sigma}$ and that $\tan(\psi) = \frac{\varepsilon}{\gamma}$ we get $\tan(\phi) = \tan(\phi_{cs}) + \tan(\psi)$

It should be noted that the above flow rules can be applied in two distinct senses. They may either be used to obtain the relationship between the mobilized friction angle and the current dilation rate as a test progresses. Or they may be used to express the relationship between the peak friction angle and the maximum dilation rate for several tests on the same material. Bolton (1986) took an empirical approach and came up with the following fit:

$$\phi'_p = \phi'_{cv} + 0.8\psi_{max}$$

Having firmly established the relationship between friction and dilation, it is time to turn to the relationship between dilation and density. Intuition dictates that denser the sample the more it will tend to expand. Stroud (1974) carried out a well controlled set of simple shear tests with each test starting at about the same density and all showed about the same angle of dilation. Wroth (1958) had carried out simple shear tests on steel balls initially packed at different densities and the rate of dilation was higher

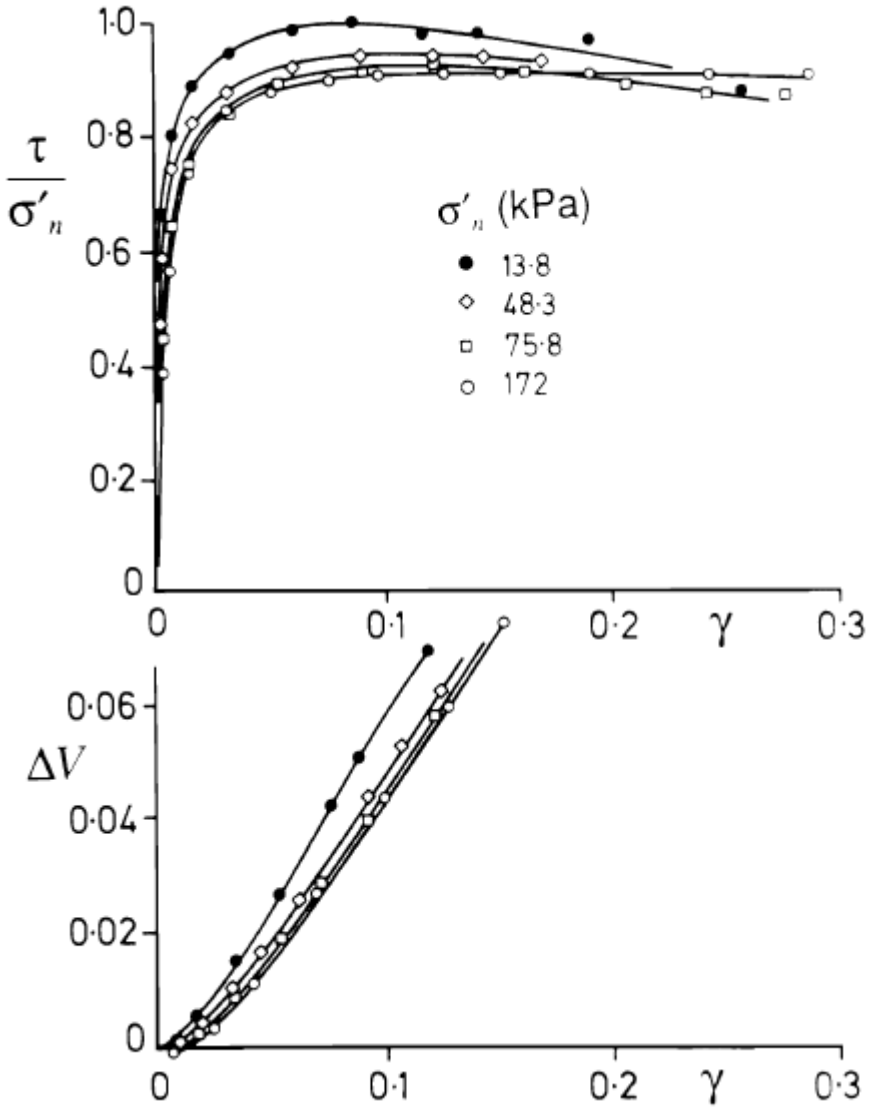

Figure 2.2: Shear stress- shear strain and volumetric strain- shear strain for simple shear tests on sand (Stroud, 1971)

for samples which were initially at a lower void ratio. The samples dilated until they reached the same critical void ratio, irrespective of their initial density, at which point they continued to shear with no further change in void ratio. These experiments formed the basis of Critical State Soil Mechanics. The critical void ratio, however, is not unique and reduces slightly with increasing normal stress. Figure 2.3 leads to the concept of critical state line (CSL) as the end points (critical state) of all of Stroud's tests on sand are plotted in the form of specific volume against mean stress and the points fall on a straight

line with the critical void ratio reducing with pressure. It is observed empirically for clays that the CSL is parallel to the normal compression line in the consolidation plot.

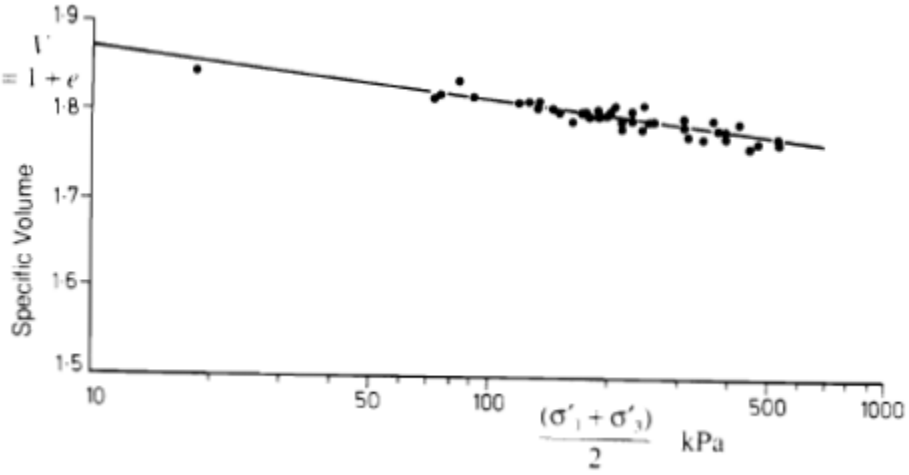

Figure 2.3: Critical state line for simple shear tests on sand (Stroud, 1971)

Stroud's tests' results as presented in Figure 2.5 show that the primary controlling factor for the peak strength is density, with denser samples giving a higher strength, but at a given density the friction angle reduces with stress level. This reduction is linked to the slope of the CSL.

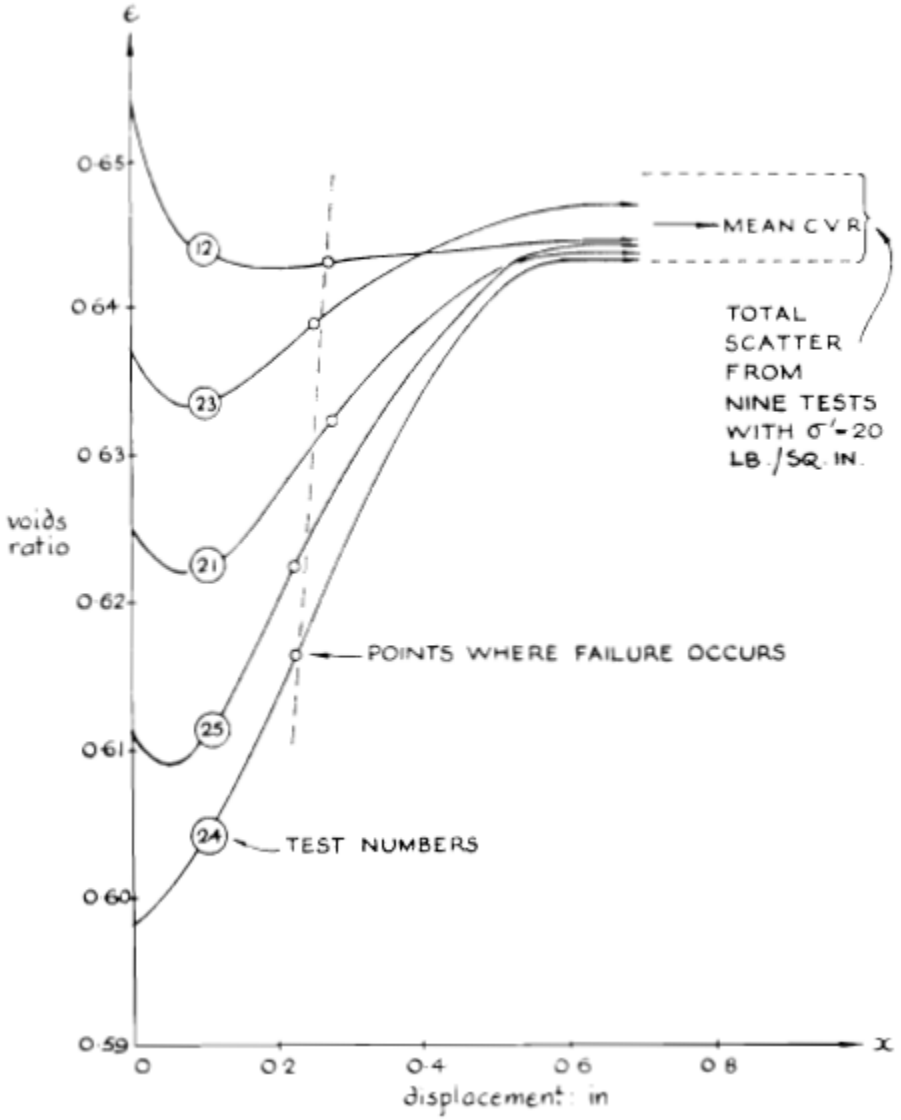

Figure 2.4: Void ratio against shear displacement for simple shear tests on steel balls (Wroth, 1958)

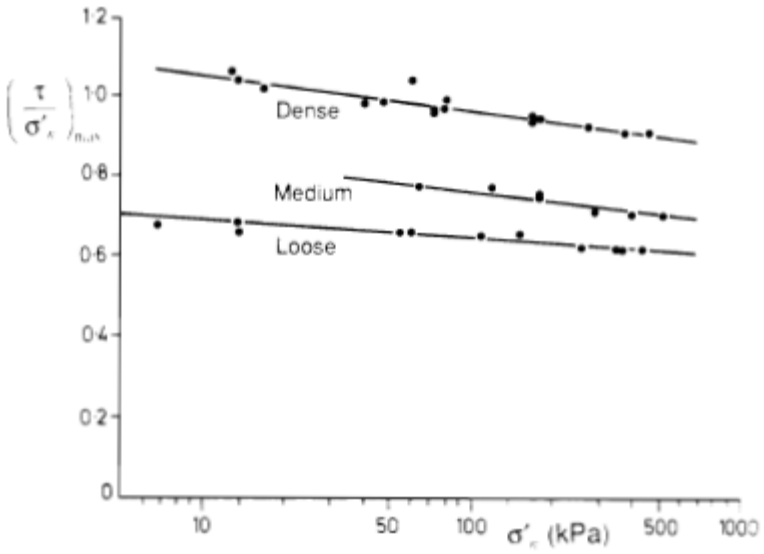

Figure 2.5: Peak strength against stress level for simple shear tests at different densities (Stroud, 1971)

On the CSL, the rate of dilation is zero, and it seems reasonable that the rate of dilation should be a function of the distance of the current stress point from the CSL. If we introduce a term V_λ such that it has an inverse relationship with the distance between the initial point on the e-ln p' plot and the point vertically above on the CSL then higher the value of V_λ the closer the point to the CSL and lower will be the dilation and vice versa. In figure 6, the peak friction angles from Stroud's tests are plotted against V_λ, and all the tests from all combinations of pressure and density, plot on a single curve. The peak strength is therefore a unique function of the distance from the CSL. In view of the relationships between friction and dilation angles already established, this also means that the maximum dilation rate is a unique function of V_λ.

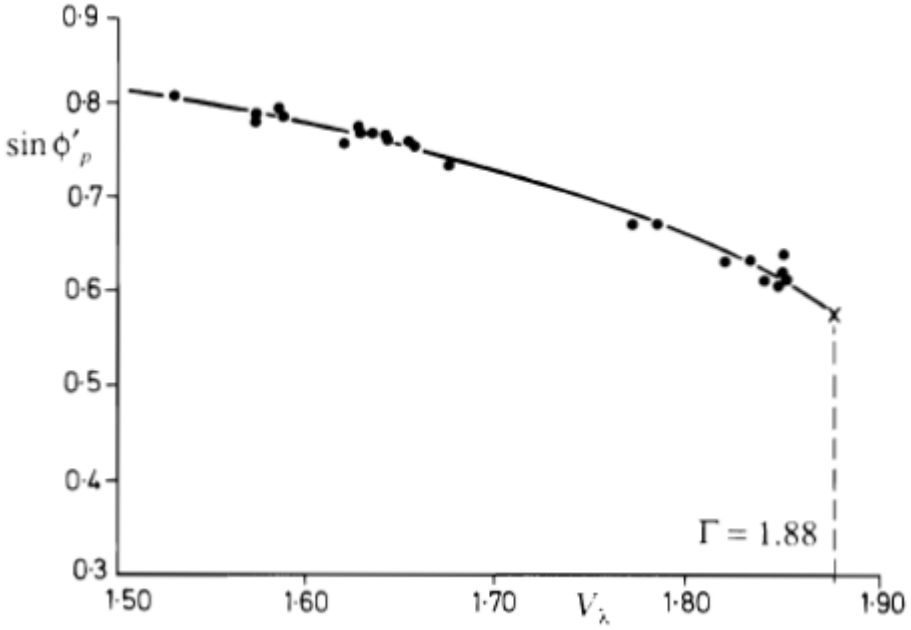

Figure 2.6: Peak strength plotted against V_λ (Stroud, 1971)

The following expressions give the relationship between sand dilation and relative density and confining pressure, derived from Wroth's expression:

$$\sin\psi = \alpha(\Gamma - V_{max}) + \alpha(V_{max} - V_{min})I_D - \alpha\lambda\ln\left(\frac{p'}{p_a}\right)$$

$$\psi = -0.11 + 0.59I_D - 0.11I_D\ln\left(\frac{p'}{p_a}\right)$$

2.3: Offshore field methods for sand strength

The in situ devices available for offshore use include piezocone, pressuremeter, dilatometer, nuclear density and electrical resistivity probes, seismic cone and screw plate. The use of in situ tests is important in sands where it is not possible to obtain representative undisturbed samples.

Cone penetration test (CPT) measures cone tip resistance and sleeve friction. The piezocones also measure pore-water pressure. Special density probes measure the in situ porosity.

Electrical resistivity probes also measure the electrical resistivity of the soil volume in addition to cone resistance and sleeve friction. A separate probe measures the resistivity of pore water. Readings are taken at 0.2 m intervals and correlated to laboratory calibrations on specimens reconstituted to different porosities.

Nuclear density probe has a radioactive source and detector built into a cone. The bulk density of soil is determined by comparing the energy level of emitted photons from the source and the photons entering the detector after backscattering from the soil mass. It was recently used offshore (Tjelta et al., 1985).

Seismic cone is a piezocone combined with a set of seismometers built into the cone. The cone resistance, sleeve friction and pore pressure is measured and is used to determine the soil layering at a site. The downhole shear wave velocity is measured at intervals and a profile of initial modulus is thus obtained.

Dilatometer test (DMT) measures soil contact pressure and the 1 mm expansion pressure. In situ horizontal stress, stress history, constrained modulus and effective friction angle can be predicted using empirical correlations. Dilatometer results were used by Robertson and Campanella (1984) to predict liquefaction potential of sands. The device has also been used offshore in limited water depths (Burgess et al., 1983).

Pressuremeter test provides in situ stress- strain curves from which the friction angle, dilation angle and drained shear modulus are derived. The push-in pressuremeter was developed mainly for offshore use. The self boring pressuremeter is also used offshore. This device tunnels itself into the ground and induces the least disturbance of all in situ devices.

Screw plate is a flat pitch auger screwed into the ground and loaded vertically. The settlement versus time is measured at selected depth intervals, but penetration is limited to 15-20 m in a medium dense sand. It has only been used onshore up to now.

2.4: Bender element testing

Bender elements were first introduced into soil applications in the late 1970's. The goal was to provide a simple, accurate and cost eefective alternative to other more complicated laboratory small strain shear modulus tests. Bender elements are piezoceramic plates that oscillate when electrically charged by a variable voltage or produce a voltage when stimulated by a vibration. When placed in contact with soil specimen this oscillation can be utilized to send a shear wave through the soil. As a result of the aforementioned oscillation the neighboring soil particles shift past one another resulting in a shear wave transmission. By placing one element each at the top and bottom of the soil sample, a wave can be sent and received. The time lag between the sent and received waves can be used to determine G_{max} which is useful when dealing with engineering projects that are adversely affected by vibrations and ground movement (Landon 2004). Prior to bender elements, the most common laboratory method for determining G_{max} was the resonant column test, performed using relatively complex equipment operated by experienced technicians which was expensive, time consuming, and subject to operator error.

In a typical bender element set-up, there is a function generator, power source, an oscilloscope and a computer as shown in Figure 2.7.

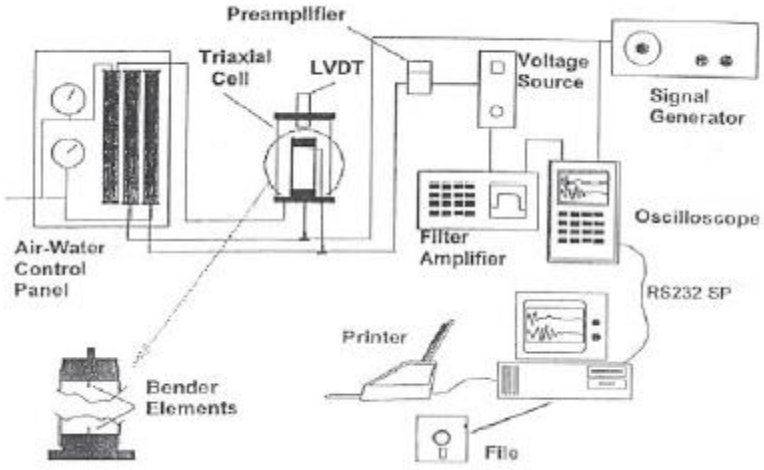

Figure 2.7: Schematic of bender element set-up (Brocanelli and Rinaldi 1998)

In order to excite the bender element, wires are soldered to the tile. The excitation is possible due to the polarization of the piezoceramic material, which refers to the alignment of positive and negative charges in the crystal. Depending on the alignment, bender elements may be either parallel (plates are poled in the same direction meaning both faces of the bender element have the same charge) or series (if the two plates are poled in opposite directions).

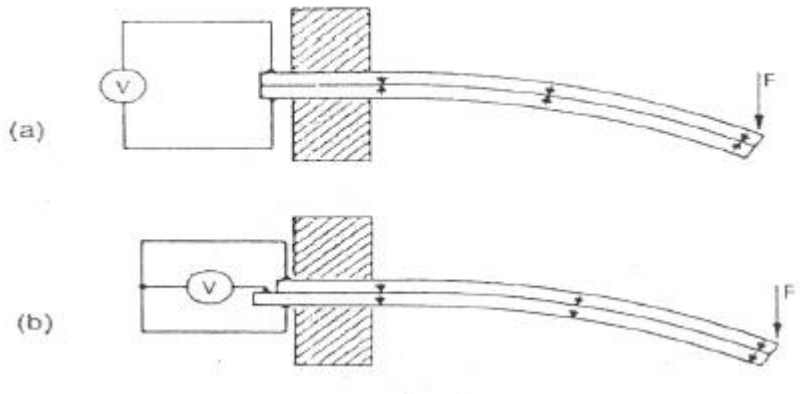

Figure 2.8: Bender elements poled in (a) series; (b) parallel (Wanders 1991)

In a typical set-up, the function generator excites the bender element by transmitting a sinusoidal input pulse which is more preferred than a square wave due to the fact that sine waves are composed of a single frequency and therefore are easier to interpret (Landon 2004). As the generated wave moves through the soil specimen it can be refracted and reflected, resulting in multiple waves being detected by the receiving bender element. Both the function generator and the receiving bender element must be connected to the oscilloscope in order to record the input pulse and the received pulse and be able to detect the time lag. There are many methods to determine travel time and they are discussed in detail in Chapter 4. Ideally the travel time should be independent of frequency. If desired, a frequency filter may be incorporated into the system to get rid of noise.

Function Generators excite the transmitting bender element. They can generate multiple wave forms-sine, square, triangle, and ramp, at a frequency range of 0.1 mHz to 21 mHz. Recent advances in function generator technology have allowed their adaptation to PC control with specific signals being sent to the function generator via software commands.

Oscilloscope records and displays the transmitted and received signals and is connected to both the function generator and the receiving bender element, at some sampling rate. Additionally, similar advances in oscilloscope technology have resulted in PC-controlled devices to replicate the functions of traditional oscilloscopes.

In order to amplify the received signal and reduce the mechanical load on the receiving bender element, a charge amplifier may also be introduced into the set-up.

As noted by Landon (2004), the system must be calibrated for any delay that occurs in the system due to the circuit and processing speed of the system. Calibration involves aligning the bender element tiles such that they are in tip to tip contact, and transmitting a signal through one of the tiles. The time difference between the initiation of the transmitted wave and the first arrival of the received wave is determined (Schmalz, 2007).

2.5: Small-strain shear modulus

Hardin and Richart (1963) and Roesler (1979) proposed one each general form of empirical equation to estimate the shear modulus of sands. Hardin and Richart (1963) performed a series of resonant column tests to obtain the following small strain shear modulus expression for round and angular Ottawa sands:

$$G_0 = C_g P_A^{1-n_g} \frac{(e_g - e)^2}{1 + e} \sigma_m'^{n_g}$$

Where C_g, e_g, and n_g are regression constants that depend solely on the soil.

Roesler (1979) developed the following correlation from shear wave velocity measurements:

$$G_0 = C P_A^{(1-n-m)} \sigma_a'^{n} \sigma_p'^{m}$$

where σ_a = normal effective stress acting along the direction of wave propagation; σ_p= normal effective stress perpendicular to the wave-propagation direction; and m,n, and C are fitting parameters.

Jamiolkowski et al. (1991) proposed a different form of the Hardin equation, accounting for the void ratio through a different function:

$$G_0 = C_g P_A^{1-n_g} e^{a_g} \sigma_m'^{n_g}$$

where a_g is a regression constant.

Iwasaki and Tatsuoka (1977) proposed the following correlation after studying G_0 for clean sands, natural sands with fines, and artificially graded sands with fines:

$$G_0 = C(\gamma) B \frac{(2.17 - e)^2}{1 + e} P_A^{1-m(\gamma)} (\sigma_m')^{m(\gamma)}$$

where $C(\gamma)$ and $m(\gamma)$ are fitting parameters that depend on strain level of the test; and B is a fitting parameter that is independent of strain, void ratio and confining stress. The above equation indicates that G_0 decreases with increasing fines content which is corroborated by D.C.F.Lo Presti (Salgado et.

al 2000) when he conducted resonant column tests on Ticino sandand showed that the coefficient C_g in Hardin's equation is reduced by 50% when the fines content increases from 0 to 25%. According to Randalf et al. (1994), the small strain stiffness of silty sand with 5-10, 10-15, and 15-20% silt content ranges might be reduced to about 50, 25, and 19% of the G_0 value of clean sand, respectively. The stiffness reduction with fines content is due to the way in which fnes interact with the sand matrix. If the fines are positioned with in the sand matrix in a way that they do not have well developed contacts with the sand particles, shear waves are not effectively transferred through the fine particles. Thus increse in relative density due to addition of fines do not lead to increase in G_0; accordingly, a silty sand at the same void ratio as a clean sand has a lower G_0. Secondly, the silt particles may more easily move sideways under shear stress application or shear wave propagation, leading to lower shear stiffness.

CHAPTER III

TRIAXIAL TESTING

3.1. Materials tested

Anisotropically consolidated triaxial tests were conducted on the following two sands: Ottawa sand which would be classified as *rounded*, and Mystic white sand which would be classified as *angular*. Both the Ottawa and the Mystic white sands predominantly had grains of a single size, which matched the opening size of sieve #30. So as per USCS classification, they are poorly graded sands. The sands are white in color with quartz being the chief mineral. The round sand was obtained from Ottawa, Illinois, while the angular sand was obtained from Berkeley Springs, West Virginia.

Figures 1 and 2 show the gradation curves for the two types of sands. The angular sand was sieved to ensure that it had a similar gradation as that of the rounded sand for the purpose of comparison of the test results.

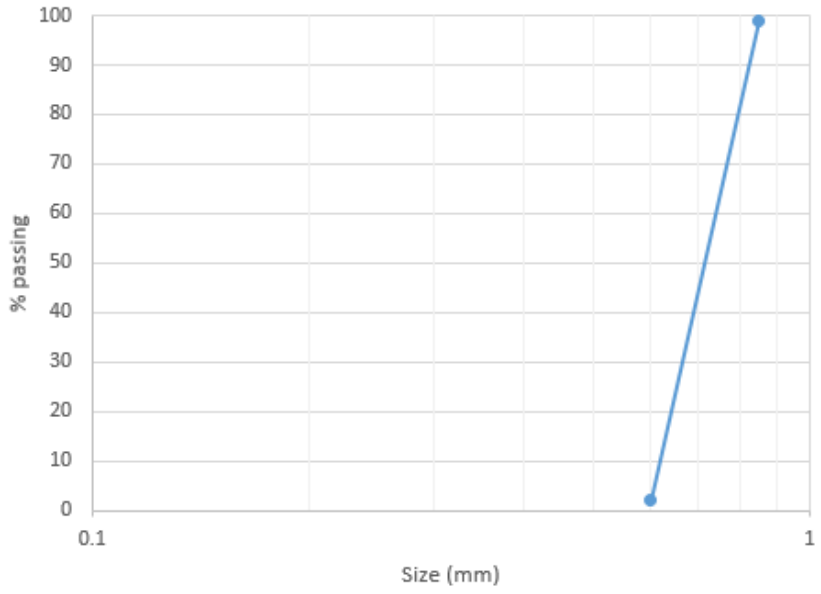

Figure 3.1: Ottawa sand gradation

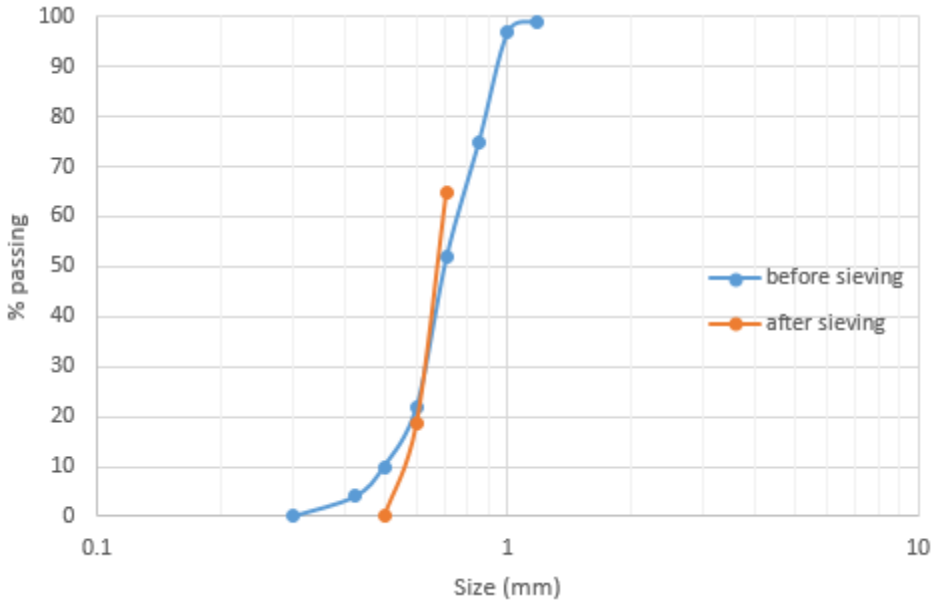

Figure 3.2: Mystic White sand gradation

Relative density tests were carried out on both the sands to get the maximum and minimum possible void ratios on a sample prepared from either of these sands. These tests were carried out as per the specifications given in ASTM D 4253 and ASTM D 4254 for the maximum index density and the minimum index density respectively.

For the determination of maximum density or minimum void ratio, we are trying to make our sample as dense as possible. The method of compaction using a 6" diameter mould was employed. The sand was filled in the mould in a layer-wise fashion (a total of 5 layers filled sand up to the brim of the mould). After each layer of sand was poured from a certain drop height, a suitable weight (1984 g) was placed on top of the sand surface and the mould was hammered 10 times followed by rotating the mould by 90 degrees and hammering again. This was repeated four times before the next layer of sand was poured and the process repeated.

For the determination of minimum density or maximum possible void ratio our goal is to make as loose a sample as possible. A glass graduated glass beaker was taken and the sand was gently placed at the

open end while keeping the beaker horizontal. Then the beaker was turned away from the horizontal position as slowly as possible so that the sand started falling towards the closed end of the beaker very slowly (ideally one grain at a time!). After all the sand had fallen to the other end the beaker was turned vertical very slowly.

At the end of both these processes mentioned above, the weight of the sand collected (in the 6" mould and the glass beaker) was measured and also the volume of sand collected (which is fixed for the mould and depends on height of the sample collected for the case of beaker). Knowing the volume, V and weight of the sample collected, W, the void ratios, e can be calculated using the relation

$$e = \frac{V}{\frac{W}{2.65 * Y}} - 1$$

Table 3.1: Relative density test results

Soil Type	Min void ratio	Max void ratio
Rounded sand	0.49	0.79
Rounded sand (Salgado et al., 2000)	0.48	0.78
Angular sand	0.80	1.10

The above table lists the maximum and minimum void ratios obtained for the two sands. Salgado et al. (2000) in his paper titled 'Shear strength and stiffness of silty sands' reported void ratio limits for rounded sand which are very close to the values we obtained.

3.2. Specimen preparation

The objective of sample preparation in the laboratory is to reproduce and simulate the in-situ soil conditions with regards to spatial homogeneity of the density, and organization of sand grain. Reconstituted specimens formed from disturbed materials are used in the laboratory because of the high costs involved in obtaining high quality frozen and undisturbed samples in sandy soil deposits. The various methods available in literature for sample preparation would be manual, vibration of the box, layer rodding, layer tamping etc. all of which have the drawbacks of producing samples that have poor reproducibility and/or poor homogeneity. Rad and Tumay (1987) concluded that among all the currently available techniques, pluviation (or raining) is the method that not only provides reasonably homogeneous specimens with the desired relative density but simulates a soil fabric most similar to the one found in natural deposits formed by sedimentation.

Specimen preparation method strongly influences the sand behavior. Miura & Toki (1982) showed that both stress- strain and volumetric strain- axial strain plots were affected by the specimen preparation method. Vaid et al. (1999) showed that the fabric induced by moist tamping and air pluviation caused specimens to contract while water pluviated samples dilated. Also, pluviation followed by compaction to the target density present the same stress- strain behavior as undisturbed frozen specimens. Moreover, pluviation has the added advantage that it is less operator dependent and the void ratio throughout the specimen height is more uniform.

3.2.1. Mechanism of pluviation

We had to make sure that the dense sample is as dense and the loose sample is as loose as possible to maintain consistency amongst all the samples prepared. Also we did not have porous stones in between the sample and the triaxial caps; instead the porous stones were embedded in the top and bottom caps. Thirdly, air was used to apply confining pressure instead of water because we were dealing with electronic ultrasonic caps that had wires coming out of them. The entire sample preparation procedure can be described in the following paragraphs.

First, the height of the split mould is measured from the bottom to the top cut mark and the height of the inner cylindrical portion of the bottom cap is subtracted from it to obtain the sample height. The diameter of the mould is measured next and the height and diameter are used to calculate volume of the sample. The bottom cap is screwed on to the pedestal and a membrane is placed around it. An O-ring holds the membrane to the pedestal. The split mould with another set of O-rings around it at the top is placed around the membrane so as to circumscribe it and the remaining portion of the membrane is folded at the top of mould over the O-ring. Vacuum is used to ensure that the membrane is taut everywhere inside the mould. The water soluble gel is spread over the bottom cap to facilitate reading of the wave signals. The arrangement is now ready for air pluviation of the sand using a funnel- guide tube arrangement.

A dense specimen is obtained by pouring the sand into the mould from a drop height of at least 10 cm. For a loose sample, a wire mesh is inserted at the bottom of mould and then the sand is poured through zero drop height meaning the guide tube at the end of the funnel always touches the surface of sand in the mould. After pluviating, the wire mesh is slowly lifted up through the sand to further fluff up the sample.

Now the top cap is placed over the sample, the membrane unfolded to cover the top cap and the O-ring slid above to make it surround the top cap. Vacuum is applied to the sample and the split mould is removed. The sample is ready to be tested.

3.2.2. Factors affecting sample density

The density of pluviated samples depended on fall height, depositional intensity and uniformity of the sand rain. As per Vaid and Negussey (1984), pluviation of sand can be idealized as a free fall of spheres of equivalent diameter D_{50} or further simplified and analyzed by considering the free fall of a single sphere if we neglect the interferences between the grains. So the sample density then depends only on the energy of particles impacting on the raising specimen surface. According to Stoke's law, a particle falling freely under gravity through a fluid (air, in our case) reaches a constant terminal velocity, the value of which is linearly dependent on sphere's diameter. This indicates that at equal fall heights, finer sands will have a lower density. For samples of high density, the effect of fall height on density is insignificant.

The maximum sample density corresponds to an optimum sand flow rate. As per Lagioia et al. (2005), the pluviating sand revealed that an energetic layer, three to four grains thick develops within which the compaction takes place. So at the optimum flow rate, the energetic layer is allowed enough time to move to the minimum potential energy position and the hammering effect of falling grains is most effective. At lower than optimum flow rates, the hammering effect is not as effective and at higher rates, the 'energetic' layer doesn't have enough time to move to the lowest energy position.

Uniformity of sand rain controls the uniformity of fabric and density. To that end a guide tube below the hopper was used to avoid disturbance of the rain. Care was taken to ensure that the material of the guide tube was such that no electrostatic charges developed during pluviation.

3.3. Introduction to triaxial test

A triaxial test is a common method to measure the mechanical properties of soils, rocks and other granular materials. Although the name might suggest that the stresses are different in all three directions, this is not true for our tests as with most triaxial tests. The horizontal stress is the same in both directions and it is different from the vertical stress. So it's not a "true" triaxial test.

The sand sample is contained in a cylindrical latex membrane with the top and bottom caps of the triaxial apparatus closing off the top and bottom end of the sample respectively. This arrangement is then enclosed in a hollow Perspex cylinder so that fluid (air) pressure can be applied to the sample. The top platen of the apparatus can be driven down along the axis of the cylinder to load the sample. The force required to move the piston is measured as a function of the distance that the upper platen travels, while the confining pressure is maintained constant. The net change in volume of sample can be determined by measuring how much water has moved in or out of the sample.

The principle behind a triaxial shear test is that the stress applied in the vertical direction (along the axis of the cylindrical sample) can be different from the stresses applied in the horizontal directions perpendicular to the sides of the cylinder, i.e. the confining pressure. In a homogeneous and isotropic material this produces a non-hydrostatic stress state, with shear stress that may lead to failure of the sample in shear. Every soil has an upper limit to how much shear stress it can withstand without failing and one of the objective of this test is to determine that limit, as a function of various other parameters. Failure is taken to have occurred at 15% strain, although we strained the samples to over 20% so that sample gets closer to critical state in order to compare the result of dense and loose samples at any given confinement. During shearing, the sample gets shorter and bulges outwards.

For our tests, we did not have porous stones in between the sample and the triaxial caps; instead the porous stones were embedded in the top and bottom caps. Moreover, air was used to apply confining pressure instead of water because we were dealing with electronic ultrasonic caps that had wires coming

out of them. Couplant has to be applied on the flat surface of the triaxial caps in order to receive a clear signal and to identify the arrival time of the waves.

We are mainly interested in obtaining the friction angle through the triaxial test.

3.4. Testing procedure

Figure 3.3 shows the load frame and placement of load and displacement transducer in the GEOTAC triaxial system while Figure 3.4 shows the entire TruePath automated triaxial system which also includes the flow pumps in addition to the triaxial apparatus.

Once the sample is prepared, it is important to ensure that it is fully saturated. This requires removal of all the air present in the void spaces. This is achieved by passing de-aired water through the sample from the bottom and letting it drain through the top cap. The water pushes most of the air out of the sample and dissolves the rest in the back saturation phase at a high back pressure. We switch between the two top valves and also the bottom valves for letting water into the sample and make sure that each valve is clear of air. After this the following steps are followed.

Back Saturation: To ensure that the sample is fully saturated, all the valves except for the one through which water enters the sample are closed. The cell pressure and pore pressure are increased to very large values around 20 psi (138 kPa) and 19 psi (131 kpa) respectively and the sample is left to saturate for a couple of hours. This will ensure that the smallest of air bubbles which were not eliminated from the sample gets dissolved.

Consolidation: During the back saturation phase the difference between cell and pore pressure was kept minimum, approximately 1 psi (~7 kPa). This difference is now increased so that the effective pore pressure equals K_0= 0.4 times the confining stress that we are testing the sample at. For example, for the 60kPa (8.7 psi) test, the difference between cell pressure and pore pressure is maintained at 0.4*8.7 = 3.48 psi. Sand consolidates immediately but we let the sample stay at this effective stress for an hour.

B-value check: B-value is the ratio of change in pore water pressure to increase in cell pressure when cell pressure is increased keeping the valves closed and thus arresting any water flow in or out of the sample. If our sample is fully saturated, whatever incremental cell pressure we apply will be taken up by the water in the pores and the pore pressure will also increase by an equal amount. If, however, the sample is not fully not saturated then a part of the incremental cell pressure will be taken up by the air in the voids. Consequently, the pore pressure won't increase as much. Thus, B-value is a measure of the degree of saturation of the sample. The closer the B-value to 1, the more saturated our sample is. For clays, a B-value very close to 1 can be attained but for sands the B-value after saturating the sample is usually in the range 0.65- 0.7.

Shear: The shearing process involves pushing the piston through the top cap down at a constant rate (5% per hour). The resistance that the sample applies to the piston is variable and this resistance (principal stress difference) is plotted as a function of the strain.

3.5. Difficulties in back pressure saturation

Lowe & Johnson (1960) gave the following expression for the back pressure required to bring a sample from an initial degree of saturation, S_i, to a final degree of saturation, S

$$P = Pi\frac{(S - Si)(1 - H)}{1 - S(1 - H)}$$

H is the Henry's constant, P_i is the pressure corresponding to S_i, and P is the additional pressure required to attain the desired saturation. Substituting S= 100% in the above equation gives$P100 = 49\ Pi\ (1 - Si)$.

in which P_{100} is the back pressure required for 100% saturation.

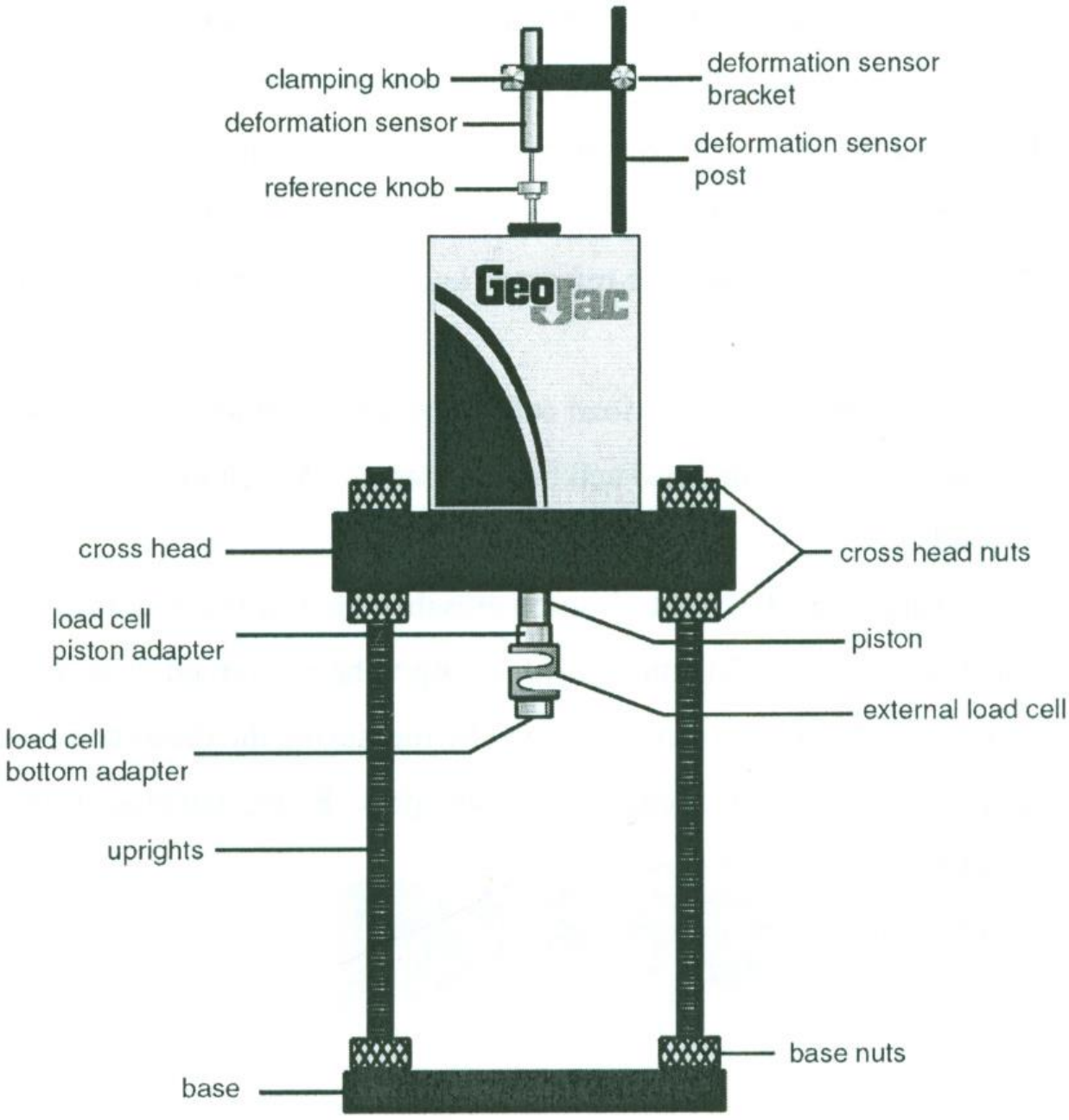

Figure 3.3: Load frame and load and displacement transducer in GEOTAC triaxial system (Biscontin and Aubeny, 2012)

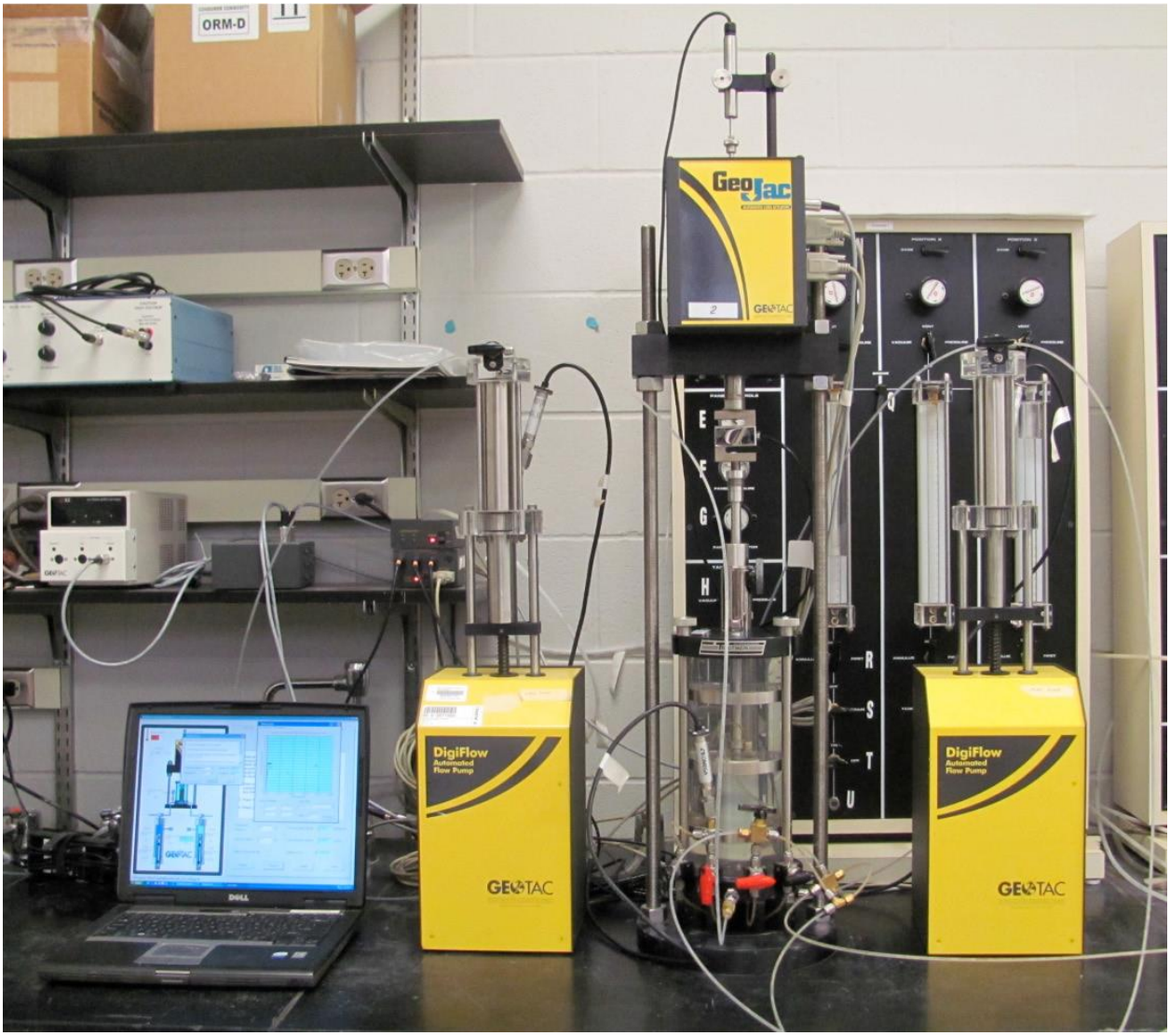

Figure 3.4: GEOTAC TruePath automated triaxial system

For complete saturation, the back pressure is increased to P_{100} or greater and then waiting until B-value test indicates that the sample has fully saturated. But Figure 3.5 below shows that for sands, even at saturations over 99%, the b-value could be anything in between 0.6 to 1. Moreover, for stiff sands, it is theoretically not possible to obtain B-value of 1.

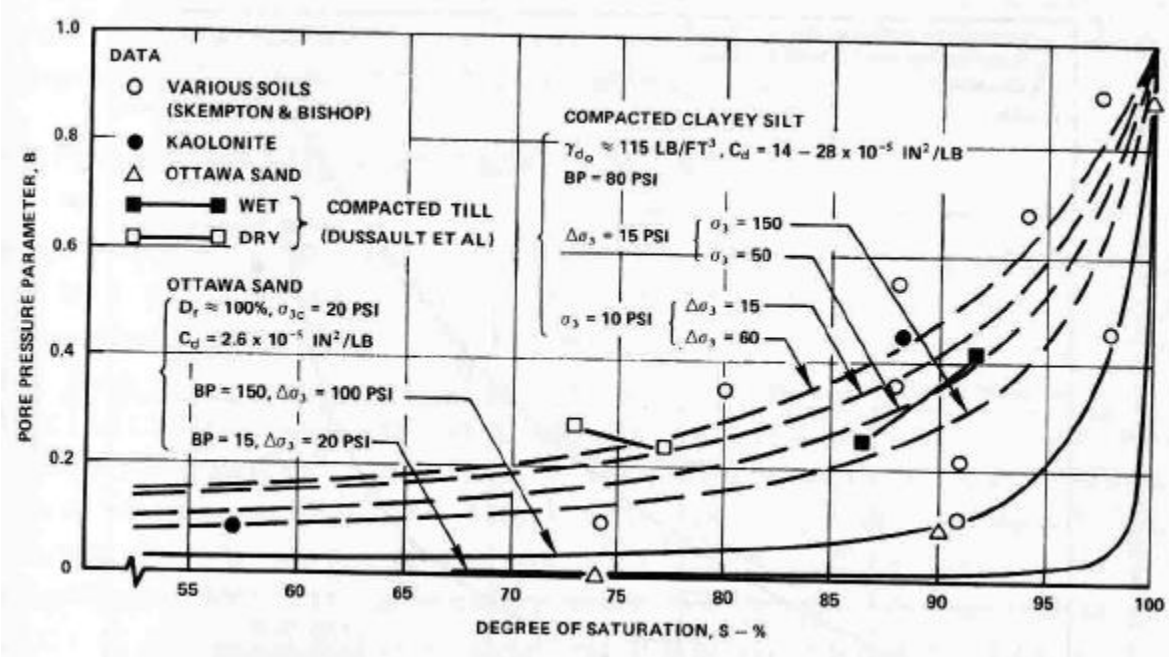

Figure 3.5: B-value versus saturation relations (Lee & Black, 1973)

The problem with achieving a fully saturated sand sample as part of a bigger project is that it requires several days to weeks, even with back pressures higher than P_{100}. The time required for saturation is the sum of the time required by water to flow into the sample and push the air out of the sample and the time required for pore air bubbles to dissolve into the surrounding pore water after being compressed. The former is a permeability problem and the latter is a diffusion problem. Sands have a high permeability so it doesn't take more than a couple of minutes for water to enter the pores and induce saturation; and so it is the diffusion process that governs the time taken for saturation.

Lesser the degrees of freedom of motion the air molecules have, the more is the time required for dissolution. For example, Lee & Black (1972) showed that small air bubbles suspended in a large container of water dissolved within hours, but the same bubble located in a small diameter tube (less freedom of motion) takes up to several days to dissolve. Thus it seems reasonable and has been shown by Lee & Black (1973) that complete dissolution of pore air bubbles will require many days. This is unacceptable if the project is to be completed on time, so it was suggested that for many soft and

medium stiff soils, a degree of saturation of 99.5 or even 99% be used instead of aiming for 100% saturation. Figures 3.6 a and b give the back pressure and time required respectively to achieve 99.5 and 99% saturation as a function of initial saturation.

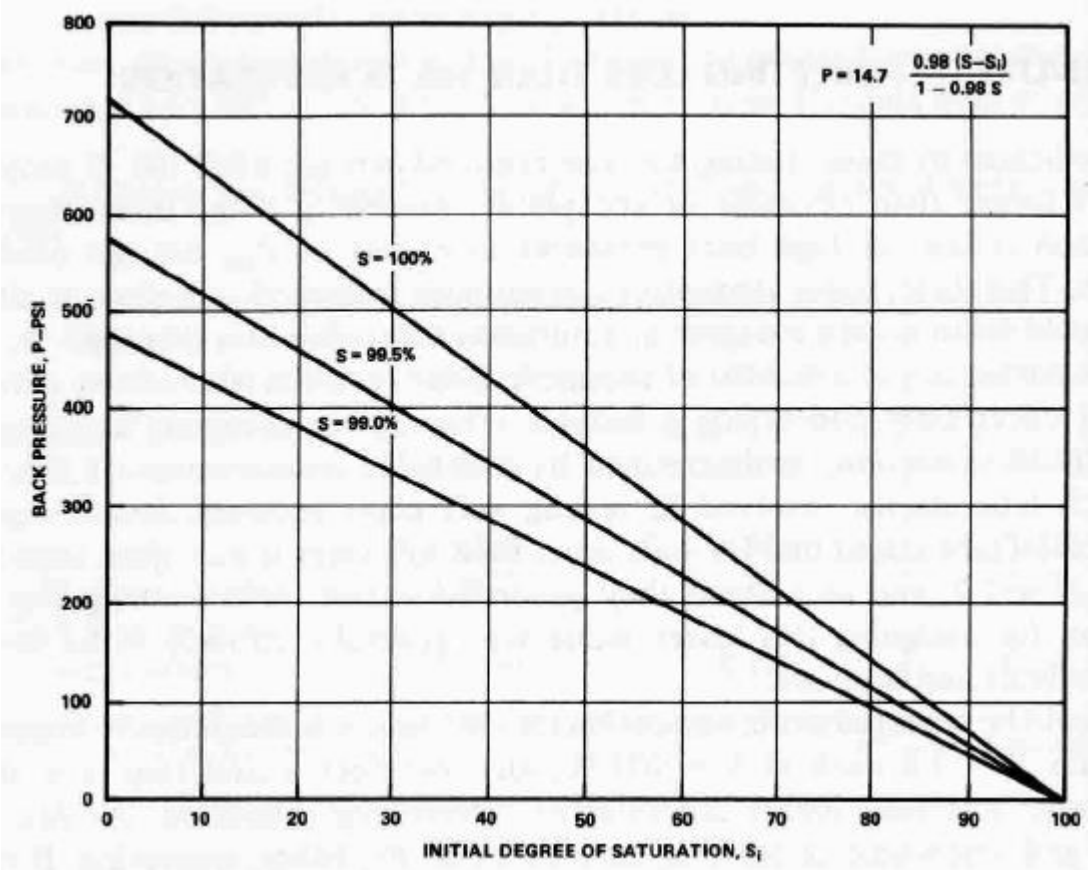

a

Figure 3.6: a) Back pressure required; b) time required to reach the desired saturation level

Figure 3.6 continued

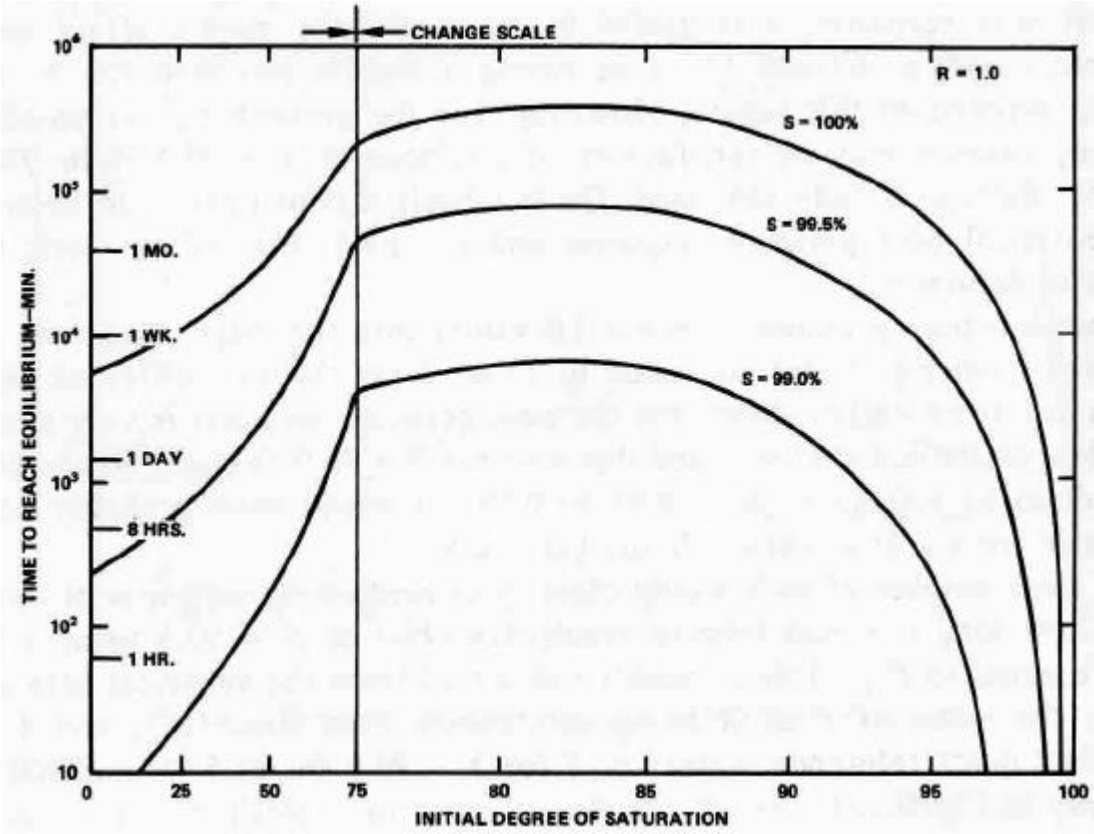

b

3.6. Precautions and sources of errors

The entire testing procedure requires utmost care, attention and precaution failing to which the test results will not be satisfactory or in some cases no results at all. A single act of carelessness at the beginning stage of the test may go unnoticed and get caught at a later stage thus rendering all the hours of work put into running that test useless. Hence it is worthwhile to note the more common sources of errors and the precautions that should be observed to overcome the errors.

The membrane used is a thin material made of latex and there is a high risk that it might get ruptured due to pinching by sand. The membrane is the barrier that isolates the inside of the sample from the outside, i.e., the membrane maintains the difference between cell pressure and pore water pressure. If,

however the integrity of the membrane is compromised by a rupture then the cell pressure and pore pressure will equalize, which is something that needs to be avoided. Before using a membrane it is best to check for ruptures by filling with water and making a balloon and compressing it. If water oozes out then it should be discarded. The membrane may also tear during sample preparation especially with coarse grained angular sand. Sand should never be allowed to stick to the lateral surface of the caps because the membrane will press against the lateral surface of the cap and any trapped sand can pinch it at a high cell pressure.

It is also very important to ensure that the surface of sand sample is flat and makes contact with the caps at all points. If the surface is not flat then the stress-strain plots might show abrupt jumps or kinks because of the variation in the resistance that the sample offers to the piston. Also it might lead to preferential failure of sample in one particular direction during shearing. If the sample does not make contact with the caps at all points then it is possible that we may miss on the wave signal that travels through the sand before hitting the cap. To ensure prefect contact between the caps and the sample, it is a good idea to place some weight on the top cap while unfolding the membrane from the split cell onto the top cap. But care must be taken to not put a lot of weight on loose samples to avoid any densification of the sample.

Sand, if trapped in the grooves of the pedestals, can prevent the perfect locking and tightening of the cylindrical cell and the leak will prevent the maintenance of a constant cell pressure. So it needs to be ensured that the groves are sand free.

The top triaxial cap should be placed in a way such that it is properly aligned with respect to the bottom cap so that we get visible signal on the oscilloscope.

Before locking the cylindrical cell it must be ensured that the wires coming out of the top pedestal are properly aligned for the oscilloscope to be able to read it. So a good practice would involve always checking for the signal on oscilloscope before placing and locking the cell and also immediately after

locking the cell. If at some point during the test, the oscilloscope does not read any signal or just shows a very vague signal then that test is no good simply because the bender element data is not retrievable.

3.7. Computational steps in data reduction

The raw data obtained from the 'TruePath' software at the end of a test are: external load cell, axial DCDT, cell pressure, back pressure, pore pressure, platen position, and pore volume. These data are a table of values in voltages at different instants of time. These voltages need to be converted to appropriate units to get the actual values of load, stress, volume, displacement etc. The external load cell measures the resistance offered by the sample to the piston as it moves down at a constant rate. The axial DCDT and the platen position give information about the strain at any time. The pressure transducers read the pressure, be it cell pressure (inside the cell but outside the sample), pore pressure (inside the voids of the sample) or back pressure (pressure applied by the pore pump inside the pores which should ideally be equal to pore pressure). The pore pump encoder gives the change in the volume of water entering or exiting the specimen.

Data reduction involves converting the voltage values into figures that make sense from geotechnical point of view and obtaining relevant plots from such values, namely deviatoric stress-axial strain plots and volumetric strain versus axial strain plots. Every transducer is associated with a 'calibration factor', an 'excitation' and a 'zero', the values of which are used to convert the voltages to load, displacement or pressure. Table 3.2 below gives the list of raw data obtained directly from the software while Table 3.3 gives the list of parameters obtained after reducing the raw data.

Table 3.2: Table of raw data from the software

External load	Axial DCDT	Cell pressure	Back pressure	Pore pressure	Platen position	Pore volume

The change in platen height is obtained by dividing the difference in platen position value in volts from its initial value obtained from the load frame encoder by its calibration factor. This change in platen height when divided by the initial height of the sample gives the strain which is used to calculate the area of the sample at any instant as per the following formula

$$area = \frac{original\ area}{(1 - strain)}$$

The axial force (in pounds) is obtained from the external load cell reading (in volts) using

$$Axial\ force = \frac{(Load\ cell\ reading - zero\ of\ load\ cell)}{excitation} * calibration\ factor$$

The deviatoric stress, σ1-σ3 is simply the axial force per unit area of the sample that is in contact with the top cap. Since the sample is enclosed within a rubber membrane which prevents it from falling apart, a part of the deviatoric stress that we obtain is due to the contribution of the membrane and it needs to be subtracted to obtain the stress that is taken by the sample alone. The cell, back and pore pressure and the pore volume are calculated from their transducer readings in the same manner as axial force by subtracting the 'zero', multiplying with the calibration factor and dividing by the 'excitation'. The cell pressure when added to the deviatoric stress gives the major principal stress, σ1. The stress-strain plot involves plotting σ1-σ3 against axial strain. The volumetric strain is obtained by dividing the change in pore volume by the initial volume of the sample and this is plotted against the axial strain. Finally, friction angle Φ is computed using

$$\sin(\Phi) = \frac{\sigma 1 - \sigma 3}{\sigma 1 + \sigma 3}$$

3.8. Test results

The figures numbered 1 through 13 in Appendix 1 give plots of principal stress difference and volumetric strain as functions of axial strain for all the tests performed for this project. Each plot corresponds to a particular sand type, a particular relative density and at a particular confining pressure.

Corresponding to each plot, a friction angle value at peak stress level and at critical state are obtained from the plots which is shown on the plots

Table 3.3: Summary of triaxial test results

Sand type	Confining stress (kPa)	Void ratio	Relative density (%)	Peak shear stress (kPa)	Residual Shear stress	Peak friction angle	Residual friction angle
Round dense	60	0.57	76.66	63.3	50.7	34.5	31
Round dense	30	0.58	73.33	37	28.1	37.3	32.6
Round dense	15	0.53	90	20.22	15	38.9	33.8
Round dense	5	0.53	90	11.3	8.2	47.5	42.2
Round loose	60	0.8	0	47.2	47.2	29.8	29.8
Round loose	30	0.71	28.1	26	26	31.33	31.33
Round loose	15	0.8	0	13.6	13.6	32.1	32.1
Round loose	5	0.72	26.6	7.97	7.97	41.7	41.7
Angular dense	60	0.89	70	76.3	55.4	37.8	32.4
Angular dense	30	0.8	100	38.1	31.3	38	34.5
Angular dense	15	0.8	100	20.8	16	39.4	34.9
Angular loose	60	1	33.3	49.33	49.33	30.4	30.4
Angular loose	30	1.03	23.3	27.5	27.5	32.3	32.3

Table 3.3 continued

Sand type	Confining stress (kPa)	Void ratio	Relative density (%)	Peak shear stress (kPa)	Residual Shear stress	Peak friction angle	Residual friction angle
Angular loose	15	1.02	26.6	14.5	14.5	33.17	33.17

3.9. Conclusions

There are three components contributing to the strength of sand: frictional resistance, strength developed by energy required to cause dilation of the material, and strength developed by energy required to rearrange and reorient grains. The frictional character is influenced primarily by the nature of contacts between sand particles and as such, it was observed that angular sand has higher strength than rounded sand for the same confinement because of greater degree of interlocking among grains. Also the strength increased with increasing confining pressure (figures 3.18 through 3.21) which is consistent with Mohr's Coulomb failure criterion. Higher the inter-particle contact forces, higher will be the force required to make the grains slip past one another. When a dense sand was sheared, the grains tended to tangle which mobilized more friction and therefore higher peak shear strength than loose sand.

Some studies suggest that friction angle increases with increase of uniformity coefficient for sands containing feldspar and calcite but for sands that predominantly contain quartz, there is no link between these two parameters. And thus for samples with the same void ratio, the size of particles doesn't influence the friction angle. However, Mustafa Kara et al. (2013) conducted direct shear tests on samples of sand with the same void ratio and different particle sizes and found considerable variations in friction angle.

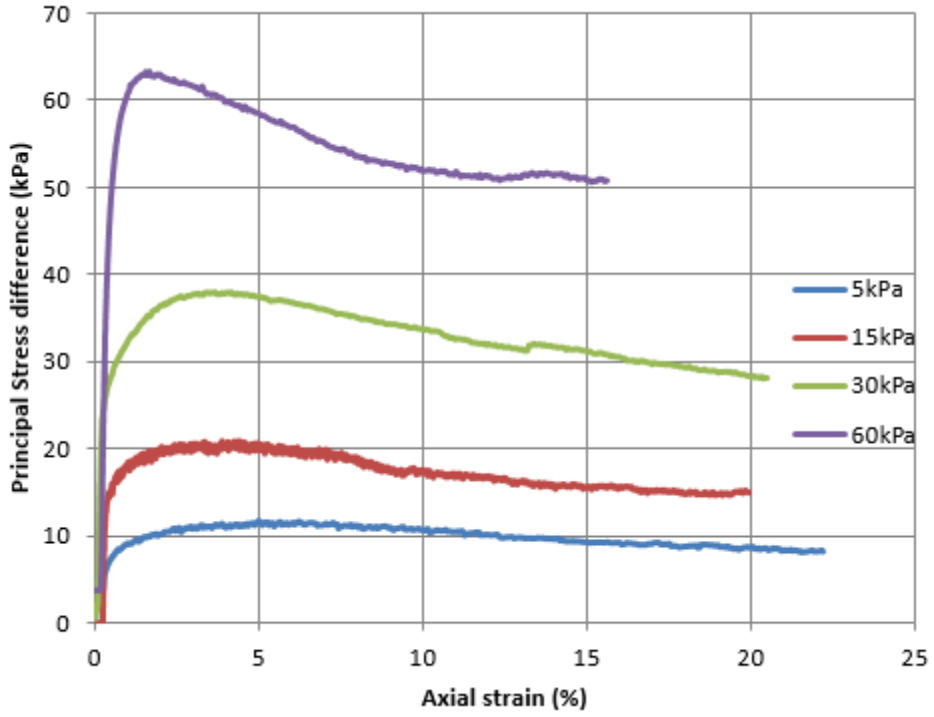

Figure 3.7: Round dense sand plots at different confinement

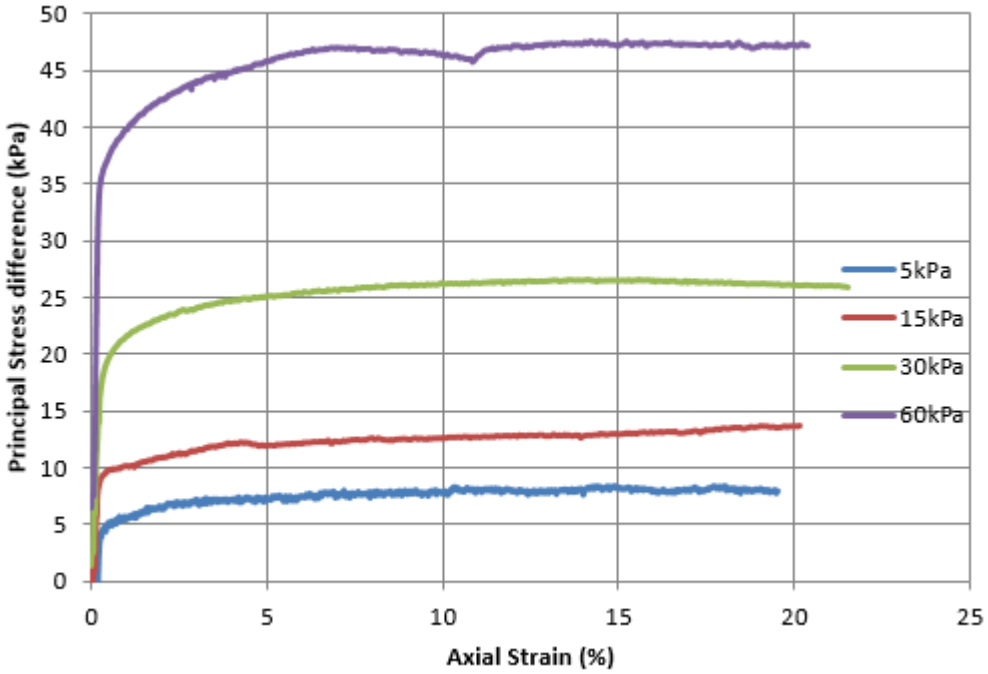

Figure 3.8: Round loose sand plots at different confinements

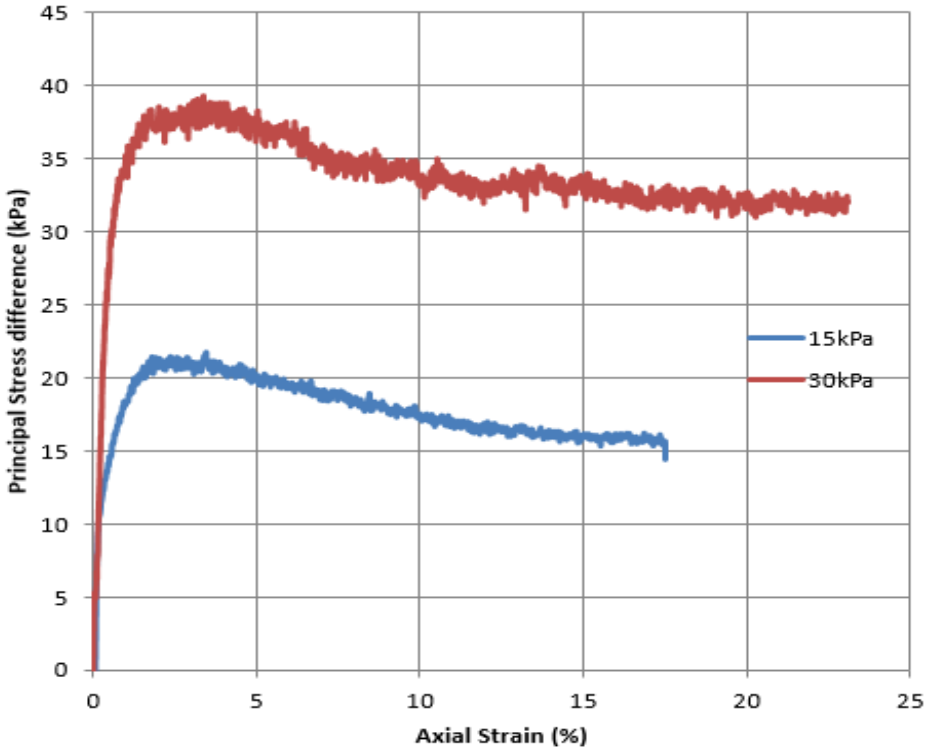

Figure 3.9: Angular dense sand plots at different confinements

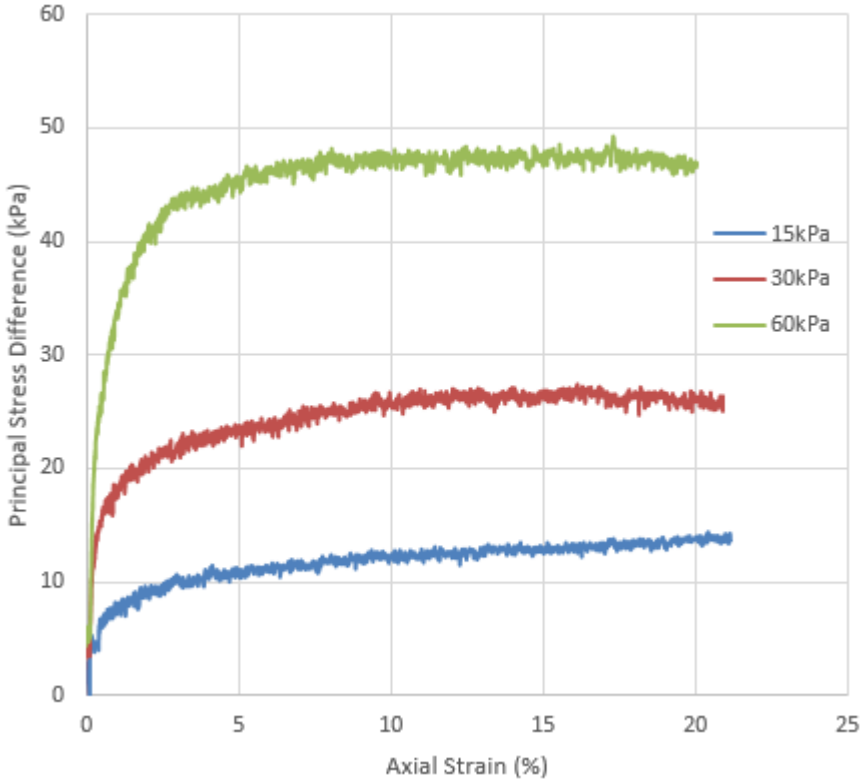

Figure 3.10: Angular loose sand plots at different confinements

The study described in this paper resulted in angular sand having friction angles which is about 1^0 higher than the rounded sand for the same confining stress. It is worth noting that the loosest state of angular sand coincided with the densest state of rounded sand, as far as void ratio is concerned and thus, a fair comparison would be to compare loose round sand with dense angular sand in which case the difference in friction angle is of the order of 3 degrees.

Friction angle decreased with increasing confining pressure. The result is that the peak strength envelope is curved in the Mohr-Coulomb plot. Ud-din et al. (2011) in their study concluded that regardless of the material tested, the friction angle reduced with increasing effective confining stress (Figure 3.22) which corroborates the findings of this study.

The soil behaved linearly at very low values of strain (~10^{-3}%) after which the behavior was non-linear. Peak shear strength developed further at around 1-4 % axial strain for dense sand. 'Critical state' which is characterized by shearing progressing with no volume change, was not observed for most samples and the samples were sheared to 20% strain thus suggesting that the samples needed to be sheared further (beyond 25%) to attain critical state. The loose sand contracted and the dense sand dilated (after initial contraction) as they approached critical state. The maxima of the rate of dilation seemed to coincide with the peak in shear strength for dense sands beyond which the shear stress dropped. Irrespective of the initial relative density of the sample for a given confining pressure, the final near-critical state shear strength was the same.

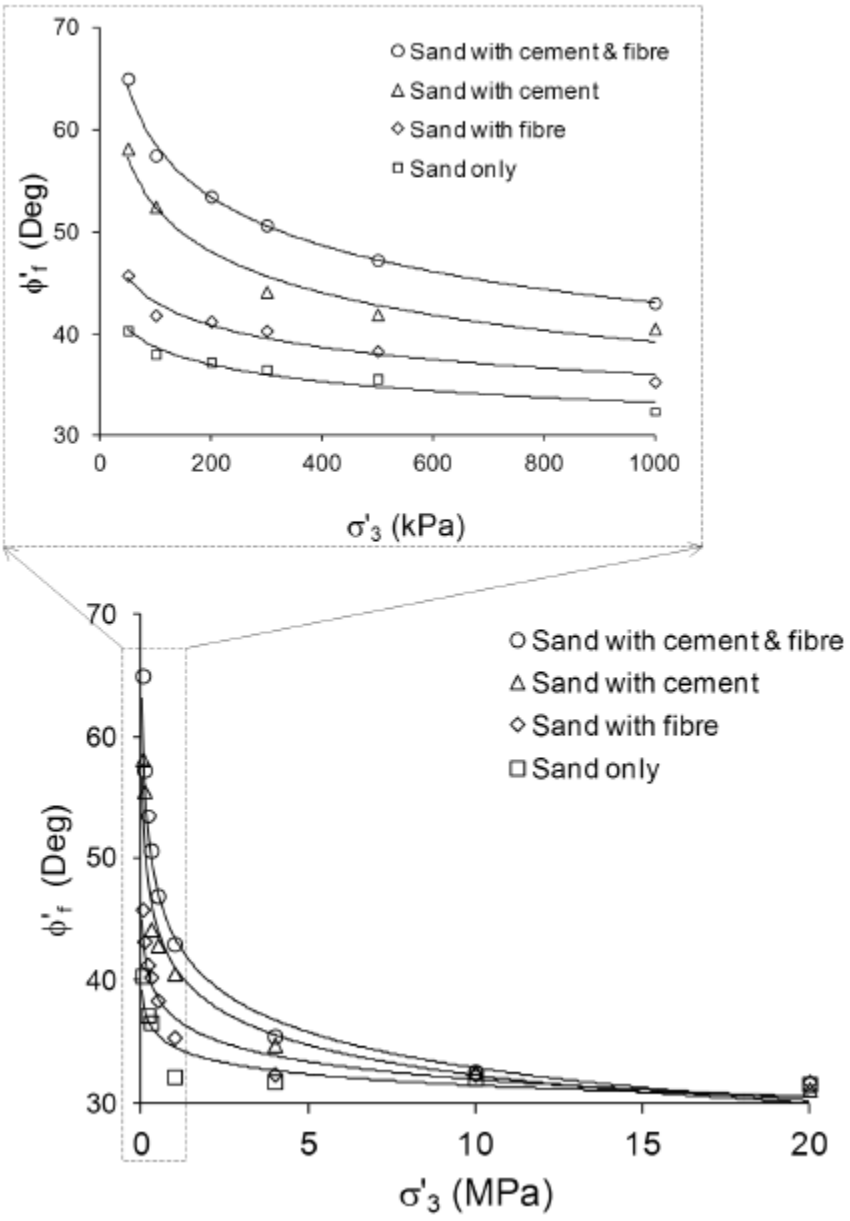

Figure 3.11: Dependence of friction angle on effective confinement (Ud-din et al. (2011))

CHAPTER IV

BENDER ELEMENT TESTING

4.1. Introduction

The bender element (B.E) is an electromechanical transducer capable of converting mechanical energy into electrical signals and vice versa. When a driving voltage is applied to the bender element, the polarization will cause a bending displacement and, thus, the bender element acts as a signal generator. When the element is forced to bend, a voltage is generated and, thus, the bender element acts as a signal receiver (Leong et al 2005). The use of bender element/ ultrasonic testing to measure shear wave velocity is popular due to its simplicity. The ASTM standard D 2845-95 standardizes the method for determination of small strain elastic constants for rocks. This method is not used so frequently for soils due to their higher damping characteristics which results in the signal being transmitted to be weak and noisy and hence difficult to measure. Signal processing is necessary for soils to enable wave travel time estimation (Leong et al. 2004).

There are many uncertainties in the interpretation of this test. The results depend on characteristics of the bender elements and of the waveform, magnitude and frequency of the applied voltage and the method employed for determining the travel time (Leong et al. 2005).

Bender elements are now commercially available and are being increasingly used in laboratory soil testing for determining S- wave velocity. However, the use of compression wave (P-wave) piezoceramic elements is not as widespread for the following reasons: i) the shear modulus is more applicable to describe deformation behavior of soil as soil is loaded mostly in shear mode and ii) this is an ineffective method for measuring P-wave velocity in saturated soils as the P-wave travels through water phase faster than through the soil skeleton. However, with growing interest in unsaturated soil mechanics, P-wave velocity measurement becomes more important as it can provide an assessment of the degree of saturation as well as porosity of the soil specimen.

4.2. History & mechanism

Lawrence (1963 1965) pioneered the concept of using piezoelectric elements for geotechnical applications by using piezoelectric crystals to generate 1D compression waves through sand and glass beads while shear waves was generated and received in laboratory tests first by Shirley (1978). These days bender elements are used in a number of geotechnical testing apparatuses. Bates (1989), Brignoli et al. (1996), and Pennington et al. (2001) measured shear wave velocity in triaxial specimens using piezoceramic bender elements. Dyvik and Madshus (1985) measured small strain stiffness, Gmax , of soil specimens in resonant column, oedometer, and direct simple shear apparatuses using bender elements. Kawaguchi et al. (2001) measured Gmax in an oedometer using bender elements. Agarwal and Ishibashi (1991) used bender elements in a triaxial cubical box device. Blewett et al. (2000) measured shear wave velocity of saturated sand using bender elements in a large container. However, to date the bender element test has not been standardized.

Bender elements consist of two sheets of piezoelectric ceramic material such as lead zirconate titanate (PZT), barium titanate or lead titanate sandwiching a center shim of brass, stainless steel, or other ferrous nickel alloys to add strength to the system. Table 4.1 shows the various types of bender elements used by different researchers.

Table 4.1: Bender elements used by researchers in past

Researcher	Bender element used
Shirley& Hampton (1978), Bates (1989)	PZT4
Brignoli et al. (1996)	PZT5A and PZT5HN
Agrawal & Ishibashi (1991)	PZT5A
Pennington et al. (2001)	PZT5B

4.3. Test principles and sources of errors

In the bender element test for measurement of shear wave velocity a pair of bender elements was used, each element being installed in each triaxial cap, whereby one of the elements acts as a shear wave transmitter and the other acts as a receiver. A schematic diagram is shown in Fig. 4.1. By measuring the travel time of the wave, the wave velocity is determined as follows (Viggiani and Atkinson 1995):

$$Vs = \frac{Ltt}{t}$$

Where Ltt is the tip to tip distance between the transmitter and receiver bender element and t is the travel time of the wave from transmitter to receiver. From Vs, the shear stiffness G_{max} can be determined from the elastic wave propagation theory:

$$\mathrm{Gmax} = \rho \mathrm{Vs}^2$$

Where ρ is the total density of the soil specimen.

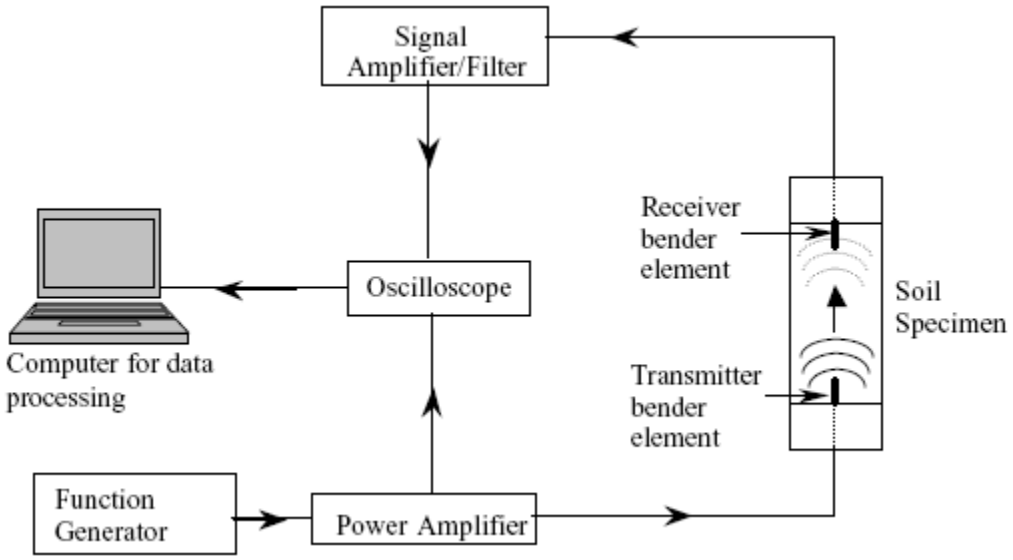

Figure 4.1: Bender element test setup (Leong et al, 2005)

The potential error in shear modulus ΔG_0 is given by (Viggiani and Atkinson 1995)

$$\frac{\Delta G0}{G0} = \frac{\Delta \rho}{\rho} + 2\frac{\Delta l}{l} + 2\frac{\Delta t}{t}$$

Where $\frac{\Delta\rho}{\rho}, \frac{\Delta l}{l}, and\ \frac{\Delta t}{t}$ are the relative errors in density, length of sample and travel time respectively.

The density of a cylindrical soil sample can be precisely measured by direct measurement but errors can occur while determining l and t. The length of the triaxial sample is usually 127 mm and bender elements protrude 3mm into each end of the sample so the maximum error connected with the choice of l is 6 mm or 4.7%.

From the oscilloscope signals obtained, it was observed that the instant of transmission of the shear wave is clearly defined but its arrival at the receiving end is not. There is the first deflection of the signal after which the intensity increases gradually up to a point where there is a sharp inversion and thereafter the signal fades after a number of crests and troughs. Depending on whether we choose the point of deflection or the point of reversal of signal or a trough as the first arrival, the uncertainty in arrival time is $\pm 0.142ms\ in\ an\ average$ travel time of 0.5ms, an error of about $\pm 30\%$, which corresponds to an error of 60% in G_0 (Viggiani and Atkinson 1995).

The output signal from the receiving bender is not just measuring incident waves but also reflected waves and there is no way to isolate these two. The finite size of the soil specimen results in reflection and refraction of the wave at the sample boundaries as it travels along the length of the sample. The interference of reflected and incident waves at the rigid boundary can affect the interpretation of travel time.

The transfer functions used to obtain electrical signals from the physical wave forms are associated with phase and time lags which are different at the receiver and transmitter bender elements.
We don't take into account non one dimensional wave travel and near field effects (Viggiani and Atkinson 1995).

4.4. Bender element characteristics

Relationship between the applied forces and the resultant responses depend upon the piezoelectric constants of the ceramic, size and shape of the element, and the direction of the electrical or mechanical

excitation, since B.Es are anisotropic. Piezoelectric strain constant is a measure of strain developed per unit applied electric field. So large strain constants relate to large mechanical displacements. Piezoelectric voltage constant is a measure of the magnitude of electric field generated by the piezoceramic material per unit of mechanical stress applied. Typical values of these constants are illustrated in table 4.2.

The length, width, and thickness of B.E are important because they determine the tip deflection of the transmitter element and the output voltage from the receiver element, which also depend on protrusion length of the B.E, l_b. l_b ranges from 3 to 6 mm. Choosing a wider B.E increases the maximum force generated by transmitter B.E, F_{max} and reduces the output voltage from receiver B.E. Hence for the receiver, usually a narrow B.E is preferred. A thicker B.E decreases tip deflection and increases F_{max} of transmitter B.E and reduces output voltage from receiver B.E.

Table 4.2: Piezoelectric constants of commercially available B.E from SPK Electronics Company Ltd., Taiwan (Leong at al., 2005)

Piezoelectric constant	Bender Element type			
	PZT4	PZT5A	PZT5B	PZT5H
Elastic Modulus ($*10^{10}N/m^2$)	7.9	7.4	7.4	5.9
Strain Constant ($*10^{-12}$ m/V)	-125	-170	-180	-275
Voltage constant ($*10^{-3}$ Vm/N)	-11.4	-10.6	-10.6	-9

4.5. Influence of applied voltage on signal received

The output signal received on the oscilloscope depends on the waveform, magnitude and frequency of applied voltage, in addition to soil type.

Sinusoidal wave is preferred over square wave because the square wave causes greater ambiguity in arrival time, the receiver signals of the square wave do not resemble the input signal, and they have more distortions at the beginning of the receiver signal. Figure 4.2 shows the influence of the waveform chosen on receiver signals for three different soil. Sinusoidal wave was found to be a better choice than square wave as the distortion of the receiver signal at the beginning is greatly reduced.

The magnitude of applied voltage does not affect the appearance of the receiver signal but increases the signal to noise ratio (SNR). This is because a higher input voltage generates a stronger shear wave relative to near field effects and minimizes the distortion of received signal. But depolarization and eventual failure of the B.E has to be avoided so there is a maximum limit to the applied voltage. Figure 4.3 shows the influence of applied voltage on received signal on three different types of soils. As the voltage is increased, the peaks are sharper and more distinct and the intensity of power spectrum magnitude of the receiver signal increases so it is easier to tell the arrival of a wave (Leong et al., 2005). Frequency of input signal decides whether or not near field effects will be significant which may mask the shape of receiver signal thus rendering determination of arrival time difficult. The use of high frequency wave was recommended to ensure the separation of coupled S and P waves and to reduce the near-field effect. For a given wave velocity, wavelength decreases as frequency increases and it was shown by Sanchez-Salinero et al. (1986) that near-field effects are significant when the length of sample to wavelength ratio is less than unity. Figure 4.4 shows the effect of frequency of the pulse on receiver signal for mudstone residual soil specimen.

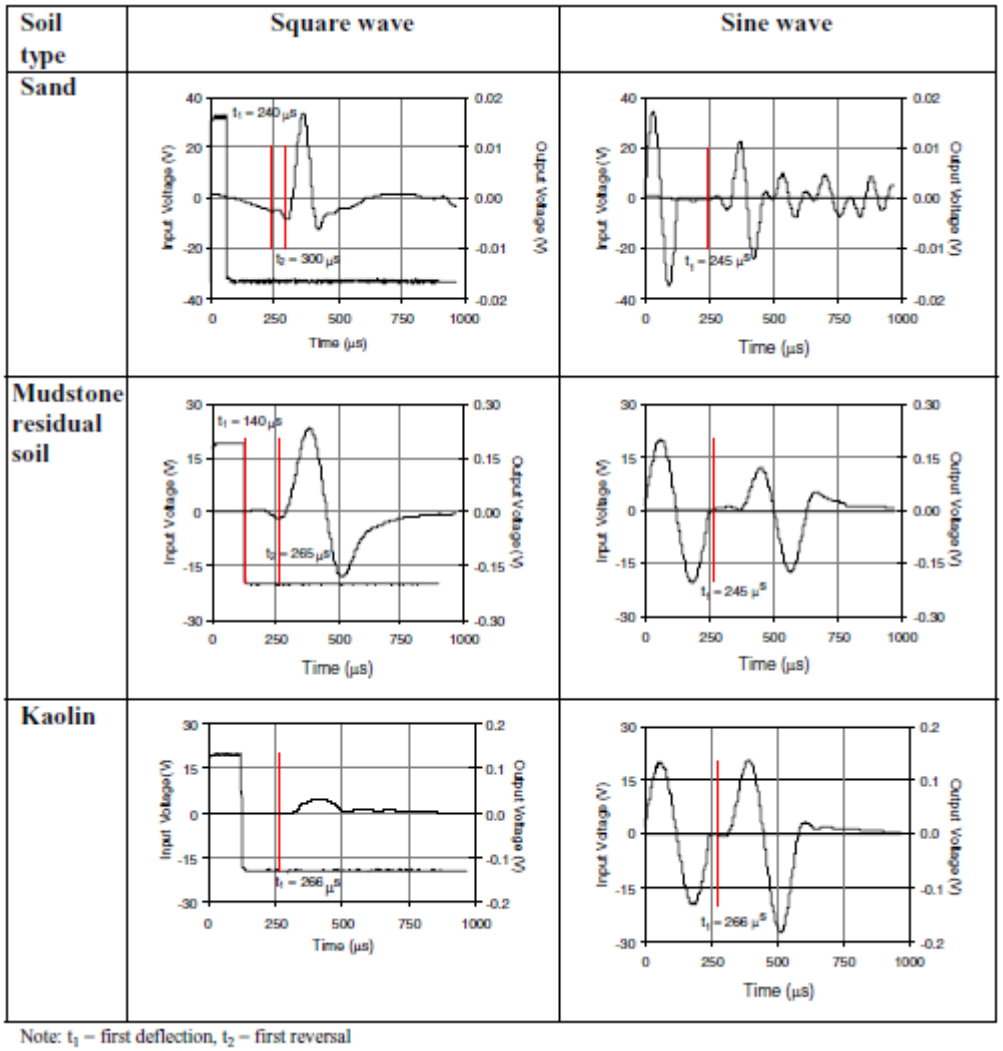

Note: t_1 – first deflection, t_2 – first reversal

Figure 4.2: Effect of waveform on receiver signal (Leong et al., 2005)

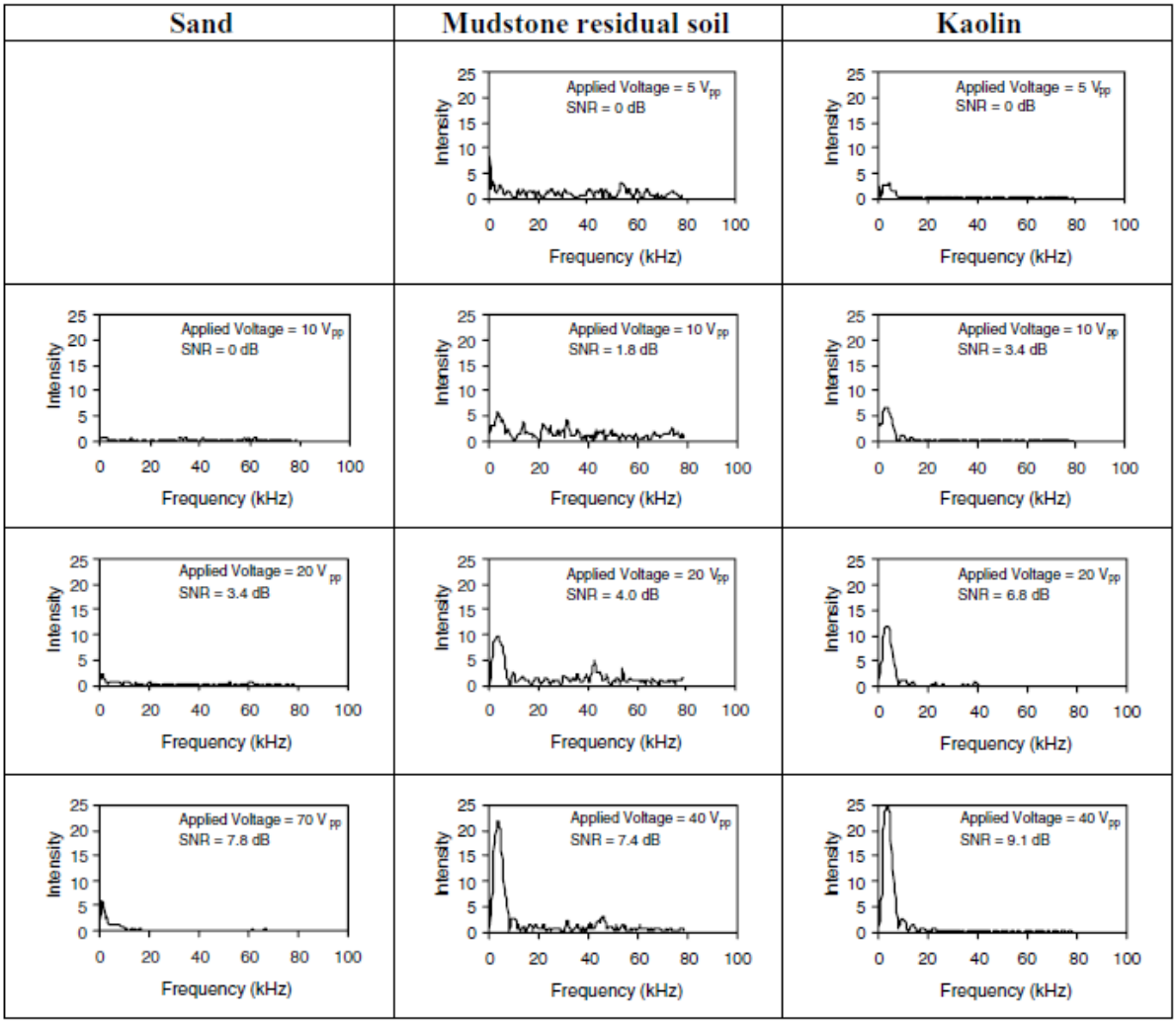

Figure 4.3: Influence of applied voltage on receiver signal. (Leong et al., 2005)

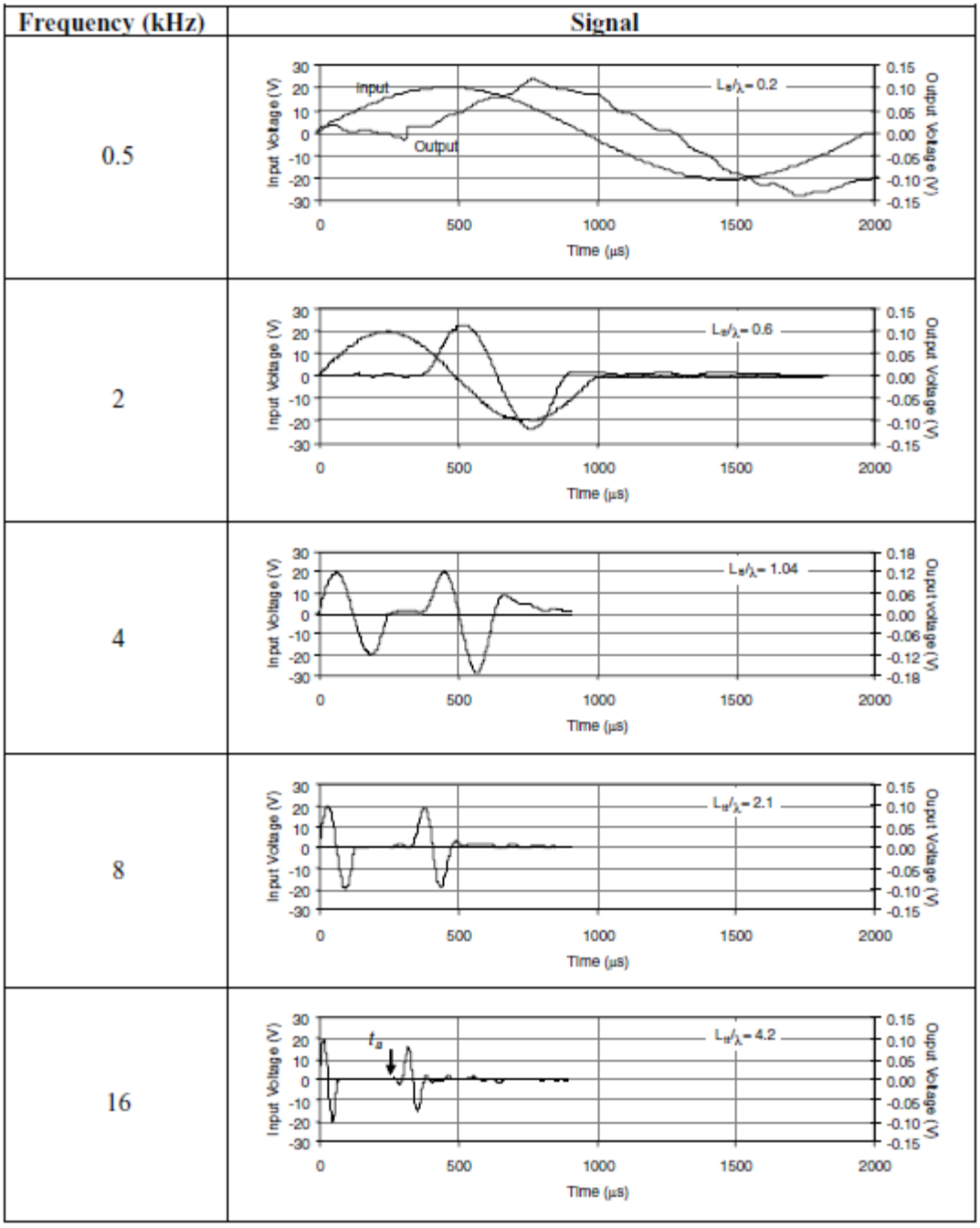

Figure 4.4: Influence of frequency of pulse on receiver signal (Leong et al., 2005)

4.6. Ultrasonic test system

There are three modes of operation in an ultrasonic test system (Kundu 2000): pulse echo, through transmission, and pitch catch. In the pulse-echo mode, both pulse generation and pulse detection occur on the same transducer. In the through-transmission mode, one transducer generates the pulse while the

other detects it so there are two transducers. In the pitch-catch mode, these two transducers are on the same side of the specimen. The through-transmission mode is more suitable for measuring wave velocities and attenuations of geomaterials (Krautkrämer and Krautkrämer 1990). The ultrasonic test system used in this study operates in the through-transmission mode. The caps in the triaxial apparatus were equipped with piezoelectric transducers, manufactured by GCTS Testing Systems and fit the GEOTAC setup. One set of caps had bender elements (protruding from the caps) and p-crystals installed while the other set had both p and s-crystals (mounted under the surface of the cap) installed. The system is completed by a Tectronix arbitrary function generator AFG320, a Tectronix oscilloscope TD3014B and TDS3GV and a Piezosystems PiezoLinear amplifier. Placement of transducers is shown in Figure 4.5.

4.7. Methods for determining travel time

The following five methods for determining the travel time from the results of ultrasonic tests are explained by Viggiani & Atkinson (1995):

i) Travel time to first direct arrival in output signal

Travel time of an impulse wave between two points in space may be taken as the time between the first direct arrival of the wave at each point. In applying this approach to our test, travel time has been estimated as the time between the start of the voltage pulse input to the transmitting bender and the first deflection in the output signal although the first arrival point is ambiguous.

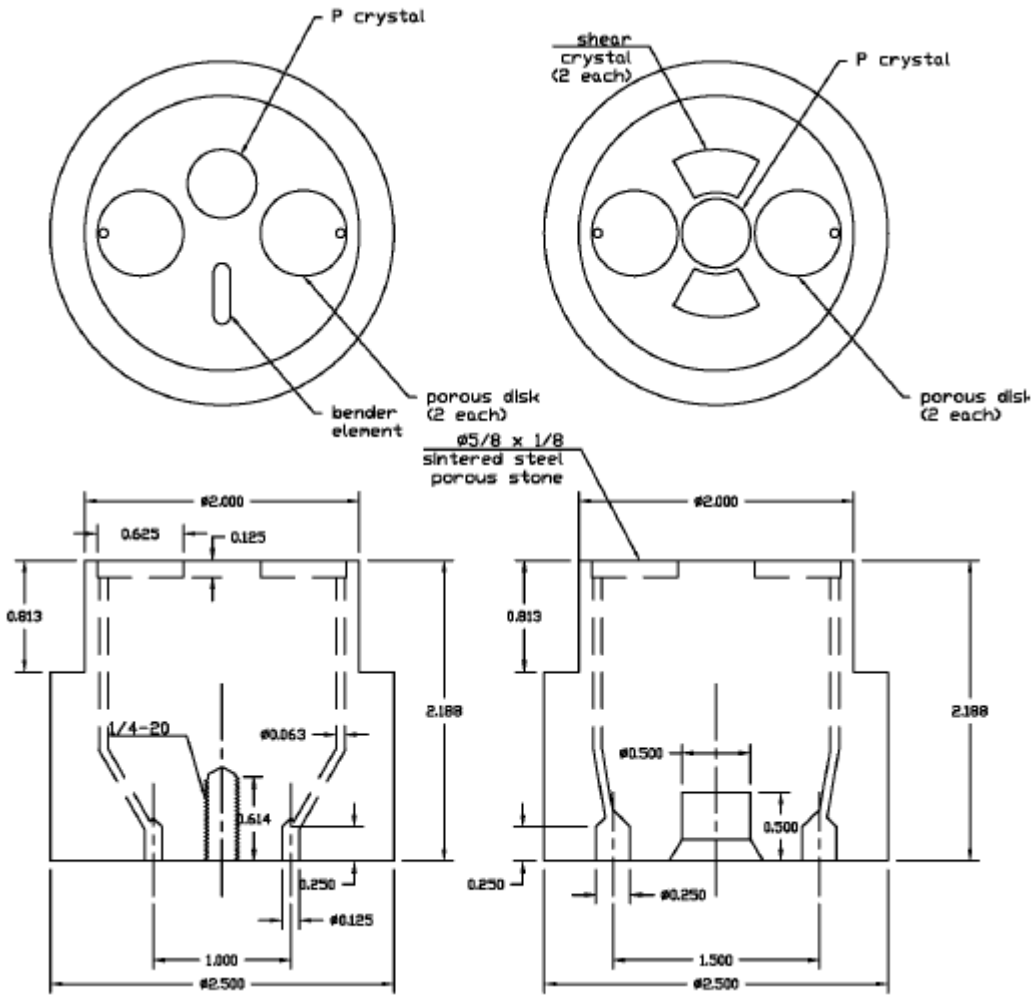

Figure 4.5: Triaxial caps with placement of bender elements and p and s piezoelectric crystals

ii) Travel time between characteristics peaks of input and output signals

Travel time of an impulse wave between two points in space may also be taken as the time between either the first peak or first trough or zero crossing in the signals recorded at these two points.

iii) Travel time by cross correlation of input to output signals

Numerical analyses are carried out on oscilloscope signals. The time domain record is decomposed into a group of harmonic waves of known frequency and amplitude using the fast fourier transform (FFT) algorithm. The cross correlation function $CC_{xy}(t)$ is a measure of the degree of correlation of the input and the output signal. The analytical expression of the cross correlation function is

$$\mathrm{CCxy(t)} = \lim_{\mathrm{Tr}\to\infty} \frac{1}{\mathrm{Tr}} \int_{\mathrm{Tr}} \mathrm{X(T)Y(T+t)dT}$$

Where Tr is the time record and t is the time shift between the signals.

The linear spectrum $L_x(f)$ of a signal X(T) is a function of frequency and is given by

$$\mathrm{Lx(f)} = \mathrm{FFT(X(T))}$$

It's a vector in the complex field; its magnitude and phase are respectively the amplitude and phase shift of each of the harmonic components of the signal.

The cross power spectrum $G_{xy}(f)$ of two signals X(T) and Y(T) is defined as

$$Gxy(f) = Lx(f) * Ly'(f)$$

Where $\mathrm{Ly'}$ is the complex conjugate of the linear spectrum of Y(T).

For each frequency, the magnitude and phase of the cross power spectrum are respectively the product of amplitudes and the phase differences of the components of the two signals at that frequency.

It can be concluded that $CC_{xy}(t)$ is the inverse FFT of $G_{xy}(f)$. The cross correlation analysis is based on the assumption that the travel time is equal to the time shift t that maximizes the cross correlation function. Thus t represents the travel time of the whole waveform.

It is convenient to calculate the cross correlation in the frequency domain in the following manner. First the linear spectra of the input and output signals are obtained using the FFT algorithm and then the cross power spectrum is obtained by multiplying them. And finally the cross correlation function is obtained by taking the inverse fourier transform of the power spectrum. These calculations take only a few steps in MATLAB and are no longer an onerous task.

iv) Travel time by Phase Velocity

From the phase of the cross power spectrum that we calculated above, it is possible to determine the phase velocity of each frequency component as

$$V(f) = \lambda * f = 2\pi \frac{L}{\Phi(f)} f$$

Where $V(f)$ is the phase velocity of each frequency component, $\Phi(f)$ is the phase of the cross power spectrum, f is the frequency, $and\ \lambda$ is the wavelength.

A cross power spectrum phase diagram is plotted which is a plot of the phase angles of each frequency component in degrees against that frequency. Let's call the slope of this plot as α. Then the group travel time is given by

$$Tg = \frac{\alpha}{2\pi}$$

v) Travel time using the second arrival in the output signal

Output signals also show a clear second arrival of the input wave. The second arrival is just the input wave after it reflects from the receiver cap, travels back to the transmitter cap where it reflects again, and returns to the receiver cap a second time. Assuming plane wave propagation, the time between first and second arrivals in the output signal is equal to twice the travel time of wave from cap to cap. The travel time may be determined using either the characteristic peaks or cross correlation methods. For the latter method, it is useful to decompose the output signal into two dummy signals, both being modified copies of the original output signal. The first dummy signal is obtained by setting to zero the signal outside the time frame of the first arrival and for the second dummy signal, the signal is set to zero outside the time frame containing the second arrival.

4.8. Recommendations

Parametric studies of the propagation of elastic waves in an elastic medium by Mancuso and Vinale (1988) show that the near field effects may mask the arrival of the shear wave when the distance between the source and the receiver is in the range of ¼ to 4 times the wavelength. As per Viggiani and Atkinson (1995), near field effects are prominent when L/λ_s is below a limiting value, L being the sample length. When $L/\lambda_s > 2$ and when $L/D > 2$ then there is very little effect of L/λ_s and L/D ratios on the shear wave velocity.

Signal processing was required because the signal is weak and very noisy and hence to improve the quality. Stacking of signals helps to reduce random noise. Nakagawa et al. (1996) stacked 100 signals to obtain a clear signal. Stacking was applied to a series of S- and P- wave signals and the signals showed minimal improvement beyond 12 signals. For our project a stacking operation involving 8 signals was adopted.

For a reliable measurement of P-wave velocity, ASTM standard D2845-95 further recommends that the minimum lateral dimension (diameter) be at least 5 times the wavelength and the wavelength should be at least 3 times the average grain size. The former restriction is due to the dispersion phenomenon. Dispersion arises due to interaction of the wave with the boundary of the system causing wave mode conversion, which won't occur if diameter is more than 5 times the wavelength. The effect of D/λ_p has been studied by Curtis (1969) who explained that the head of a wave pulse will propagate at the unbounded velocity V_p. As λ_p increases to greater than the specimen's diameter, the velocity approaches the one dimensional velocity, V_1 given by $\sqrt{\frac{E}{\rho}}$ asymptotically. Therefore depending on the D/λ_p ratio, the P-wave velocity measured by an ultrasonic test may range from V_1 to V_p.

4.9. Example of data reduction

The cross correlation method was adopted as it is the simplest approach and has been shown to yield correct results by many researchers. Summarizing the steps, first we obtain the linear spectra of input and output signals by taking their Fast Fourier Transform. On multiplying the linear speactras (after taking the conjugate of one of them), we obtain the cross power spectrum. From the cross power spectrum, we obtain the cross correlation function by taking the inverse FFT. Then we normalize it by dividing by its maximum value. And finally we plot the cross correlation function against time. Now, as discussed earlier in this chapter, the travel time is the time shift which maximizes the cross correlation function, so we look for the highest peak in the plot. The time corresponding to the highest

peak gives the value of travel time. The "appropriate" height of the sample is then divided by this time to get the velocity.

This section shows through an example how shear wave velocity and shear modulus were obtained from the input and output signals obtained from the oscilloscope. 15 kPa dense angular sand test is chosen to illustrate the approach chosen.

Sample	Angular sand
Stress level	15kpa
Classification	Dense
Void ratio, e	0.8
Density $(G_s*\rho_w+S*e*\rho_w)/(1+e)$	1916.66 kg/m^3

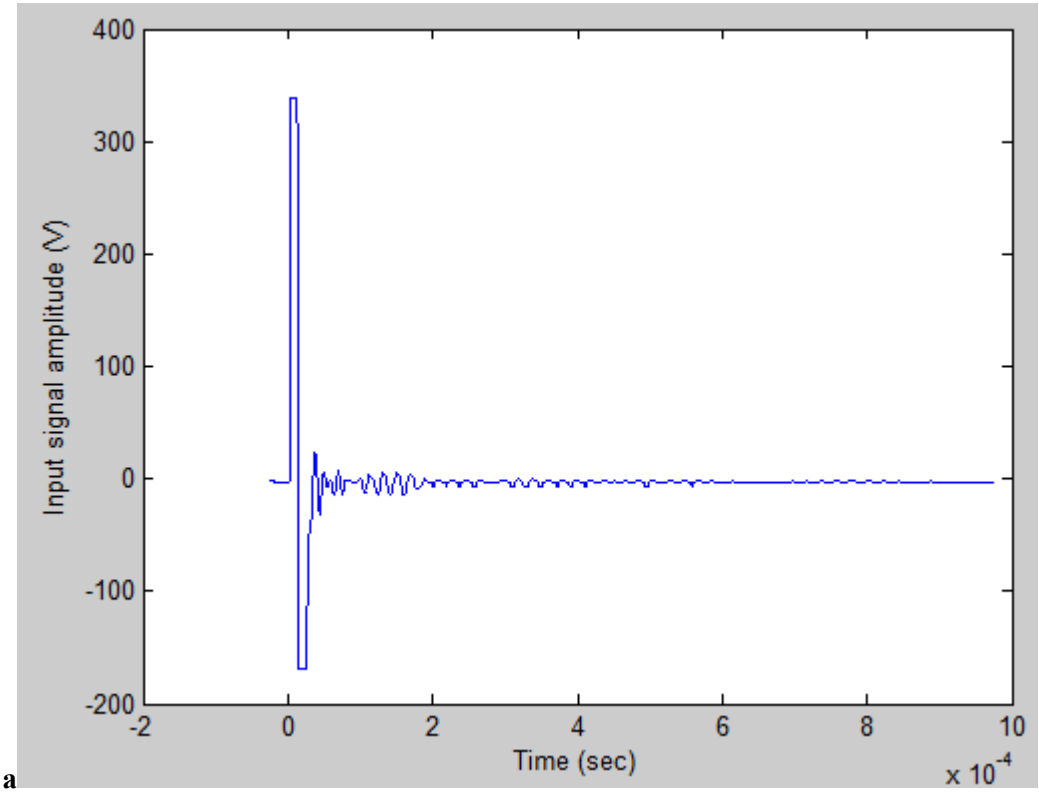

a

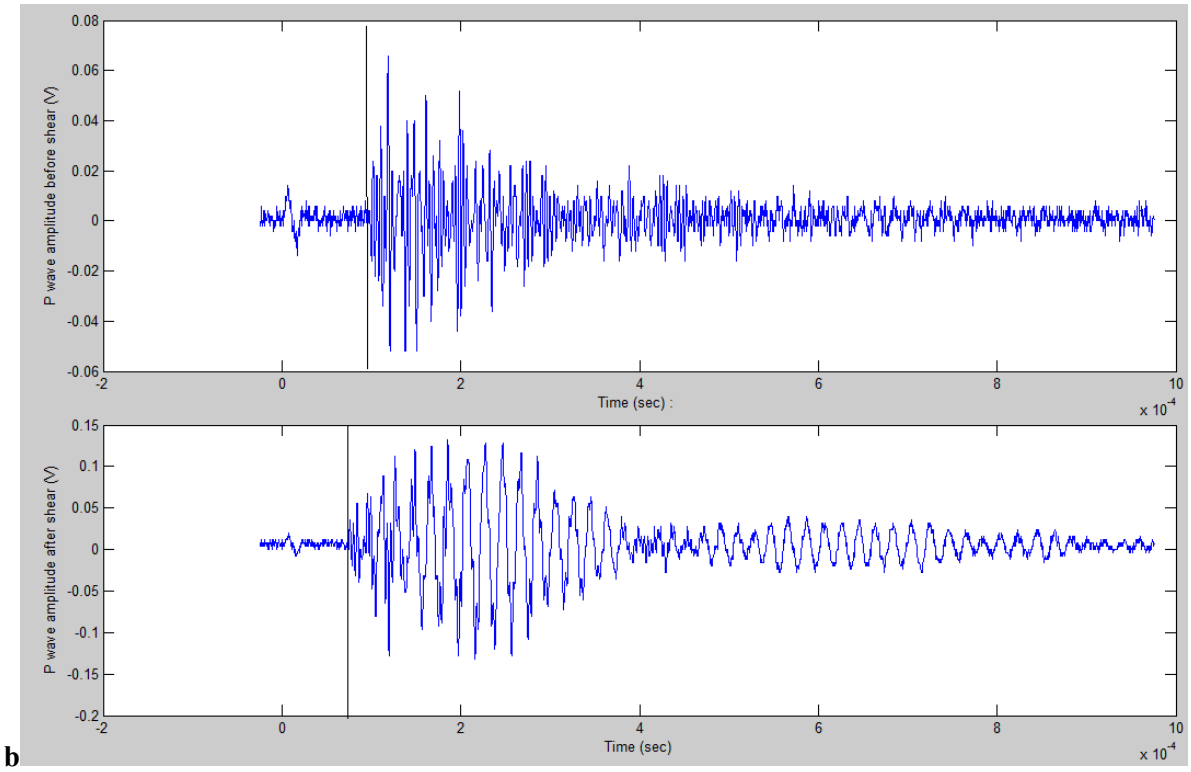

b

c

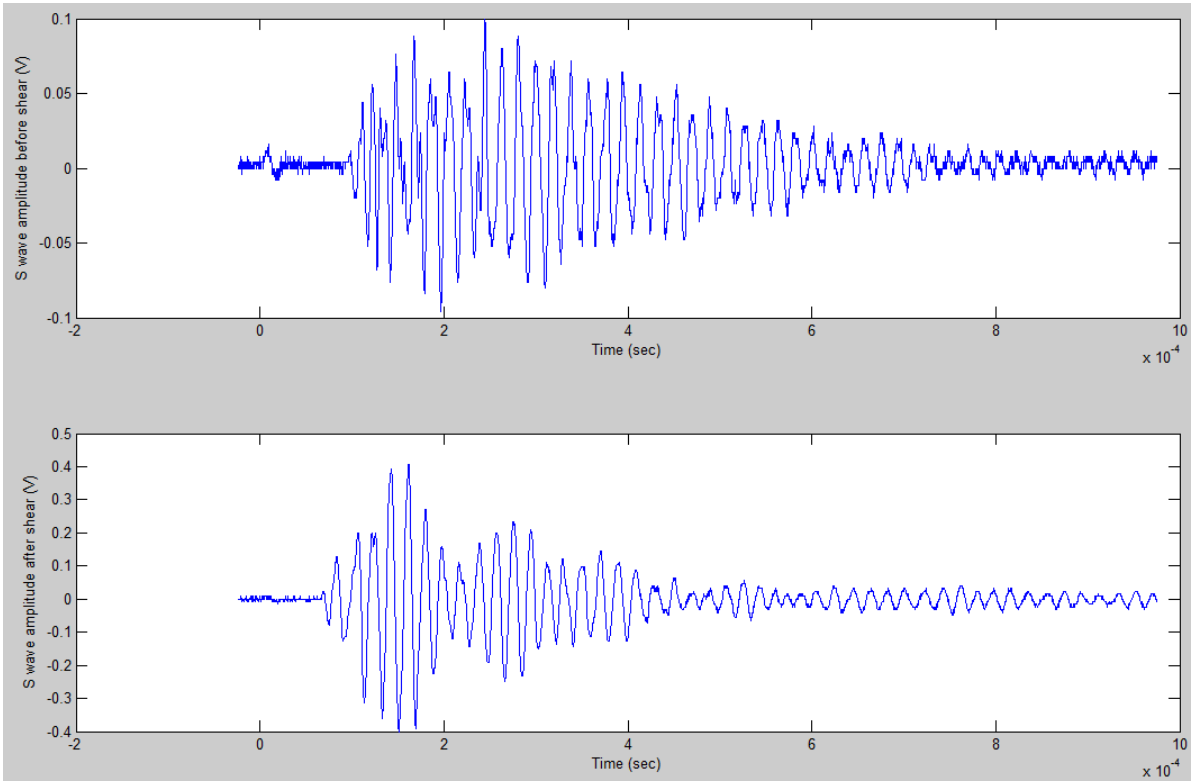

Figure 4.6: Plots obtained from oscilloscope- a) Input signal, b) P-wave profile before and after shear, and c) Shear wave profiles before and after shear.

P-wave arrival is directly taken as the first arrival from the plot without any manipulation. As can be seen from the plot, arrival time, t_a before shear = $2.68*10^{-4}$ s and t_a after shear = $2.42*10^{-4}$ s (the location of vertical black line in the plot 4.7.b marks the arrival of P-wave). The cap to cap arrival time of $5.2*10^{-6}$ s is subtracted from the above values to get the corrected arrival time. The height of sample at the time the readings are taken is calculated from the strain at that time and the initial height of sample at the start of the test, which comes out to be 5.2 inches. This height is divided by the corrected arrival time to get the P-wave velocity.

For the S-wave though, the signal obtained from oscilloscope is cross-correlated with the input signal to obtain the plot as shown in Figure 4.8

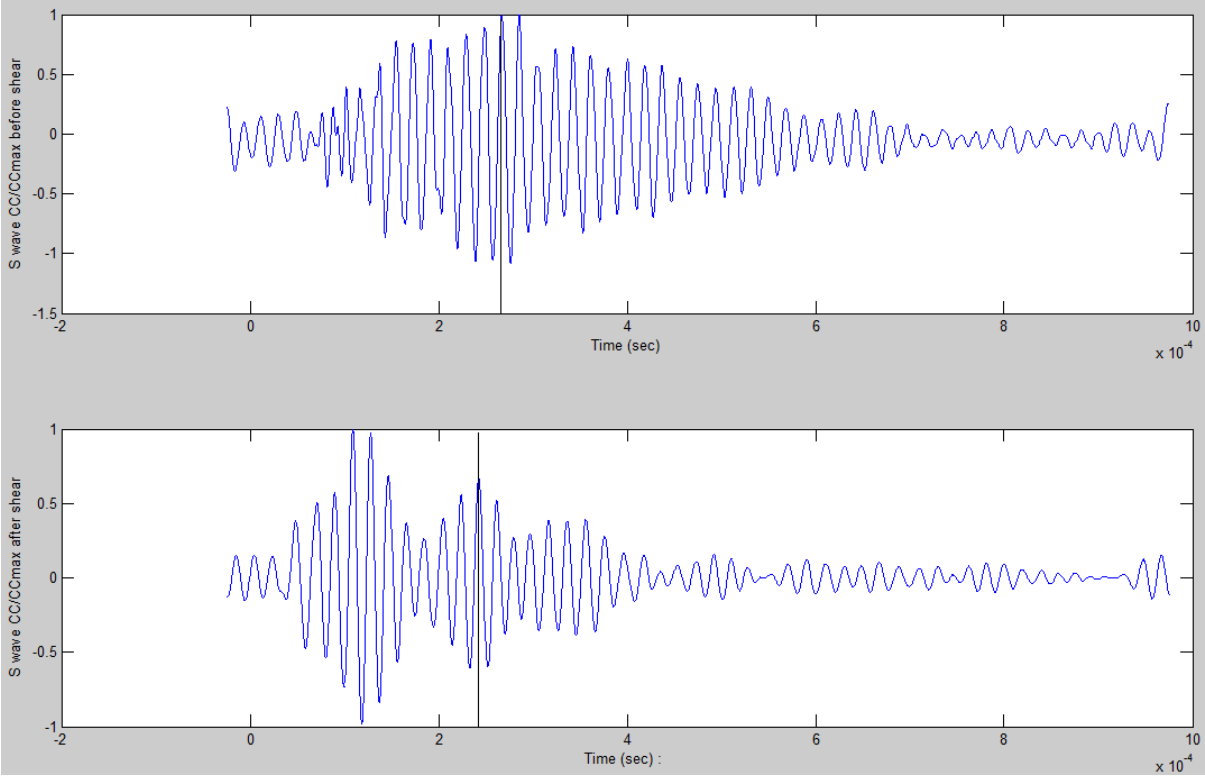

Figure 4.7: Cross-correlated and normalized plots of shear wave profile before and after shear

The arrival time corresponds to either the first or second maxima of the plot 4.8 (marked by vertical black line). Having obtained the arrival time, the shear wave velocity is calculated in the same way as P-wave velocity. Shear modulus, $\mu = \rho V_s^2$. And Bulk modulus, $K = (\rho V_p^2 - 4\,\mu/3)$.

Table 4.3: Table of data reduction

	S		P	
	Before shear	After shear	Before shear	After shear
Time of arrival (s)	0.0002680	0.0002420	0.0000975	0.0000720
Cap to cap arrival (s)	0.0000052	0.0000052	0.0000053	0.0000053
Corrected time of arrival (s)	0.0002628	0.0002368	0.0000922	0.0000667
Height (m)	0.13208	0.10566	0.12090	0.09753
S/P wave velocity (m/s)	251.29	223.10	1311.32	1462.30
Modulus (Gpa)	0.1210	0.0954	3.2958	4.0984

4.10. Results and analysis

The following table summarizes the results obtained from the data obtained from the oscilloscope after being reduced to yield the modulus values for different sand types at different confinement. The measurements are taken twice, one for the before shear signal and the other for the after shear signal to obtain the before shear and after shear velocities respectively.

Table 4.4: Summary of bender element test results

Category	Confinement (kPa)	Shear wave velocity (m/sec)		Shear modulus (Mpa)	
		Before shear	After shear	Before shear	After shear
Round Dense	5	211	211	93.24	93.26
	15	291	247	176.28	127.36
	30	293	274	177.42	153.58
	60	312	280	200.84	161.24
Round Loose	5	207	220	84.14	95.02
	15	267	286	137.24	157.78
	30	266	299	138.93	175.87
	60	276	303	146.35	176.35
Angular Dense	5	208	196	82.96	73.74
	15	251	223	121.03	95.40
	30	271	227	141.44	99.06
	60	285	232	152.69	101.03
Angular Loose	15	218	222	91.56	94.04
	30	224	230	91.39	95.75
	60	249	267	113.51	130.64
Category	Confinement (kPa)	P wave velocity (m/sec)		Bulk modulus (Mpa)	
		Before shear	After shear	Before shear	After shear
Round Dense	5	1822	1668	6.90	5.78
	15	1529	1474	4.86	4.51
	30	1689	1708	5.83	5.96
	60	1610	1569	5.32	5.05
Round Loose	5	1421	1531	3.95	4.59
	15	1626	1691	5.06	5.48
	30	1666	1628	5.45	5.21
	60	1517	1458	4.41	4.07
Angular Dense	15	1311	1462	3.29	4.09
	30	1480	1443	4.18	3.98
	60	1800	1607	6.07	4.83
Angular Loose	15	1394	1325	3.71	3.35
	30	1465	1661	3.89	5.00
	60	1578	1708	4.54	5.32

The shear wave velocity as well as the shear modulus for all categories increases with confining pressure. For dense sands, the value of shear wave velocity after shear is lower than its value before shear. This is due to the fact that dense sands get loose when sheared, and hence is not as compact. Also as expected, for loose sands, the shear wave velocity before shear is lower than the after shear V_s, due to densification of loose sands on shearing. The shear wave velocity ranged from 209 m/sec to 312 m/sec and the shear modulus varied from around 79 Mpa to 176 Mpa. These values are in good agreement with the values found in literature.

An important point to be kept in mind while using the value of travel time for velocity calculation is that we need to subtract the 'zero time' from the value of travel time to get the actual time. As per ASTM D 2845-95, zero time is the delay due to presence of platen between the piezoelectric crystals and the test specimen. The transmission of pulse through the face of platen will take up some time before the pulse reaches the sample. The zero time is determined by placing one cap directly on top of the other and determining the time taken by the pulse to go from the transmitter to the receiver element. In dry sand, the P-wave velocity is depth- and therefore, stress- dependent according to a power law (Emerson & Foray, 2006). The velocity in partially saturated sands is about the same as in dry sand. But at 100% saturation, the velocity largely exceeds that in dry sand. There is a dramatic increase in P-wave velocity as the degree of saturation varies from 99 to 100% (Emerson & Foray, 2006). Figure 4.8 below shows the variation of wave velocity as measured by Bardet & Sayed, (1993), versus effective confining stress for various degrees of saturation, S.

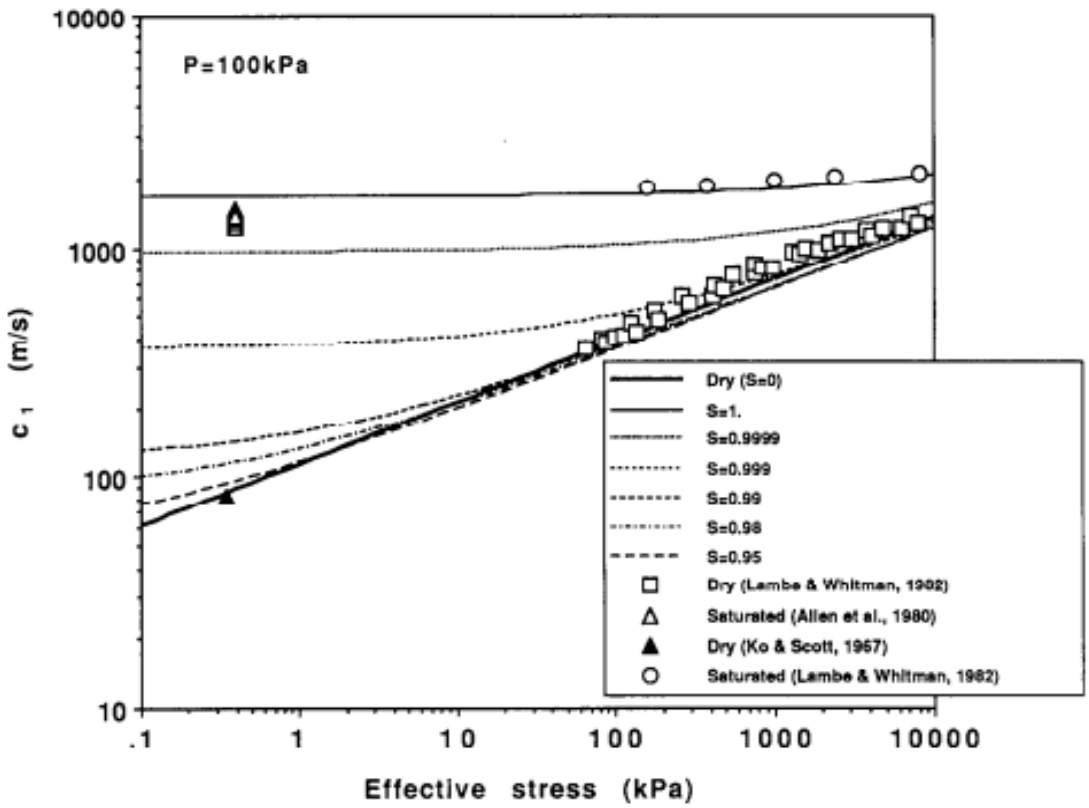

Figure 4.8: Velocity versus effective confining pressure for various degrees of saturation (Bardet & Sayed, 1993)

As can be seen from plot 4.8, a decrease in S from 1 to 0.999 causes a large decrease in wave velocity, especially at effective stresses below 100 kPa. Also, for fully saturated sands, the wave velocity is practically independent of σ'. The above two reasons might explain why, although a clear pattern is observed for shear wave velocities and shear modulus, no such pattern was observable for P-wave velocities. Also, the time taken to achieve 100% saturation in sands is very high, as shown by Lee& Black, 1973, to the point where it is not practical to aim for full saturation (Figure 3.6). Instead we settle for around 99% saturation. The variation in P-wave velocities in between 1400 m/sec and 1800 m/sec was probably due to variation in the degree of saturations of the prepared samples.

CHAPTER V

FINAL RESULTS & CONCLUSIONS

5.1. Normalized plots: Shear stress

Figures 5.1 through 5.4 below illustrate the effect of confining pressure on friction angle of the sand. The deviatoric stress of all the tests have been normalized by dividing by the confining pressure of each test. It is observed that as the confining pressure increases, the plots shift downwards, implying smaller friction angle for higher confining pressure. The 5 kPa plots are significantly higher than the 15, 30 and 60 kPa plots, all three of which lie almost close to one another with the 60 kPa plots at the bottom of all.

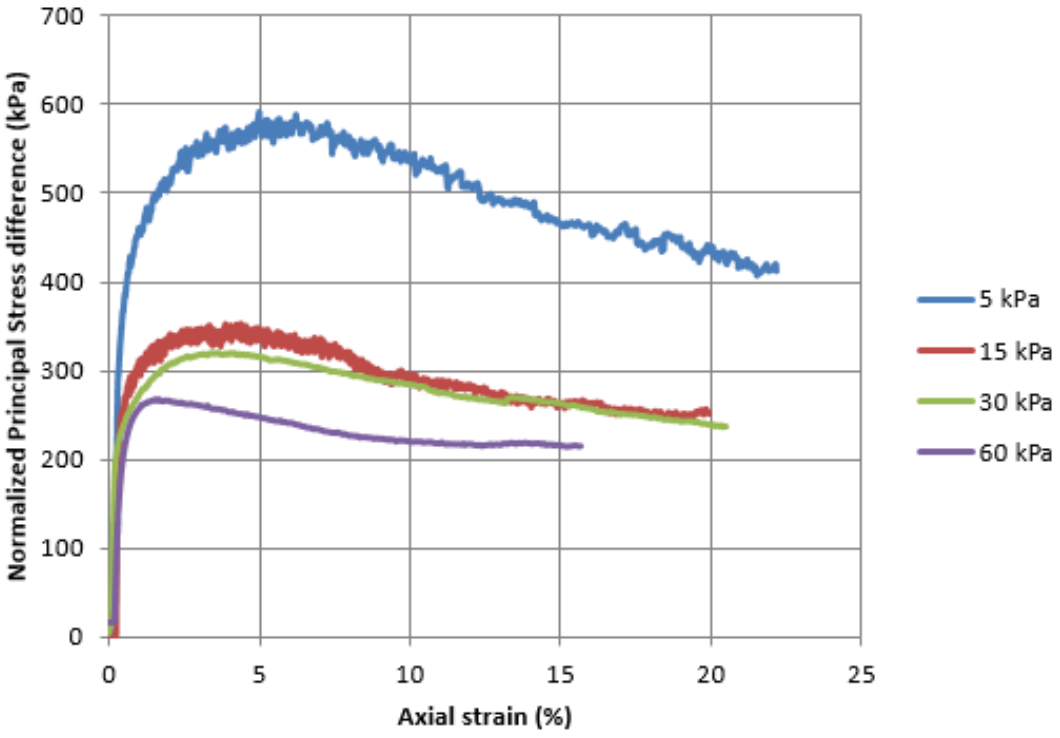

Figure 5.1: Normalized stress-strain plots for round dense sand at various confinement

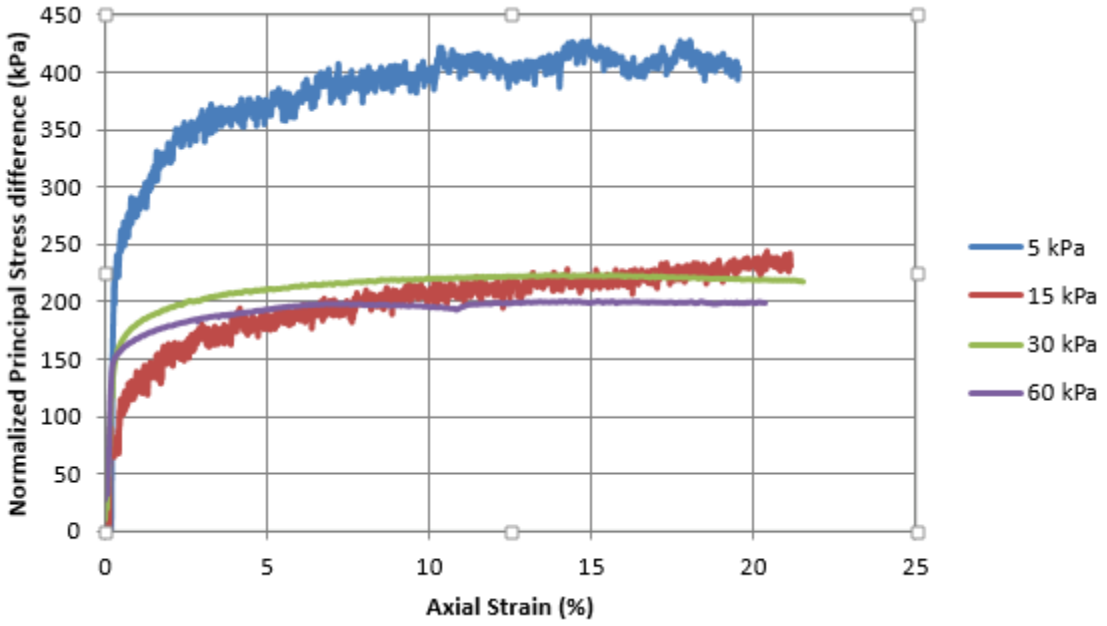

Figure 5.2: Normalized stress-strain plots for round loose sand at various confinement

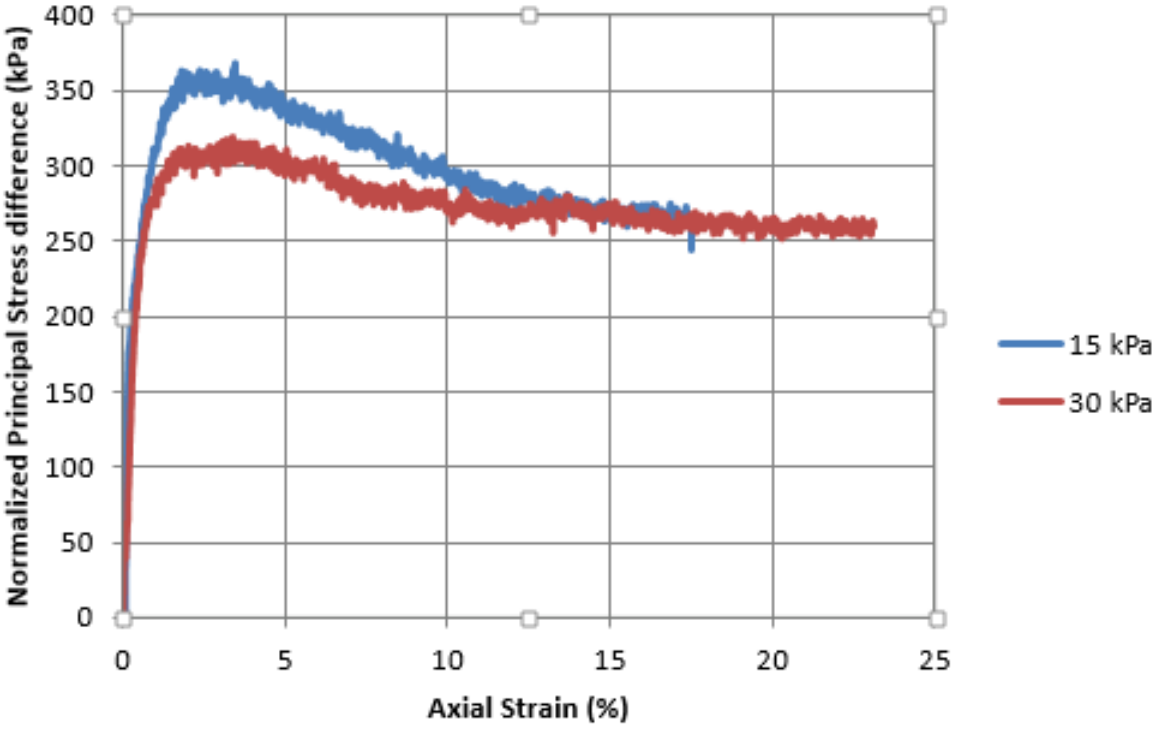

Figure 5.3: Normalized stress-strain plots for angular dense sand at various confinement

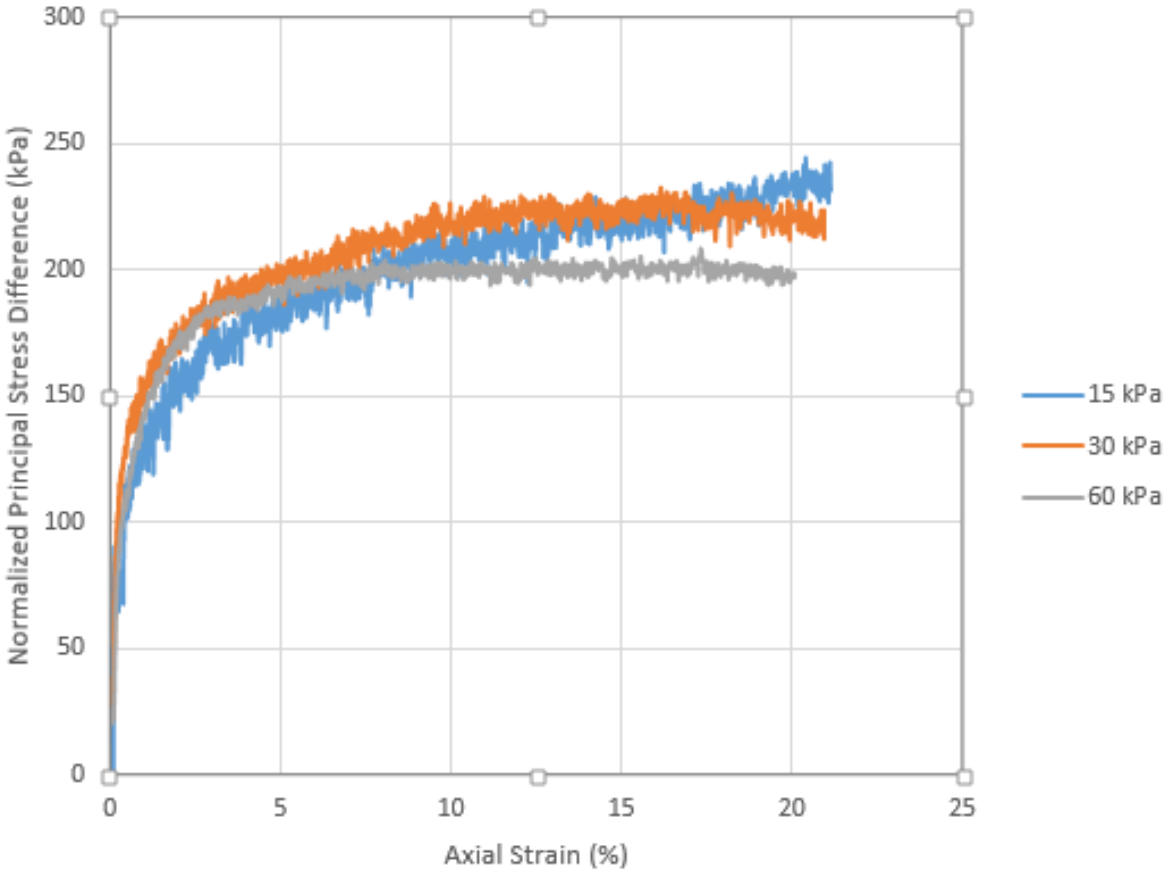

Figure 5.4: Normalized stress-strain plots for angular loose sand at various confinement

5.2. Normalized plots: Shear wave velocity

It was observed that shear wave velocity increased with confining pressure for all categories of sand, in the same way as the shear stress at failure increased with confinement. However, when the velocities were normalized with respect to their confining pressure, a decreasing trend was observed with confinement much like friction angle. So, as per this study, the shear strength and stiffness profiles of sand vary in a similar manner with confining pressure; both show a decreasing trend. Figures 5.5 through 5.8 illustrate the shear wave velocity profiles. Normalization is done by dividing the shear wave velocity for each test by the dimensionless quantity (confining pressure/atmospheric pressure) of that particular test.

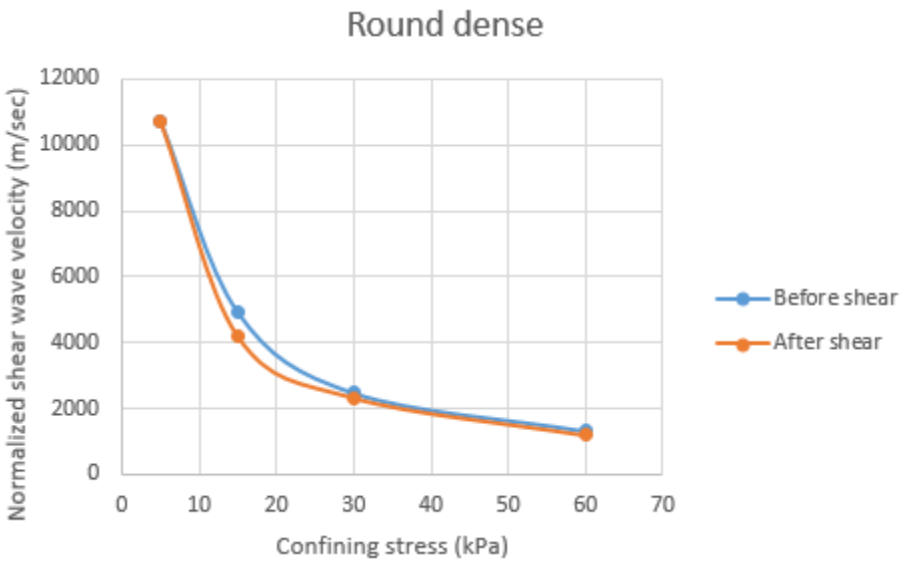

Figure 5.5: Normalized shear wave velocity versus confining stress: Round dense sand

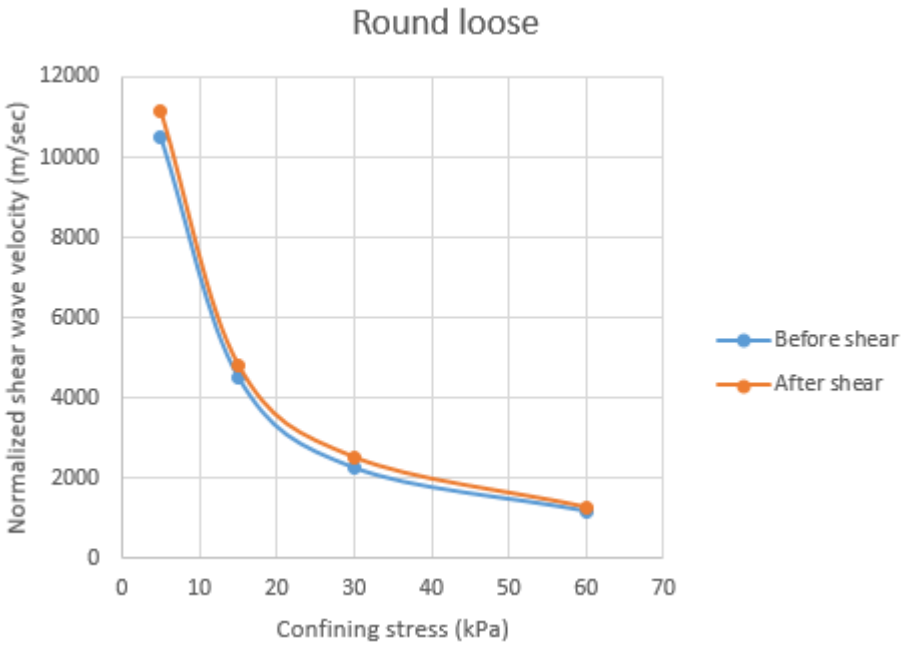

Figure 5.6: Normalized shear wave velocity versus confining stress: Round loose sand

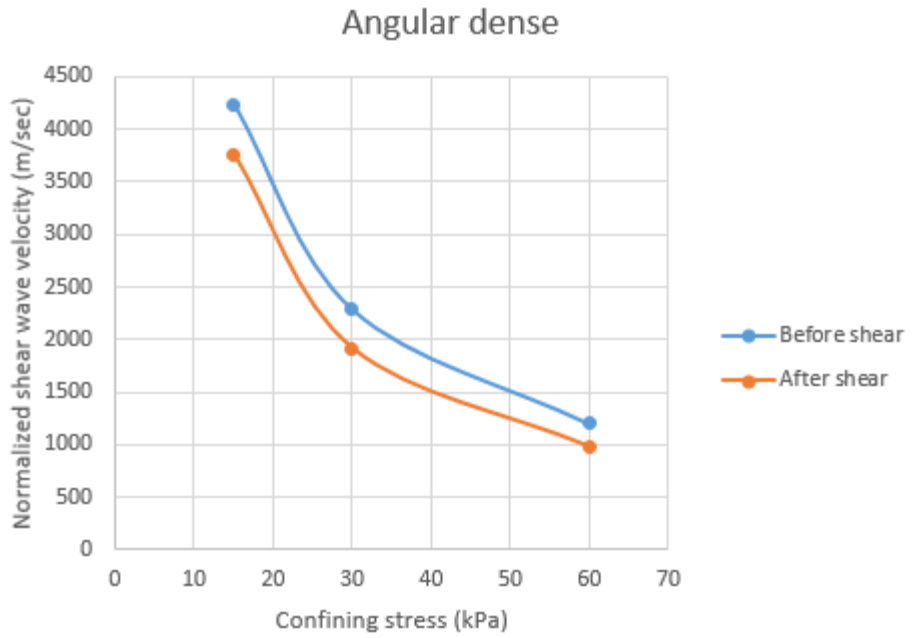

Figure 5.7: Normalized shear wave velocity versus confining stress: Angular dense sand

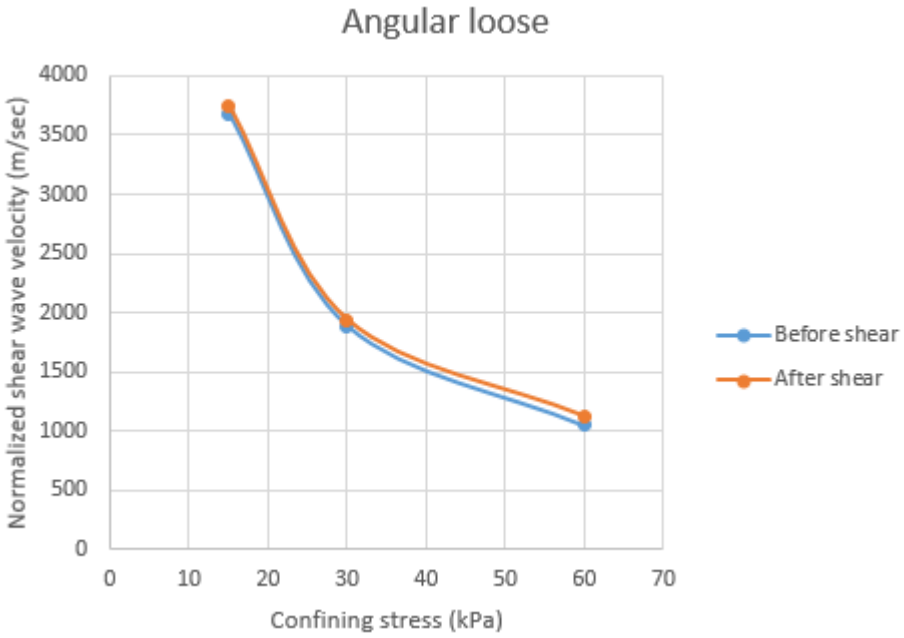

Figure 5.8: Normalized shear wave velocity versus confining stress: Angular loose sand

5.3. Final table of results

The table below summarizes the end results of the tests conducted. Shear strength of soil at failure and the residual value, friction angles, shear wave velocities and the shear moduli are tabulated against the sample void ratio/ relative density, confining stress and the type of soil. Basically, the results of triaxial testing and bender element testing have been combined into a single table. This will give an idea of how the various important soil properties vary with soil conditions.

Table 5.1: Final table of results

a. Round Dense sand

Confining stress (kPa)	Void ratio/Relative density (%)	Shear strength (kPa)		Friction angle (degrees)		Shear wave velocity (m/ sec)		Shear modulus (Mpa)	
		Peak	Residual	Peak	Residual	Before Shear	After shear	Before Shear	After Shear
60	.57, 76.6	63.3	50.7	34.5	31.0	312	280	200.848	161.242
30	.58, 73.3	37.0	28.1	37.3	32.6	293	274	177.427	153.581
15	.53, 90	20.2	15.0	38.9	33.8	291	247	176.284	127.365
5	.53, 90	11.3	8.2	47.5	42.2	211	211	93.244	93.266

Table 5.1 continued

b. Round Loose sand

Confining stress (kPa)	Void ratio/Relative density (%)	Shear strength (kPa)		Friction angle (degrees)		Shear wave velocity (m/sec)		Shear modulus (Mpa)	
		Peak	Residual	Peak	Residual	Before Shear	After shear	Before Shear	After Shear
60	0.8, 0	47.2	47.2	29.8	29.8	276	303	146.350	176.353
30	0.71, 28.1	26.0	26.0	31.3	31.3	266	299	138.938	175.871
15	0.8, 0	13.6	13.6	32.1	32.1	267	286	137.245	157.784
5	0.72, 26.6	7.97	7.97	41.7	41.7	207	220	84.145	95.021

c. Angular Dense sand

Confining stress (kPa)	Void ratio/Relative density (%)	Shear strength (kPa)		Friction angle (degrees)		Shear wave velocity (m/sec)		Shear modulus (Mpa)	
		Peak	Residual	Peak	Residual	Before Shear	After shear	Before Shear	After Shear

Table 5.1 c. continued

60	0.89, 70	76.3	55.4	37.8	32.4	285	232	152.693	101.03
30	0.8, 100	38.1	31.3	38.0	34.5	271	227	141.442	99.063
15	0.8, 100	20.8	16	39.4	34.9	251	223	121.034	95.406

d.Angular Loose sand

Confining stress (kPa)	Void ratio/Relative density (%)	Shear strength (kPa)		Friction angle (degrees)		Shear wave velocity (m/sec)		Shear modulus (Mpa)	
		Peak	Residual	Peak	Residual	Before Shear	After shear	Before Shear	After Shear
60	1.00, 33.3	49.33	49.33	30.4	30.4	249	267	113.512	130.648
30	1.03, 23.3	27.5	27.5	32.3	32.3	224	230	91.398	95.752
15	1.02, 26.6	14.5	14.5	33.17	33.17	218	222	91.561	94.041

5.4. Inferences & observations

Sands derive their strength from friction in between the grains and higher the contact stresses between grains, higher is the frictional resistance mobilized. Higher contact stresses are achieved at higher confinement. This explains why sands can take more shear stress at higher confining pressure. This is consistent with Mohr- Coulomb failure criterion which predicts a direct linear relationship between shear strength and normal stress. Relative density of the sample also plays an important role in determining the failure shear strength. When a dense sand was sheared, the grains tended to tangle which mobilized more friction and therefore higher peak strength than loose sand. A clearly marked

failure plane was observed on shearing a dense sand. This is because a dense sand loosens when sheared so the initial failure plane who was the weakest gets weaker and remains the weakest during the entire shearing process. However, when a loose sand was sheared, the sand in the immediate neighbourhood of the failure plane got denser and hence stronger so the current failure plane was replaced by a different failure plane which is weaker. Hence after failure there was no visible distinct failure plane for initially loose sand samples.

Friction angle decreased with increasing confining pressure. This implies that although shear strength increased with increasing confinement, the increase was not in the same proportion as the increase in normal stress. The result is that the peak strength envelope is curved in the Mohr-Coulomb plot. The study described in this paper resulted in angular sand having friction angles which is about 1^0 higher than the rounded sand for the same confining stress. It is worth noting that the loosest state of angular sand coincided with the densest state of rounded sand, as far as void ratio is concerned and thus, a fair comparison would be to compare loose round sand with dense angular sand in which case the difference in friction angle is of the order of 3 degrees.

The soil behaved linearly at very low values of strain ($\sim 10^{-3}$%) after which the behavior was non-linear. Peak shear strength developed further at around 1-4 % axial strain for dense sand. 'Critical state' which is characterized by shearing progressing with no volume change, was not observed for most samples and the samples were sheared to 20% strain thus suggesting that the samples needed to be sheared further (beyond 25%) to attain critical state. The loose sand contracted and the dense sand dilated (after initial contraction) as they approached critical state. The maxima of the rate of dilation seemed to coincide with the peak in shear strength for dense sands beyond which the shear stress dropped. Irrespective of the initial relative density of the sample for a given confining pressure, the final near-critical state shear strength was the same.

The shear wave velocity and the shear modulus increased with confining pressure. However, on normalizing the wave velocities with respect to their confining pressure, a decreasing trend was observed with confining pressure. For dense sands, the value of shear wave velocity after shear is lower than its value before shear. This is due to the fact that dense sands get loose when sheared, and hence is not as compact. Also as expected, for loose sands, the shear wave velocity before shear is lower than the after shear V_s, due to densification of loose sands on shearing. The shear wave velocity ranged from 209 m/sec to 312 m/sec and the shear modulus varied from around 79 Mpa to 176 Mpa. The P-wave velocity didn't follow any pattern with confinement or shearing. The reason can be attributed to P-wave velocity being extremely sensitive to degree of saturation and practically independent of confining pressure at confinements below 100 kPa.

5.5. Scope of future work

In this study, the effects of grain shape/size, density and confining pressure were taken into account. However, there are other factors like fines content, surface roughness etc. that affect sand behavior which need to be taken into account. Also, more data is required to model soil behavior at pressures higher than 60 kPa to propose quantitative equations. So more tests need to be run at higher pressures and on different materials. These further tests will also help either corroborate or contrast the findings of this study and thus give more confidence on the results or make us rethink about the results.

Only a single pair of bender element and ultrasonic transducer was used and one combination of voltage-amplitude-frequency of signal was used. It would be worthwhile to change some of the characteristics of the elements and/or the waveform characteristics to see if any improvement in the signal quality is possible that might render travel time determination more error free.

It has been suggested that friction angles obtained from plane strain tests and triaxial tests are different and the difference can be as high as 5 degrees. If that's the case then it makes sense to try and correlate the friction angles obtained from both setups and see which values correlate better.

Finally, since there exists correlations between friction angle and angle of dilation, and this study seeks to obtain correlations between friction angle and shear modulus, a similar attempt could be made to obtain correlations between angle of dilation and shear modulus.

REFERENCES

ASTM D4253-00(2006): Standard Test Methods for Maximum Index Density and Unit Weight of Soils using a Vibratory Table

ASTM D4254-00(2006): Standard Test Methods for Minimum Index Density and Unit Weight of Soils and Calculation of Relative density

Bardet, J.P. & Sayed, H. (1993): Velocity and attenuation of compressional waves in nearly saturated soils, Soil dynamics and earthquake engineering, 12, 391-401, DOI: 10.1016/0267-7261(93)90002-9

Black, David K. & Lee, Kenneth L. (1973): Saturating laboratory samples by back pressure, Journal of the soil mechanics and foundations division, 99(1), 75-93

Chakraborty, T., and Salgado, R. (2010): Dilatancy and shear strength of sand at low confining pressures, Journal of geotechnical and geoenvironmental engineering, 136(3), 527-532

Emerson, M and Foray, P. (2006): Laboratory P-wave measurements in dry and saturated sand, Geotechnica, 1(3), 167-177

Houlsby, G.T. (1991): How the dilatancy of soils affect their behavior, Tenth European Conference on Soil Mechanics and Foundation Engineering, Report Number OUEL 1888/91

Kara, Esma M., Meghachou, M. and Aboubekr, N. (2013): Contribution of particle size ranges to sand friction, Engineering, technology and applied science research, 3(4), 497-501

Lagioia, R., Sanzeni, A. and Colleselli, F (2005): Air, water and vacuum pluviation of sand specimens for the triaxial apparatus, Soils and foundations, 46(1), 61-67

Leong, E.C., Yeo, S.H., and Rahardjo, H. (2005): Measuring shear wave velocity using bender elements, Geotechnical testing journal, 28(5), DOI: 10.1520/GTJ12196

Lunne, T., Lacasse, S., Aas, G. and Madshus, C. (1985): Design parameters for offshore sands: Use of in-situ tests, Advances in underwater technology and offshore engineering, 3, 269-292

Novoa- Martinez, B. (2003): Strength properties of granular materials, Thesis submitted to the graduate faculty of Louisiana State University, Baton Rouge, LA

Rad, N.S., and Tumay, M.T. (1987): Factors affecting sand specimen preparation by raining, Geotechnical Testing Journal, 10(1), 31-37

Randolh, Mark F., Gaudin, C., Gourvenec, Susan M., White, David J., Boylan, N., Cassidy, Mark J. (2010): Recent advances in offshore geotechnics for deep water oil and gas developments, Ocean Engineering 38(7), 818-834

Sadrekarimi, A., and Olson, S.M. (2012): Effect of sample preparation method on critical state behavior of sands, Geotechnical testing journal, 35(4), DOI: 10.1520/GTJ104317

Salgado, R., Bandini, P., and Karim, A. (2000): Shear strength and stiffness of silty sand, Journal of Geotechnical and Geoenvironmental Engineering, 126(5), 451-462

Schanz, T. and Vermeer, P.A. (1995): Angles of friction and dilatancy of sand, Geotechnique, 46(1), 145-151

Schmalz, D., LaRochelle, E., and Sheahan, T. (2007): Development and proof-testing of a PC- based bender element system for shear wave measurements in soft soil, Proceedings, 4th intl. symp. on deformation characteristics of geomaterials, Atlanta, 725-732

Ud-din, S., Marri, A., and Wanatowski, D. (2011): Effect of high confining pressure on fibre reinforced sand, Geotechnical engineering journal of the SEAGS & AGSSEA, 42(4), 69-76

Viggiani, G., and Atkinson, J.H. (1995): Interpretation of bender element tests, Geotechnique, 45(1), 149-154

APPENDIX A

TRIAXIAL TEST PLOTS

A1. Round sand

5kPa dense

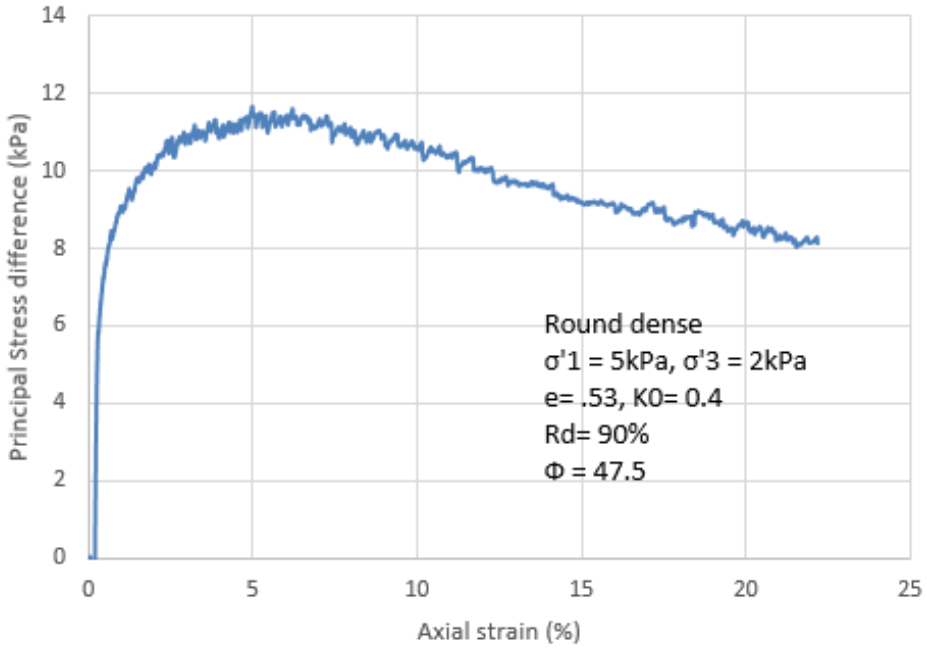

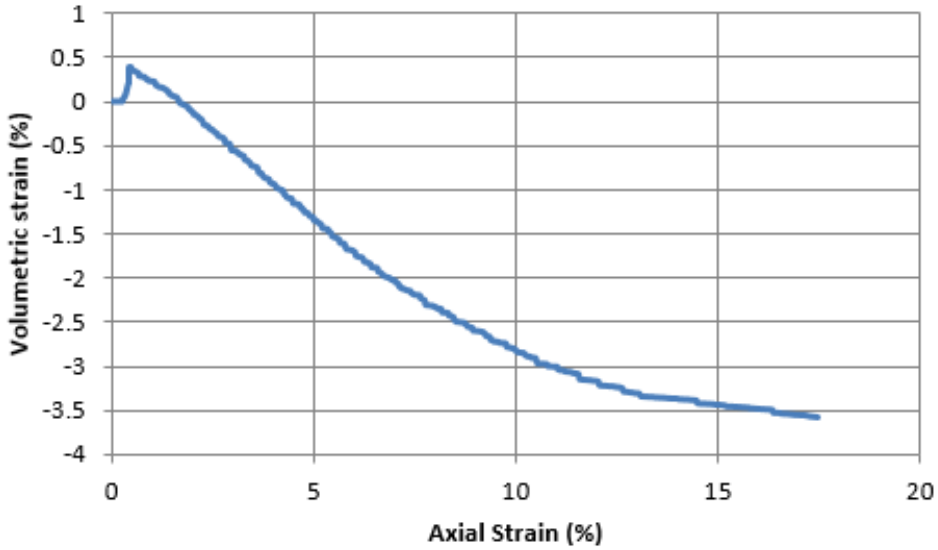

Figure 1: 5kpa dense round sand plots

5kPa loose

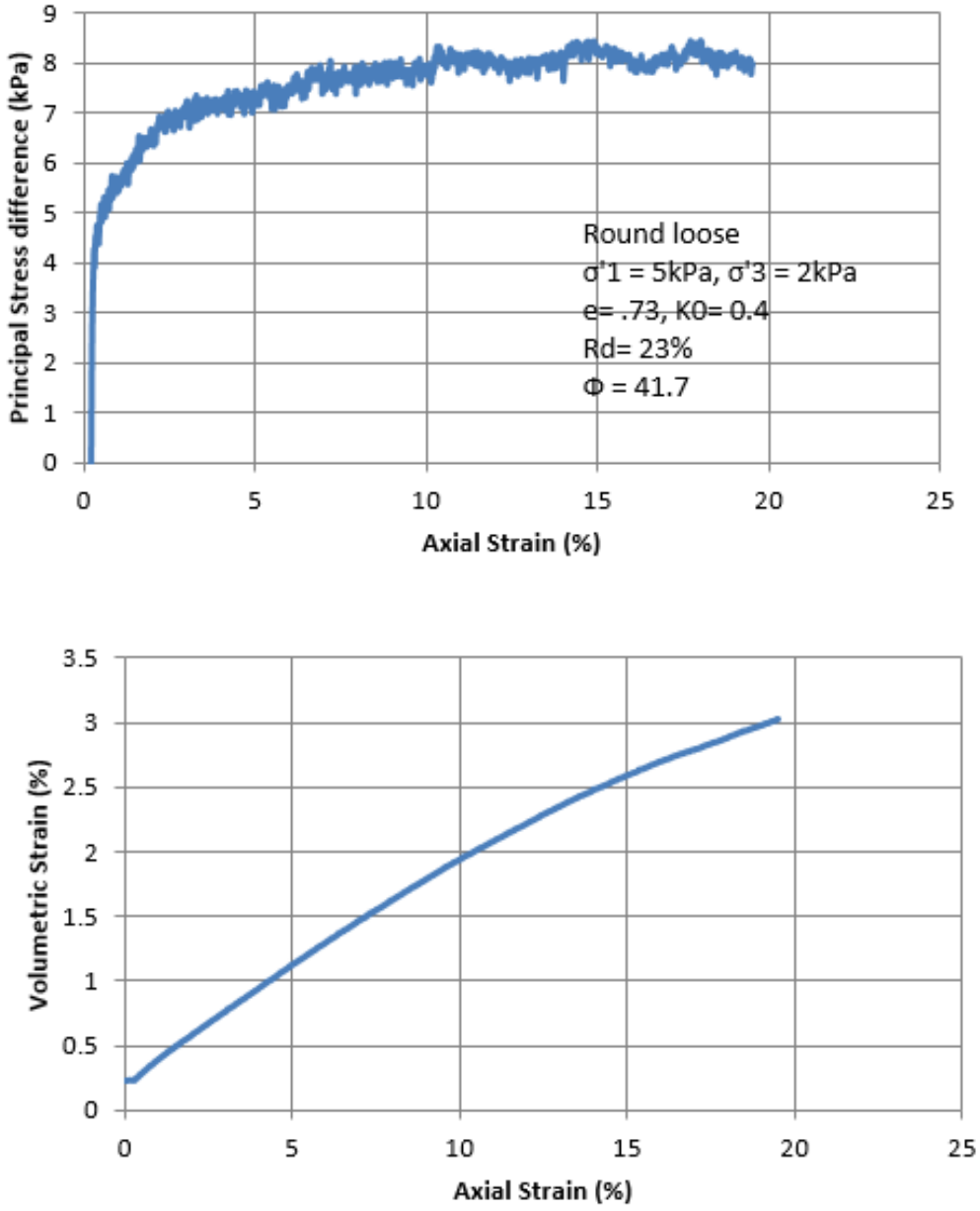

Figure 2: 5kPa loose round sand plots

15kPa dense

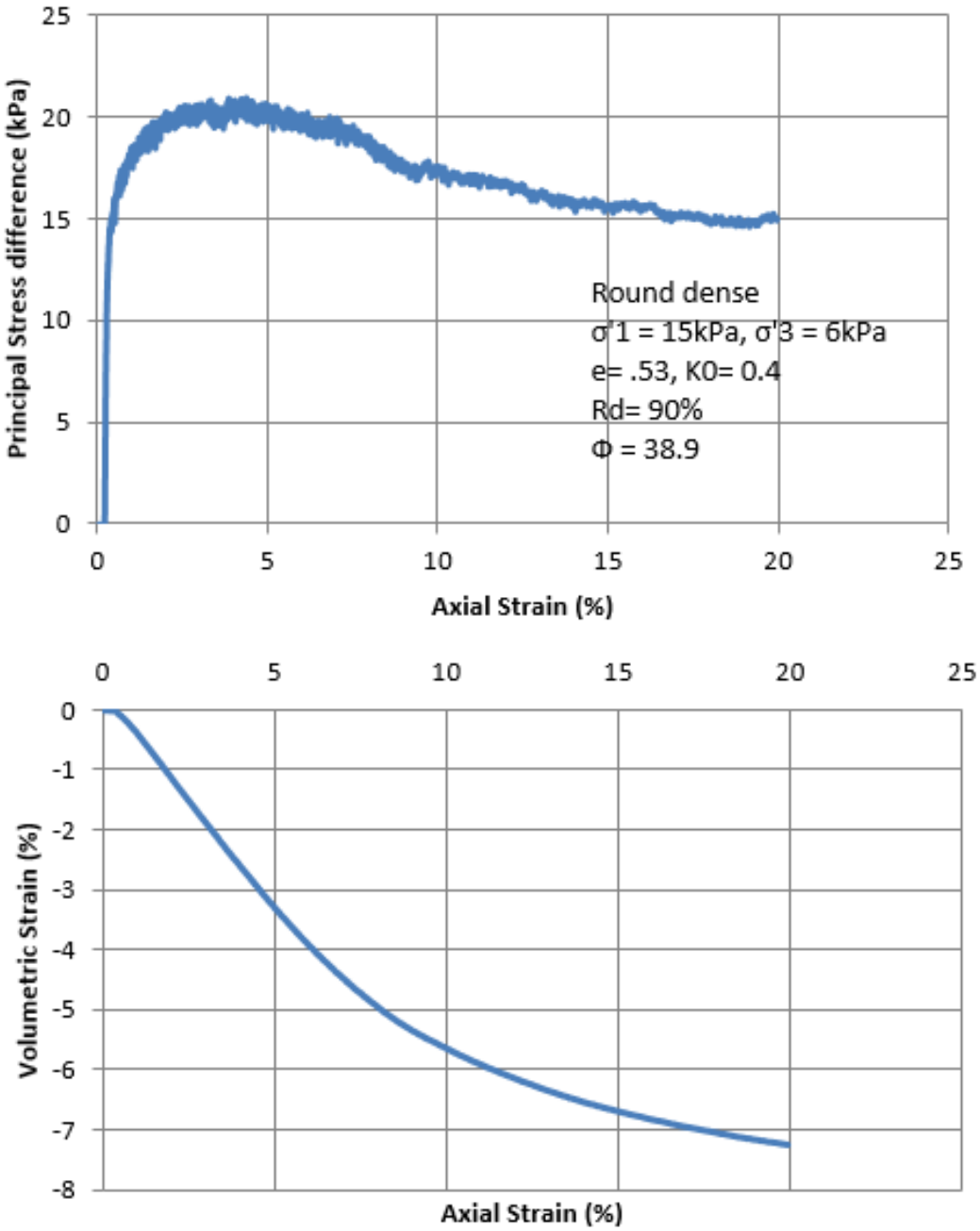

Figure 3: 15kPa dense round plots

15kPa loose

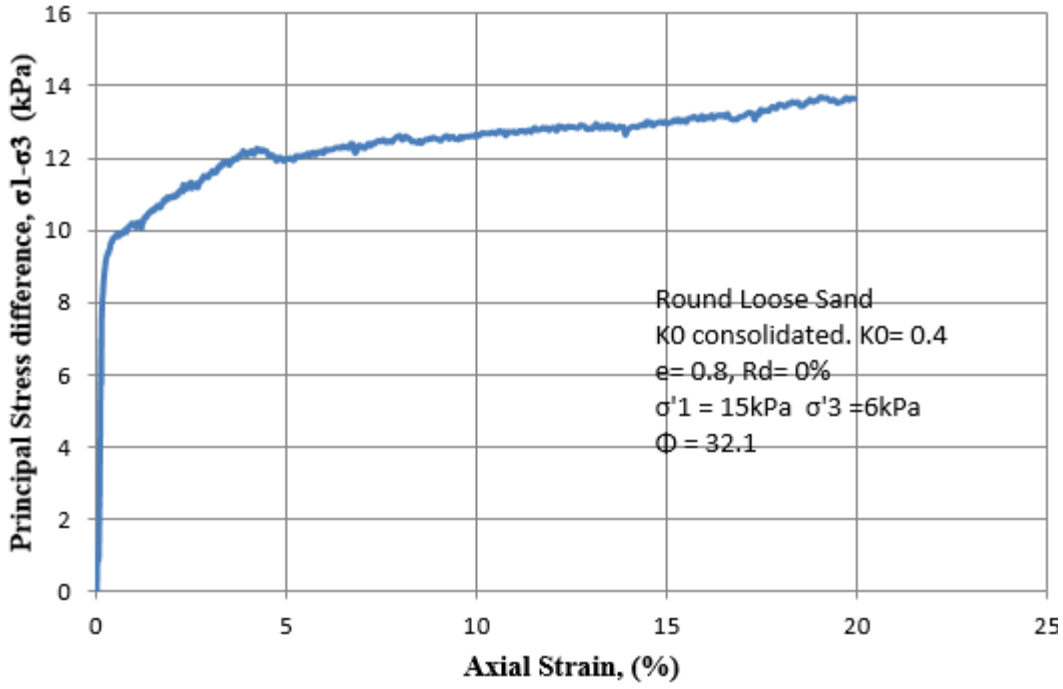

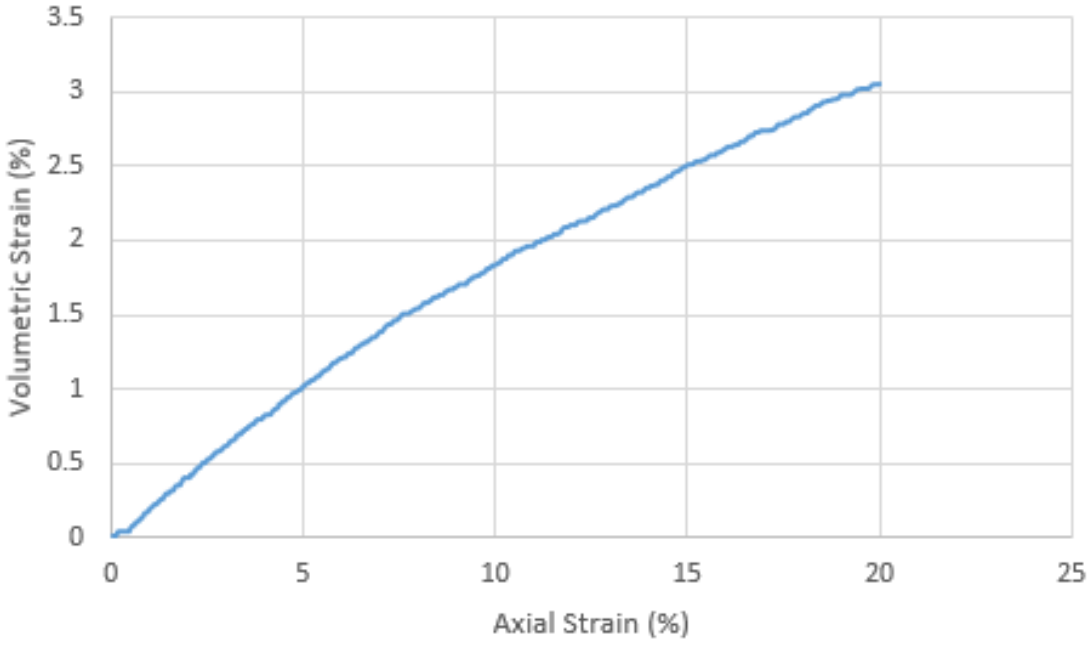

Figure 4: 15kPa loose round plots

30kPa dense

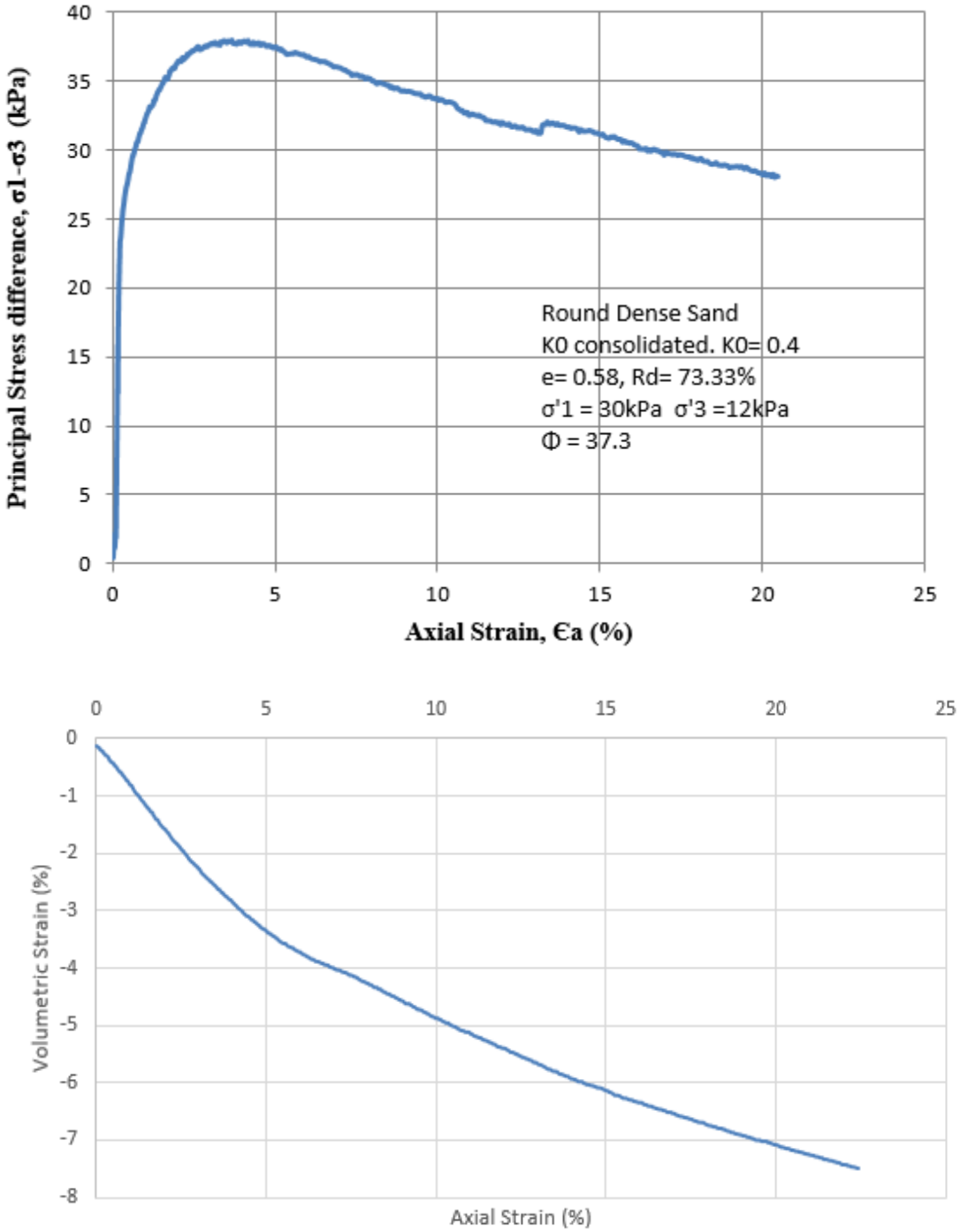

Figure 5: 30kPa round dense plots

30kPa loose

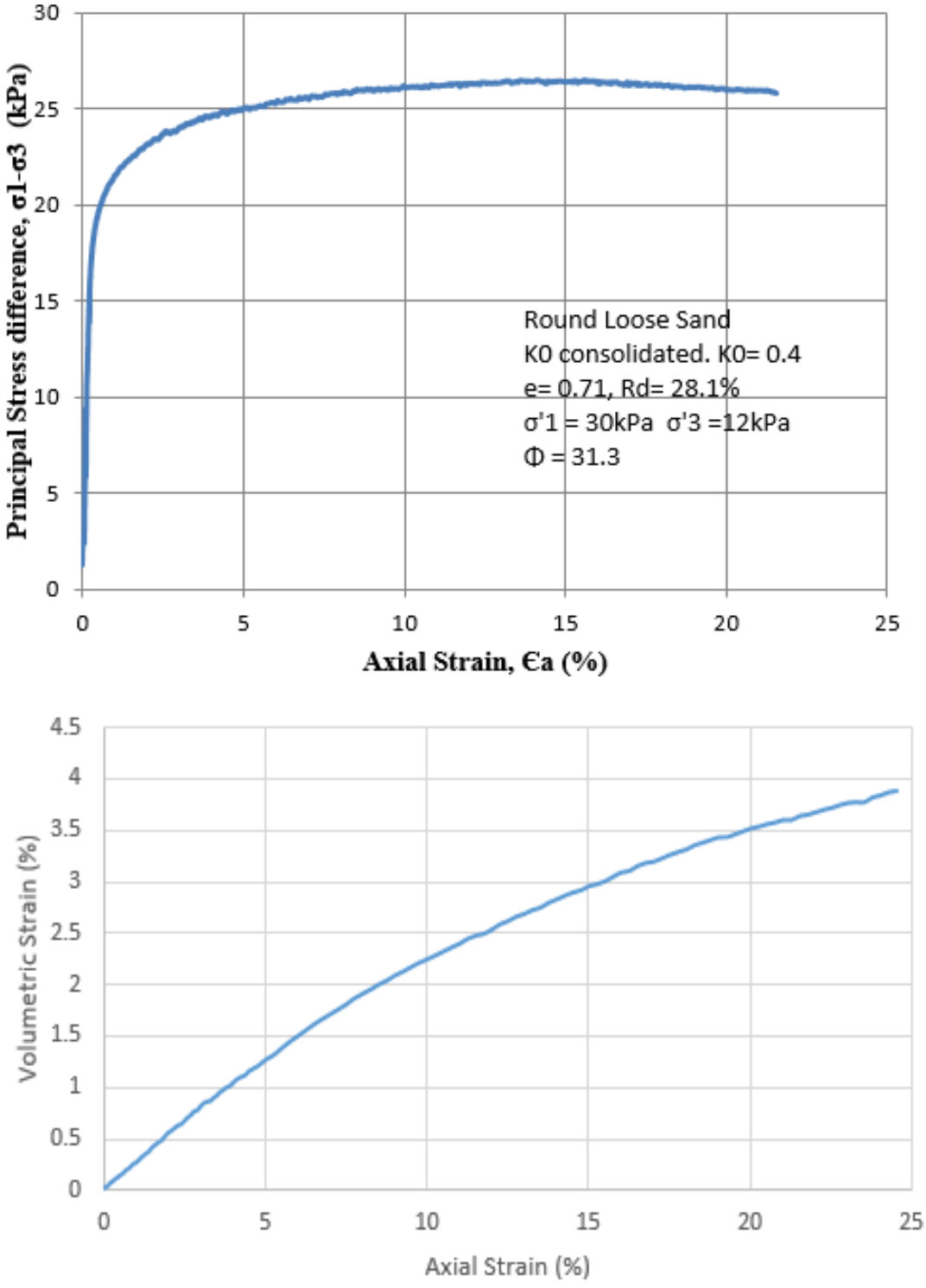

Figure 6: 30kPa round loose plots

60kPa dense

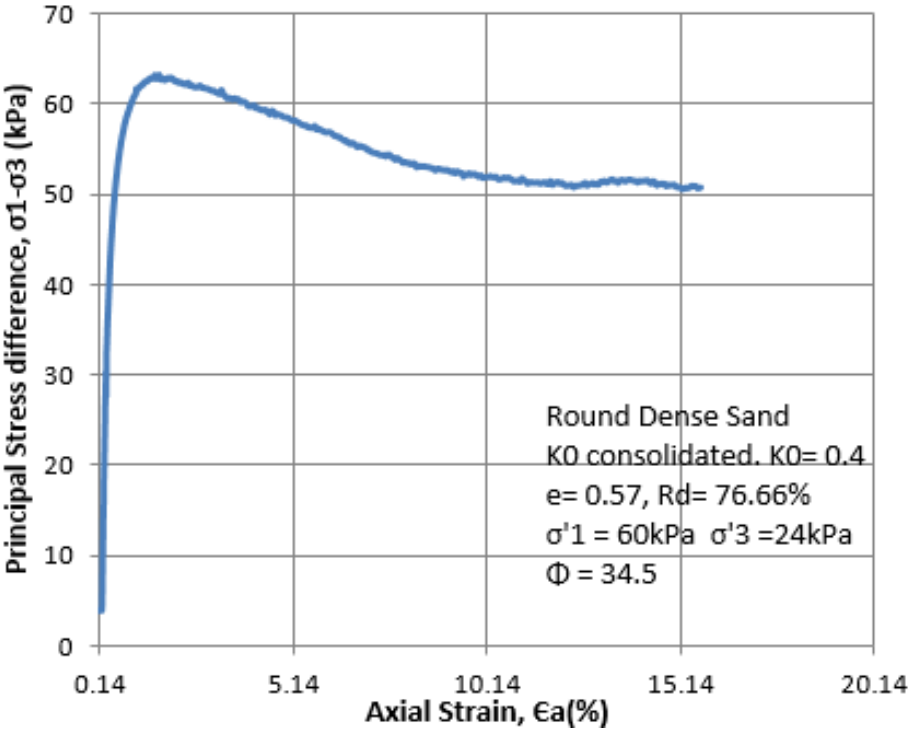

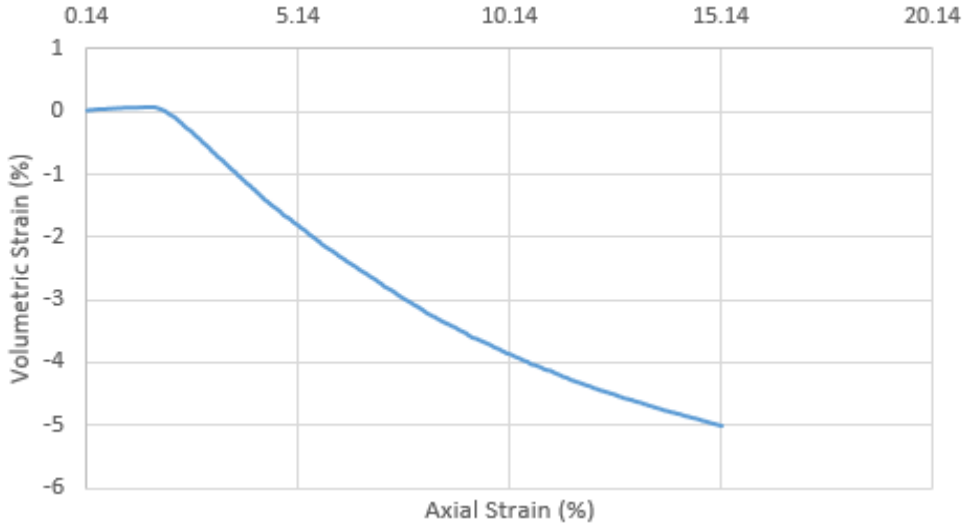

Figure 7: 60kPa round dense plots

60kPa loose

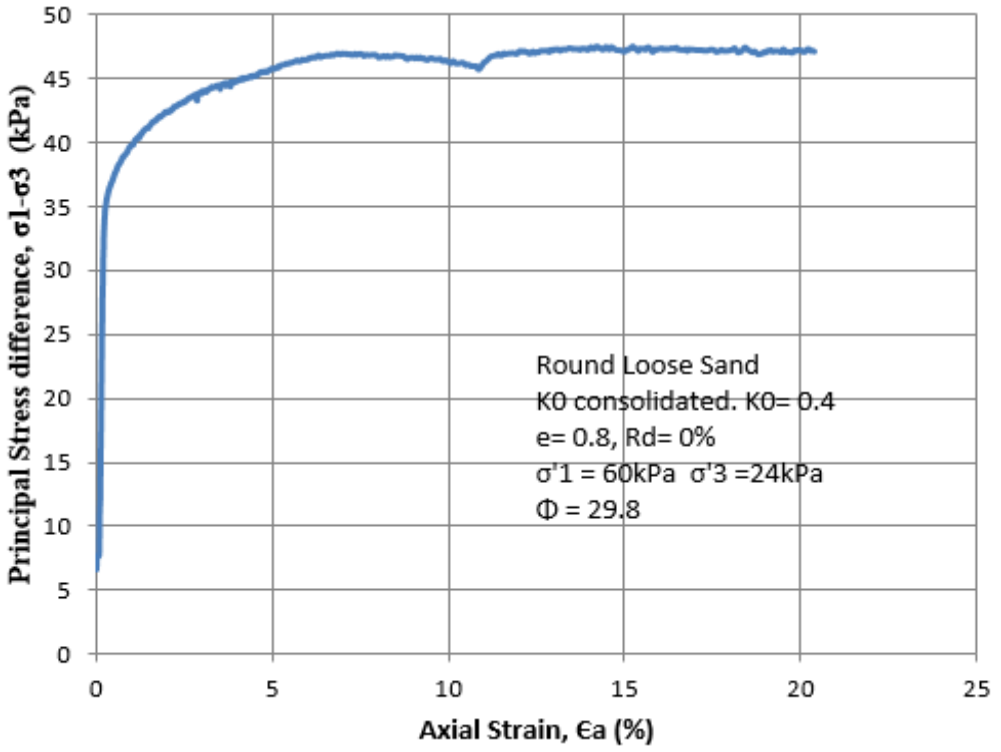

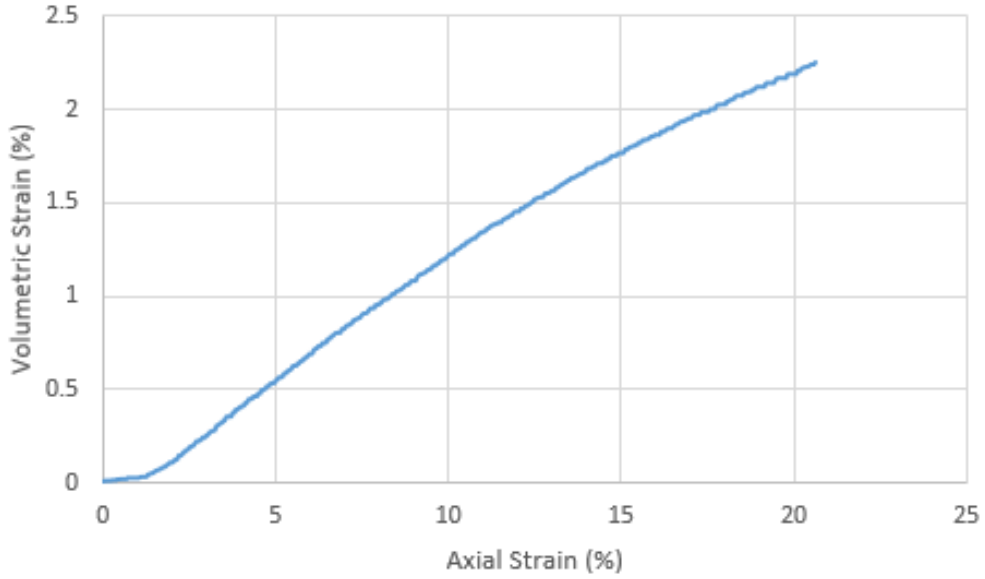

Figure 8: 60kPa round loose plots

3.7.2. Angular sand

15kPa dense

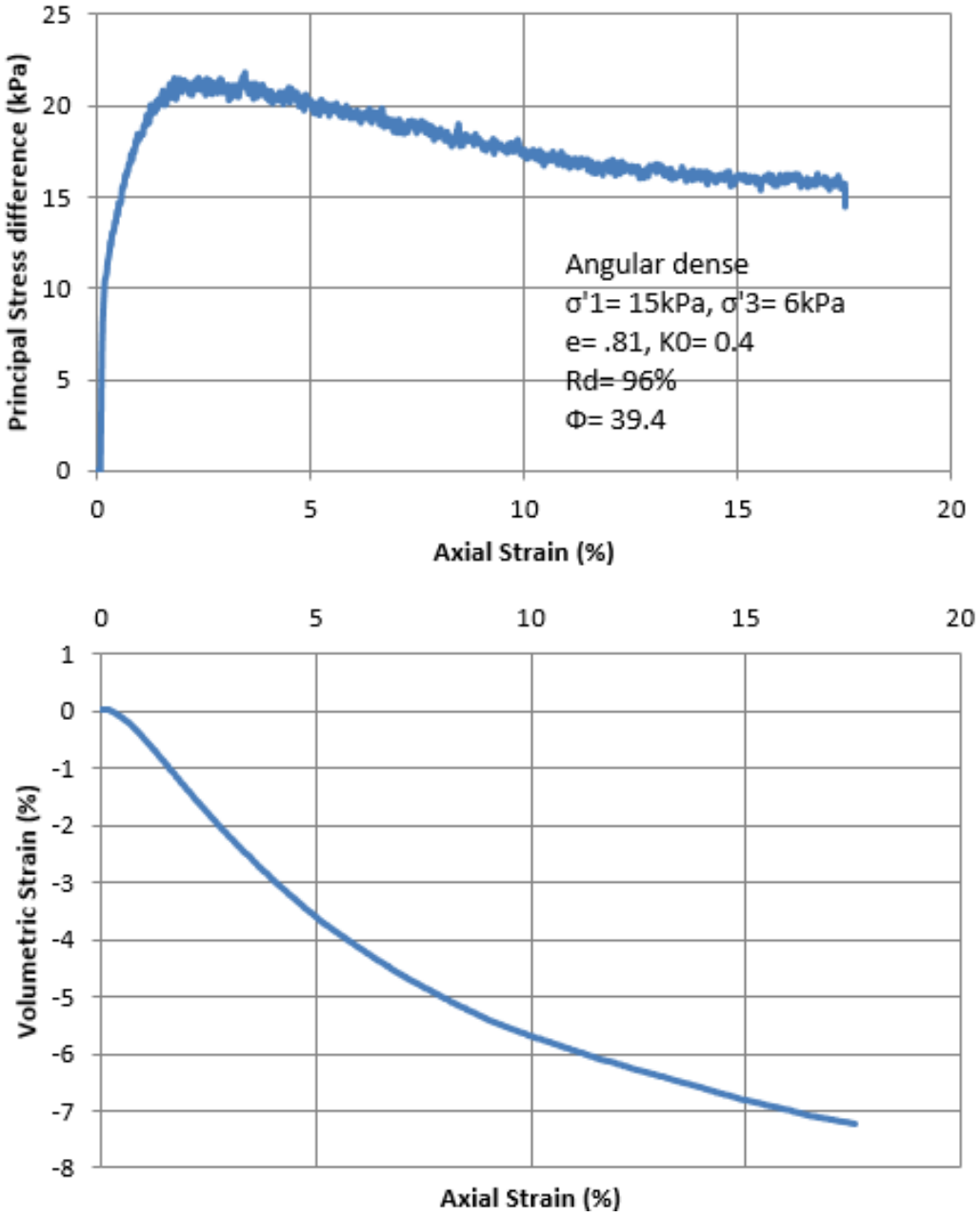

Figure 9: 15kPa dense angular plots

15kPa loose

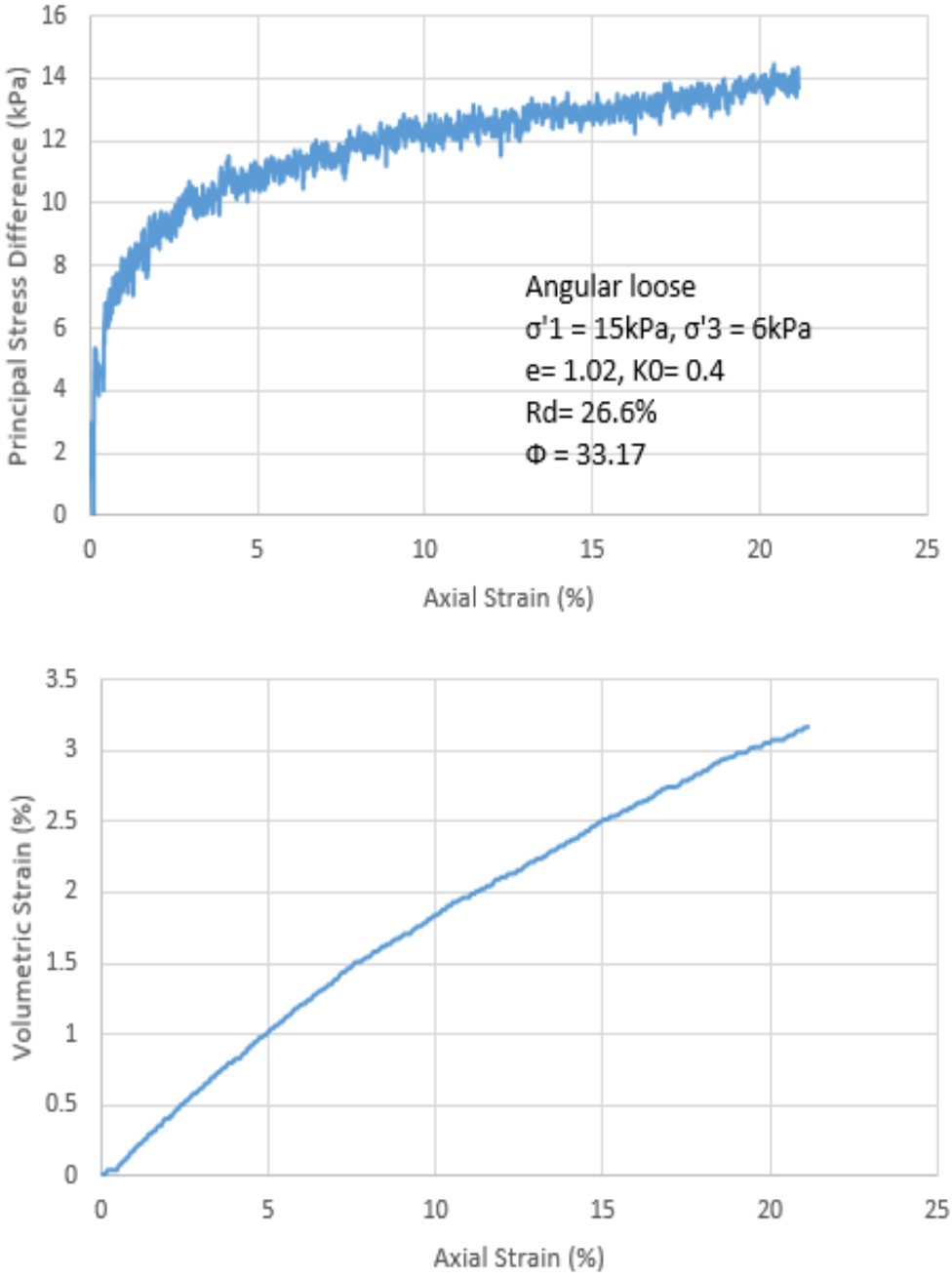

Figure 10: 15kPa loose angular plots

30kPa dense

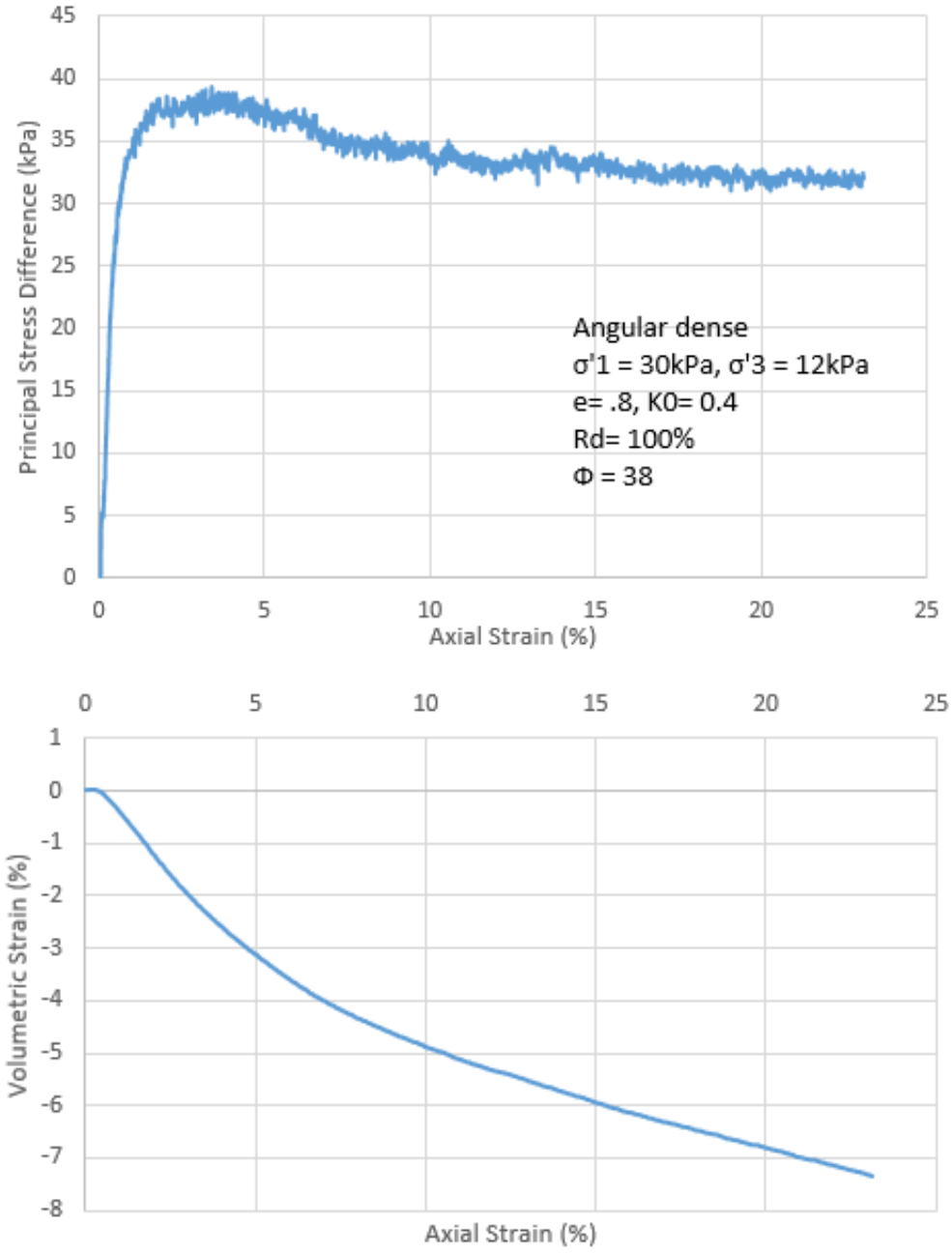

Figure 11: 30kPa dense angular plots

30kPa loose

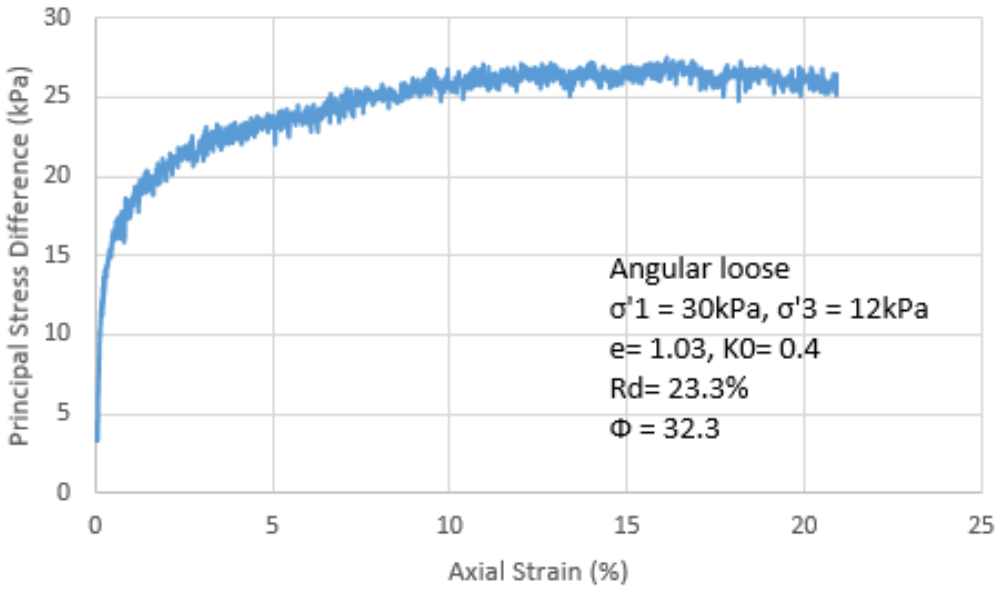

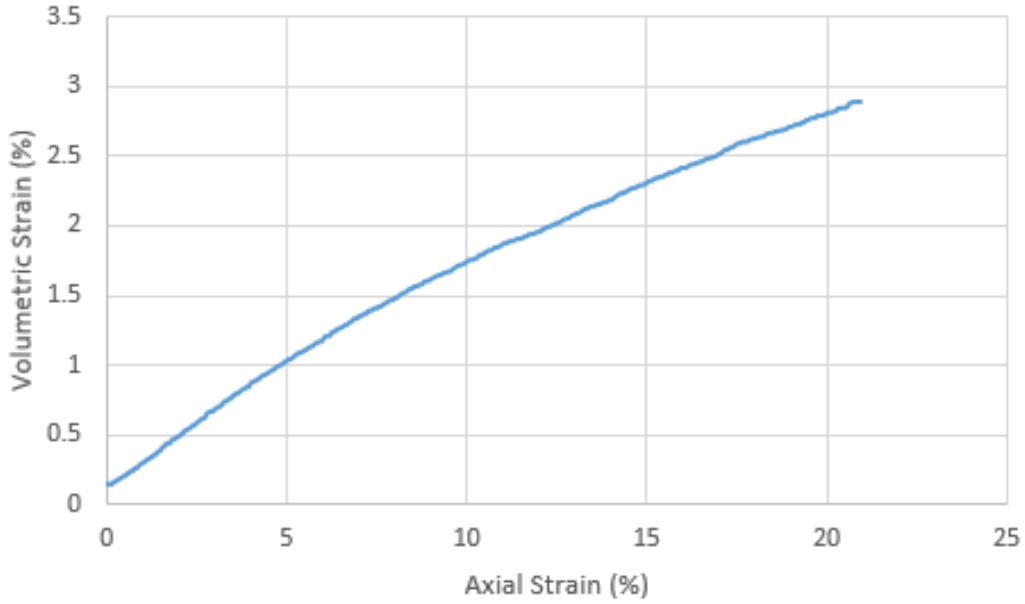

Figure 12: 30kPa loose angular plots

60kPa loose

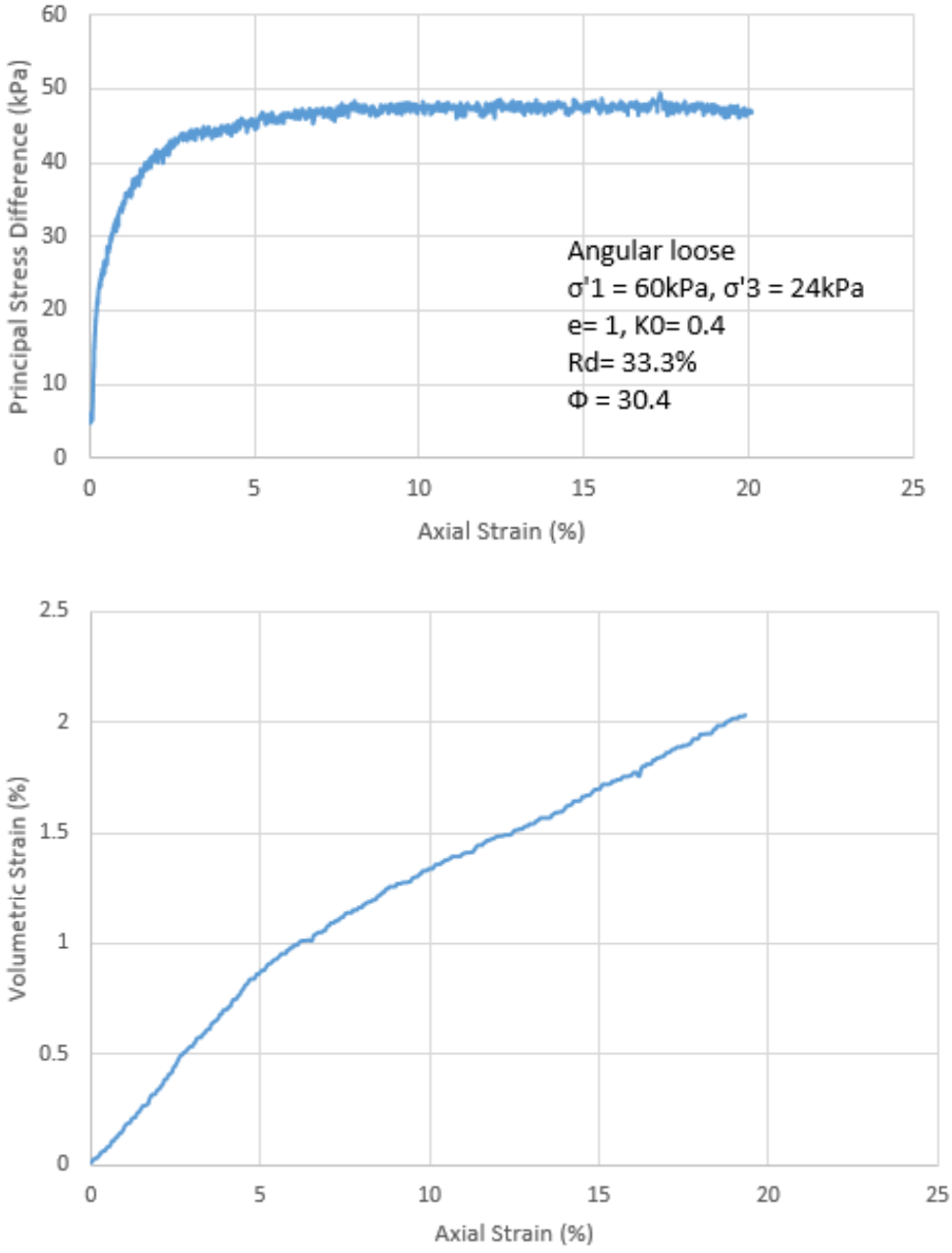

Figure 13: 60kPa loose angular plots

APPENDIX B

MATLAB CODE FOR DATA REDUCTION

The following MATLAB code was implemented to reduce the raw oscilloscope data to yield plots of input and output signal with time from which the travel time was recognized and the data was crunched to get the velocity and modulus values for each test.

```
clear all

%% Import data
ddata = importdata ('ddata.txt');
n = length(ddata);
for i=1:n
   % Time
   t(i) = ddata(i,1);
   in(i) = ddata(i,2);

   % S data
   s_before(i) = ddata(i,4);
   s_after(i) = ddata(i,5);
   % zero the central line of s data
   s_before(i) = s_before(i) + 0.06;
   s_after(i) = s_after(i) + 0.2;

   % P data
   p_before(i) = ddata(i,7);
   p_after(i) = ddata(i,8);
end

%% Cross correlation

% taking fast fourier transform of input and output signals
in_fft = fft(in);
s_before_fft = fft(s_before);
s_after_fft = fft(s_after);

% taking complex conjugate of input function
in_fft_CC = conj(in_fft);

% Cross power spectrum G:
G_in_sbefore = in_fft_CC.*s_before_fft;
G_in_safter = in_fft_CC.*s_after_fft;

% Cross correlation
CC_in_sbefore = ifft(G_in_sbefore);
CC_in_safter = ifft(G_in_safter);

% normalise CC
CC_before = CC_in_sbefore/max(CC_in_sbefore);
```

```
CC_after = CC_in_safter/max(CC_in_safter);

%% Phase velocity

mat = in_fft./s_before_fft;
numerator = imag(mat);
denominator = real(mat);
phase = atan(numerator/denominator);
v = 0.127*50000/phase;



%% Plot

figure(1)
plot(t(:),in(:))
xlabel('Time (sec)')
ylabel('Input signal amplitude (V)')

figure(2)
subplot(2,1,1)
plot(t(:),p_before(:));
xlabel('Time (sec) : ')
ylabel('P wave amplitude before shear (V)')

subplot(2,1,2)
plot(t(:),p_after(:));
xlabel('Time (sec)')
ylabel('P wave amplitude after shear (V)')

figure(3)
subplot(2,1,1)
plot(t(:),s_before(:));
xlabel('Time (sec)')
ylabel('S wave amplitude before shear (V)')

subplot(2,1,2)
plot(t(:),s_after(:));
xlabel('Time (sec)')
ylabel('S wave amplitude after shear (V)')

figure(4)
subplot(2,1,1)
plot(t(:),CC_before(:));
xlabel('Time (sec)')
ylabel('S wave CC/CCmax before shear')

subplot(2,1,2)
plot(t(:),CC_after(:));
xlabel('Time (sec) : ')
ylabel('S wave CC/CCmax after shear')
```

APPENDIX C

BENDER ELEMENT TESTING PROCEDURE AND EQUIPMENT DETAILS

Waveform Generator

Settings recommended below are saved as "STATE_1". So on turning the waveform generator on, hit the "store/recall" button and then select "recall state". Then select "STATE_1" and hit "recall state". The settings that are saved are:

- SINE : Freq =50kHz, Ampl = 10Vpp, Offset =none
- BURST: N cycles selected, # cycles = 1, start phase = 0 deg, and manual trigger

Burst mode with manual trigger is used to give a single signal. Make sure the output button is lit, otherwise no signal is being sent.

Amplifier

Currently we are amplifying the input. The only dial that needs to be adjusted for amplification is the 'gain'. The bender elements will require less amplification than the ultrasonic transducers.

Oscilloscope

After all the connections have been made, adjust the vertical and horizontal scales so that they are reasonable as in the signals are neither too small nor do they go outside the screen. Hit the "acquire" button, and average the "number of samples". It is best to determine the number required based on the signal shown on the screen, but 64 is a good enough number to remove excessive noise in the signal.

Hit the "run/stop" button, and then the "single seq" button.

Testing

Hit the "trigger" button on the waveform generator as many times as samples needed. The oscilloscope will say 'Acq Complete' when we have hit it sufficient number of times.

To make an initial measurement
Hit the "cursor" button on the oscilloscope. (Under "Type" it should say "Time", if not then hit the button on the side until it does.)
Select cursor 1 by hitting the button to the right of it, and position the cursor using the dial. Then repeat the same for cursor 2. Make sure the color of the cursor matches the color of the channel. The difference in time between the cursors is shown on the screen.

To save the data
Open OpenChoice Desktop on the computer.
Select "Waveform Data Capture" from the tabs on the top.
Hit the "Select instrument" button on the left, if you are connected using the USB cable, then the first three letters of the instrument should be USB. Select it and hit OK.

Then click the “select channels” button to select the channels. You can either get the data from that point or click the “get data” button on the left.
Once the waveforms are on the screen, click the “save as” button, to save it to a .csv file. Add to the csv file information that you will need about the test, e.g. height and density of sample.

You can also save the oscilloscope settings in a file. Go to the “Get & Send” tab on the top, and then select the “get settings” button on the left. Then you click the “save as” button to save it.

The data can be processed using MATLAB. The m-file that does it is called plotter7a.m.